# MODELING ACID TRANSPORT AND NON-UNIFORM ETCHING IN A STOCHASTIC DOMAIN IN ACID FRACTURING

A Dissertation

by

JIANYE MOU

Submitted to the Office of Graduate Studies of
Texas A&M University
in partial fulfillment of the requirements for the degree of

DOCTOR OF PHILOSOPHY

August 2009

Major Subject: Petroleum Engineering

# MODELING ACID TRANSPORT AND NON-UNIFORM ETCHING IN A STOCHASTIC DOMAIN IN ACID FRACTURING

A Dissertation

by

JIANYE MOU

Submitted to the Office of Graduate Studies of
Texas A&M University
in partial fulfillment of the requirements for the degree of

DOCTOR OF PHILOSOPHY

Approved by:

| | |
|---|---|
| Chair of Committee, | A. Daniel Hill |
| Committee Members, | Ding Zhu |
| | Peter P. Valkó |
| | Juergen Hahn |
| Head of Department, | Stephen A. Holditch |

August 2009

Major Subject: Petroleum Engineering

# ABSTRACT

Modeling Acid Transport and Non-Uniform Etching in a Stochastic Domain

in Acid Fracturing. (August 2009)

Jianye Mou, B.S., Daqing Petroleum Institute, Daqing, China;

M.S., China University of Petroleum, Beijing, China

Chair of Advisory Committee: Dr. A. Daniel Hill

Success of acid fracturing depends on uneven etching along the fracture surfaces caused by heterogeneities such as variations in local mineralogy and variations in leakoff behavior. The heterogeneities tend to create channeling characteristics, which provide lasting conductivity after fracture closure, and occur on a scale that is neither used in laboratory measurements of acid fracture conductivity, which use core samples that are too small to observe such a feature, nor in typical acid fracture simulations in which the grid block size is much larger than the scale of local heterogeneities. Acid fracture conductivity depends on fracture surface etching patterns. Existing acid fracture conductivity correlations are for random asperity distributions and do not consider the contribution of channels to the conductivity. An acid fracture conductivity correlation needs the average fracture width at zero closure stress. Existing correlations calculate average fracture width using dissolved rock equivalent width without considering the effect of reservoir characteristics.

The purpose of this work is to develop an intermediate-scale acid fracture model with grid size small enough and the whole dimension big enough to capture local and macro heterogeneity effects and channeling characteristics in acid fracturing. The model predicts pressure field, flow field, acid concentration profiles, and fracture surface profiles as a function of acid contact time. By extensive numerical experiments with the model, we develop correlations of fracture conductivity and average fracture width at zero closure stress as a function of statistical parameters of permeability and mineralogy distributions.

With the model, we analyzed the relationships among fracture surface etching patterns, conductivities, and the distributions of permeability and mineralogy. From result analysis, we found that a fracture with channels extending from the inlet to the outlet of the fracture has a high conductivity because fluid flow in deep channels needs a very small pressure drop. Such long and highly conductive channels can be created by acids if the formation has heterogeneities in either permeability or mineralogy, or both, with high correlation length in the direction of the fracture, which is the case in laminated formations.

# DEDICATION

To my parents, my wife, Weibo Sui, and my son, Jerry Mou, for their love, support, and encouragement

# ACKNOWLEDGEMENTS

I would like to express my deepest appreciation to Dr. A. Daniel Hill and Dr. Ding Zhu for their invaluable academic guidance, motivation, encouragement, and support throughout this study. Also, I would like to extend my appreciation to Dr. Peter Valko and Dr. Juergen Hahn for serving as my committee members and for their invaluable comments and help. Special thanks also go to Dr. Hisham Nasr-El-Din for his advice.

I would like to thank my research group: Maysam Pournik, Jiayao Deng, Chunlei Zou, Gina Melendez, Camilo Malagon, and Luis Antelo. Thanks also go to my friends Xianlin Ma, Linfeng Bi, and Zhuoyi Li for their help with my research.

Finally, I would like to acknowledge financial support from the Acid Fracturing JIP at Texas A&M University and resources proved by the Harold Vance Department of Petroleum Engineering of Texas A&M University.

TABLE OF CONTENTS

Page

Page

Page

# LIST OF FIGURES

Page

Page

Page

Page

Page

Page

# LIST OF TABLES

Page

# CHAPTER I

# INTRODUCTION

## 1.1 Background

Carbonate reservoir acid stimulation consists of matrix acidizing, acidizing natural fractures, and acid fracturing. The first two are stimulation methods in which acid is injected at a pressure lower than the formation fracture pressure. The main purpose of matrix acidizing in carbonate is to bypass formation damage near a wellbore by generating wormholes. In case of naturally fractured carbonate reservoirs with or without damage, acidizing can be used to stimulate the reservoirs. It is different from matrix acidizing of un-fractured carbonate formations because the acid mainly flows through natural fractures.

As an effective stimulation technique alternative to propped fracturing in carbonate reservoirs all around the world, acid fracturing, initially applied to oilfields in the 1960s, is a stimulation method in which rock dissolution by acid along the surfaces of the hydraulically created fracture or reopened existing fractures is expected to create conductivity after fracture closure. Usually, acid is injected following a viscous pad fluid which is used to initiate a fracture. The common forms of acid include plain acid, gelled acid, foamed acid, or emulsified acid. In acid fracturing, the most commonly used acid is 15% HCl. Higher concentrations such as 20% or 28% HCl can also be used. HCl/organic

---

This dissertation follows the style and format of the *SPE Journal.*

acid blends or totally organic acid blends can be used in replacement of HCl in the situation of high temperature for reducing corrosion and reaction rate.

The primary objectives of designing acid fracturing treatments are to optimize live acid penetration distance and conductivity. The main parameters in a design include acid type and strength, acid injection volume, and injection rate of the acid. Acid fracture conductivity, a measure of the capacity for fluid flow through a fracture, is influenced by the amount of rock dissolved, the fracture surface etching patterns, the rock strength, and the closure stress. If a very small amount of rock is dissolved on the fracture surfaces, very little conductivity will be obtained because of very small fracture width. Uniform rock dissolution along the fracture gives little conductivity because the fracture will close under closure stress. By its nature, the success of acid fracturing depends on uneven acid etching along the fracture surface caused by heterogeneities such as variations in local mineralogy, variations in leakoff behavior, and variations in local stress that cause different fracture opening widths along the surfaces. Conductivity is created only if the less dissolved parts act like pillars to keep more dissolved parts open.

As a tool to design and optimize acid fracturing treatments, an acid fracturing simulator generally includes two parts: a fracture propagation module, which traces the fracture propagation and can be achieved by using existing hydraulic fracturing models although acid/rock reaction and leakoff behavior make it different from fracture propagation in hydraulic fracturing, and an acid transport module, which traces acid flow in the fracture. Acid fracture simulators calculate fracture conductivity using correlations, developed based on laboratory measurements of fracture conductivity on

samples which are a few inches in every direction. Acid fracture conductivity correlations describe how fracture conductivity changes with closure stress. They include two parts: fracture conductivity at zero closure stress and the rate of conductivity change with closure stress.

Currently there is no perfect acid fracturing model representing the complex physics of acid fracturing. Experience of acid fracturing treatments from similar reservoirs is a very important source to design new treatments. Acid fracturing treatment performance depends on many factors such as rock properties, closure stress, temperature, and spatial distributions of permeability and mineralogy. Many studies are done for live acid penetration distance. A few studies are done for acid fracture conductivity, and more is necessary to predict conductivity with better accuracy.

### 1.2 Problem Description

The success of acid fracturing depends on uneven acid etching along the fracture surfaces caused by heterogeneities, such as local mineralogy variation, leakoff variation because of permeability variations, and variations in stress that causes different fracture opening widths. Acid fracture conductivity is created only if less dissolved parts act like pillars to keep the fracture open under closure stress. Heterogeneities likely occur on the scale that neither is used in laboratory measurements of acid fracture conductivity, in which core samples are too small to observe such features, nor in typical acid fracture simulations, in which grid block size is much larger than the scale of heterogeneity due to computational limitations. Channeling characteristics caused by heterogeneities need to have widths on the order of inches for providing lasting conductivity after fracture

closure. Such features are sometimes seen in laboratory tests of acid fracture conductivity (Gong, 1997), but this is not common or easily repeatable because the breath of the fracture in lab tests is typically only an inch or two. Current acid fracturing models have a larger grid block size than can practically capture channels that are of the order of inches in breadth. A typical two-dimensional acid fracturing model can only predict uniform dissolution along contour lines fixed by the fracture geometry assumptions. For example, a model based on a PKN or KGD fracture predicts uniform rock dissolution, and hence, created conductivity. Although a three-dimensional model can predict non-uniform etching throughout the fracture domain, computational limitations result in dividing the fracture into grid blocks with dimension of several feet to tens of feet on a side. Current acid fracture models must extrapolate laboratory-based correlations of acid fracture conductivity measured on samples that are a few inches in each direction, to the macro-scale of fracture propagation model. This modeling approach does not incorporate the effect of local and macro-scale heterogeneities on conductivity.

Acid fracture conductivity both at zero closure stress and the rate of change with closure stress depends on fracture surface etching patterns, that is, the spatial distribution of fracture roughness. Random roughness distributions make void spaces isolated from each other, which gives low conductivity because of a large pressure drop for fluid flow in closed parts of the fracture. Spatially correlated distributions of roughness in the flow direction connect void space to form channels. A fracture with channels gives high conductivity because of negligible pressure drop in channels for fluid flow. Narrow

channels can keep open under high closure stress, so a fracture with narrow channels gives high conductivity at high closure stress. Fracture surface etching patterns depend on spatial characteristics of reservoirs properties such as permeability and mineralogy distributions. Existing correlations are for random roughness distributions and cannot consider the effects of channeling on conductivity.

When calculating conductivity using correlations, we need to know the conductivity at zero closure stress, which needs the average fracture width. Some correlations (Patir and Cheng, 1978; Walsh, 1981; Gong, 1997) did not give ways to calculate the average fracture width. And these correlations need parameters of a fracture such as standard deviation of fracture width or contact ratio, which are hard to obtain because there are no detailed fracture surface profiles. The Nierode Kruk correlation (1973) calculates conductivity at zero closure stress using an empirical correlation as a function of idea fracture width, which is the dissolved rock volume divided by the fracture area. The relationship between idea fracture width and fracture conductivity at zero closure stress depends on formation properties. For example, uniform acid etching gives zero conductivity after closure no matter what the dissolved rock volume is. The rougher the fracture surfaces, the larger the fracture conductivity is for the same dissolved rock volume. The Nierode Kruk correlation does not incorporate the effect of formation properties on fracture conductivity.

### 1.3 Objectives

The objective of the research is to develop an intermediate-scale acid fracture conductivity model, by which we can upscale the laboratory-based acid fracture

conductivity correlation to the field scale. The model has grid size small enough to capture local heterogeneities and total dimensions large enough to capture macro-scale heterogeneities. Macro-scale means the dimensions that can capture channel characteristics in acid fracturing, for example, the dimensions of a grid block in an acid fracture simulator. The model predicts the pressure field, the flow field, acid concentration profiles, and fracture surface profiles as functions of acid contact time. Acid fracture conductivity at zero closure stress is calculated based on fracture surface etching profiles output from the model by bring the two fracture surfaces into contact. With the model we study the relationship among the distributions of permeability and mineralogy, etching patterns, and conductivity, the channel contribution to conductivity, and the conditions to create deep, narrow channels. By extensive numerical experiments with the model, we develop correlations of fracture conductivity at zero closure stress as a function of statistical parameters of permeability and mineralogy distributions and average fracture width and correlations of average fracture width as a function of statistical parameters of permeability and mineralogy distributions and dissolved rock equivalent width. Both permeability and mineralogy distributions affect fracture surface etching patterns. According to their relative effects, we classify all the cases into three categories: permeability distribution dominance, mineralogy distribution dominance, and comparable effect of permeability and mineralogy distributions. We develop correlations for the three categories separately because it is not feasible to develop a unified correlation.

The complexity of the research lies in the moving, irregular fracture surfaces because of non-uniform acid etching along the fracture surfaces due to the heterogeneities such as local mineralogy variation and leakoff variation caused by permeability variation. It is not convenient to generate grid and imposing boundary conditions in numerical calculation for this kind of boundaries. We use a front-fixing method (Crank, 1984) to hand this complexity. By using body-fitted coordinate transformation, we can transform the physical moving, irregular boundaries into computational regular, fixed boundaries.

Fracture surface etching patterns depend on the spatial distributions of permeability and mineralogy. A common tool is semi-variogram model (Hardy and Beier, 1994) for spatially correlated distributions. We use GSLIB software incorporating a semi-variogram model to generate the permeability and mineralogy distributions. Tecplot is used for etching profile visualization.

The summary of the objectives of the research includes the following:

1) Generate mineralogy and permeability distributions on the fracture surfaces with geostatistical methods.
2) Calculate three-dimensional velocity and pressure fields in rough-walled fractures by solving the Navier-Stokes equations.
3) Trace acid transport in the fracture. Compute the three-dimensional acid concentration distribution by solving the acid balance equation with know velocity fields from (2).

4) Calculate acid/rock reaction with the known acid concentration on the fracture surfaces from (3). Update fracture surface profiles based on acid/rock reaction and get fracture surface etching profiles.
5) Calculate conductivity at zero closure stress based on the etching profile output from the model by bringing the two fracture surfaces into contact.
6) Study the relationship among etching pattern, conductivity, and the distributions of permeability and mineralogy. Based on extensive numerical study, develop correlations of fracture conductivity at zero closure stress as a function of average fracture width and statistical parameters of permeability and mineralogy distributions and correlations of average fracture width as a functions of dissolved rock equivalent width and statistical parameters of permeability and mineralogy distributions.

# CHAPTER II

# LITERATURE REVIEW

## 2.1 Acid Fracture Conductivity

Fracture conductivity indicates the capacity that a fluid flows through the fracture. After acid fracturing, as hydraulic pressure dissipates, the fracture surfaces deform and tend to close under closure stress, so the fracture conductivity decreases with closure stress increase. Acid fracture conductivity results from fracture roughness because the less dissolved parts can keep the fracture open. Because of rough fracture surfaces, it is difficult to calculate conductivity. Acid fracturing design models date back to the early 1970's. In early acid fracture designs (Williams and Nierode, 1972; Nierode et al., 1972; van Domselaar et al., 1973; Roberts and Guin, 1975; Coulter et al., 1974), fracture conductivity was assumed to be infinite to a distance from the wellbore to where the acid is 10% of its initial concentration. Of course, acid fracture conductivity is not infinite. Later on, many researchers developed acid fracture conductivity correlations to calculate finite fracture conductivity.

An acid fracture correlation has two parts: fracture conductivity at zero closure stress and the rate of conductivity change with closure stress. There are two possible ways to develop a correlation: theoretical and empirical. The Nierode Kruk correlation (1973) is an empirical one developed more than 3 decades ago based on a series of experiments, in which core plugs having one inch diameter and 2-3 inches in length were fractured in tension to a get rough-walled fracture.  It is the most commonly used one

because of its convenience and no need of parameters about fracture surface profiles. Walsh (1981) and Gong's (1997) correlations have theoretical bases. The inconvenience of using their models is that they require parameters related to fracture surface profiles, which cannot be obtained because of no detailed fracture surface etching profiles in acid fracturing. The fracture conductivity correlations can be plotted as a straight line in proper coordinate system with an intercept as a function of conductivity at zero closure stress and a slope representing the rate of fracture conductivity change with closure stress. These correlations are:

1) Nierode and Kruk correlation (1973)

$$k_f w = C_1 \exp(-C_2 \sigma_c) \quad \textbf{(2. 1)}$$

where

$$C_1 = (k_f w)_0 = 1.47 \times 10^7 w_i^{2.47} \quad \textbf{(2. 2)}$$

$$C_2 = (13.9 - 1.3 \ln S_{rock}) \times 10^{-3} \text{ for } S_{rock} < 20{,}000 \text{ psi} \quad \textbf{(2. 3)}$$

or

$$C_2 = (3.8 - 0.28 \ln S_{rock}) \times 10^{-3} \text{ for } S_{rock} > 20{,}000 \text{ psi} \quad \textbf{(2. 4)}$$

$w_i$ is the idea width calculated from dissolved rock volume, $\sigma_c$ is closure stress, and $S_{rock}$ is rock embedment stress.

2) Walsh correlation (1981)

$$(k_f w) = (k_f w)_0 \left[1 - (\sqrt{2} h / a_0) \ln(\sigma_c - p_0)_e\right]^3 \left[\frac{1 - b(\sigma_c - p_0)}{1 + b(\sigma_c - p_0)}\right] \quad \textbf{(2. 5)}$$

$$b = \sqrt{3}\pi (f / h) E (1 - \upsilon^2) \quad \textbf{(2. 6)}$$

where $p_0$ is reference pressure, $a_0$ is the half fracture width at some reference pressure, E is Young's modulus, $\upsilon$ is Poisson's ratio, $f$ is the auto-correlation distance, and $h$ is the root mean square (r.m.s.) value of the height distribution. The formula can be simplified except at very high pressures as

$$\left(k_f w\right) = \left(k_f w\right)_0 \left[1 - \left(\sqrt{2}h / a_0\right)\ln\left(\sigma_c - p_0\right)_e\right]^3 \quad \textbf{(2. 7)}$$

3) Gong correlation (1997)

$$k_f w = \left(k_f w\right)_0 \left[1 - \left(\frac{\gamma}{1+\gamma}\right)\left(\frac{2\sigma_c}{c\sigma_Y}\right)^{1/\gamma}\right]^6 \quad \textbf{(2. 8)}$$

where $\sigma_Y$ is rock yield stress, $c$ is contact ratio under closure stress, and $\gamma$ is a parameter charactering the shape of the distribution function curve. According to Gong, for a typical acid etched rough surface, the range of $\gamma$ is between 3 and 5.

### 2.2 Acid Fracturing Design Models

An acid fracturing model consists of a fracture propagation model and an acid transport model. Acid/rock reaction is incorporated in the acid transport model as boundary conditions, or some models directly set boundary acid concentration zero by assuming infinite acid/rock reaction rate. Acid fracture conductivity is calculated by using acid fracture conductivity correlations or assumed infinite conductivity from wellbore to where the acid concentration is above a certain value. Fracture propagation and acid transport are intrinsically coupled processes. For feasibility, they are decoupled to be implemented in separate models. The fracture propagation model directly makes use of existing hydraulic fracturing models although acid/rock reaction make it different

from hydraulic fracturing with non-reactive fluid. Velocity fields calculated from a fracture model are used in the acid transport model to get acid concentration distribution. Rock dissolution along the fracture surfaces is calculated from rock/acid reaction kinetics with the known acid concentration distribution. Because the fracture propagation model makes uses of existing hydraulic fracture models, the difference for different acid fracturing simulators lies in the acid transport model.

Early models (Williams and Nierode, 1972; Roberts and Guin, 1975) calculate a one-dimensional steady-state acid transport equation to get an analytical solution. The assumptions made in their models are (1) steady-state acid flow, (2) laminar and incompressible flow, (3) constant acid viscosity, (4) constant leakoff rate, and (5) neglected gravity force. The difference between their models is that Williams and Nierode's model assumes infinite reactions while Roberts and Guin's model assumes reaction rate to be controlled by both mass transfer and reaction rate.

Lo and Dean (1989) developed the first numerical model of acid fracturing. Their model assumes incompressible laminar steady-state flow, constant leakoff rate, and no gravity effect. An important aspect of the model is that the two-dimensional convection-diffusion equation is solved by a one-dimensional approximation with averaged acid concentration over the fracture width direction.

Settari (1993) developed a two-dimensional unsteady-state acid transport model. His model makes assumptions that (1) acid viscosity is not a function of acid concentration, (2) acid is incompressible, (3) reaction has no effects on velocity fields, (4) acid flow in the fracture height direction is neglected, and (5) diffusion in the fracture

length direction is negligible compared to convection. His model has the following characteristics: (1) acid spending is controlled by mass transfer and reaction rate, (2) multiple fluids with different rheologies are accounted for, (3) wormholes are considered to affect leakoff, and (4) thermal effects caused by heat of the reaction is considered. Acid transported to the fracture walls is calculated by using mass transfer coefficient and average acid concentration over the fracture width direction, which makes the acid transport equation solved one-dimensional.

When calculating acid transport to the fracture walls, we need to know the acid concentration distribution over the fracture width direction. Because of inability to calculate concentration gradient across the fracture width direction, the above models calculate acid transported to fracture walls by using mass transfer coefficient (first introduced by Roberts and Guin (1975)) relating acid transported to the fracture walls to average acid concentration over the fracture width direction.

To remove the use of mass transfer coefficient to calculate acid transport to the fracture walls, Romero et al. (1998) and Settari et al. (2001) developed acid transport models which consider the acid flow in the fracture width direction. Romero et al.'s model is an unsteady-state three-dimensional acid transport model with assumptions of negligible acid diffusion in the fracture length and height directions compared to corresponding convection terms. The model can be used for both Newtonian and power law fluids. When calculating acid transport, velocity fields are needed. The fracture model they used can only output two-dimensional velocity fields because it neglects the flow in the fracture width direction. They used Terill's solution (1965) to calculate three-

dimensional velocity fields based on the two-dimensional velocity fields and leakoff velocity. The model cannot consider non-uniform leakoff.

Settari et al. (1998) developed an unsteady-state two-dimensional acid transport model by considering the flow in the fracture length and width directions and neglecting variation in the fracture height direction. The model assumes that flow is incompressible, the reaction has no effect on volumetric flow rate, and concentration is uniform vertically. To get velocity in the fracture width direction, they made assumptions of self-similar, steady-state flow. By assuming that at every position in the fracture the flow profiles is fully developed, the velocities can be calculated from the average flow rate computed by the flow/geometry model and fluid properties. The model can be used for both Newtonian and non-Newtonian fluids. For accuracy and computational efficiency, their model uses non-uniform grid with small grid near fracture walls.

Dong (2001) developed a model to simulate acidizing in a natural fracture in carbonate reservoirs. Acidizing in natural fracture is similar to acid fracturing except that initial natural fracture width is much smaller than that created by hydraulic pressure in acid fracturing. His unsteady-state two-dimensional model considers rough fracture surfaces and two-dimensional fluid flow (the fracture length and height directions). Acid transported to the fracture walls is calculated by using a mass transfer coefficient. Flow fields are calculated based on local cubic law.

### 2.3 Velocity Fields in a Fracture

In a three-dimensional acid fracturing design model, the three-dimensional velocity field, which is necessary in acid concentration distribution calculation, is the

most difficult and time consuming part in acid fracturing modeling. Because of non-uniform acid leakoff on the fracture surfaces and rough fracture surfaces caused by non-uniform acid etching due to heterogeneous mineralogy and leakoff distributions, acid flow in a fracture is three-dimensional with flow across the fracture width direction cause by leakoff or irregular fracture shape. Existing acid fracture models use hydraulic fracture models to calculate velocity fields, which neglects the flow in the fracture width direction. For the three-dimensional acid transport model (Romero *et al.*, 1998), velocity fields are calculated based on 2D velocity fields output from the fracturing model and leakoff velocity by using formula derived from porous parallel plates with small, uniform leakoff distribution on the boundaries.

Before calculating velocity fields in a rough-walled fracture, we need to generate fracture shape. For a small specific fracture, fracture surface topography can be obtained by using a profilometer. Combining the two surfaces gives the fracture width distribution. Zimmerman et al. (2004) gave Navier-Stokes simulations in a 2 by 2 centimeters fracture. Fracture surface profiles are obtained by profilometer measurements. An experiment was done on the same fracture for comparison with numerical results. The finite element code FLUIDITY was used to solve the flow equations. They calculated two-dimensional flow without considering leakoff effect. The mesh was generated by using the fracture surface data. They confirmed the existence of weak inertial regime for small Reynolds numbers of 1-10. Above Reynolds numbers of 20, both simulations and experiments show non-Darcy pressure drop.

In situations of large fracture domain or artificial simulation, we need to generate a fracture numerically. Many researchers make use of geostatistical methods to generate fractures. Tsang and Tsang (1989), Pruess and Tsang (1990), and Murphy and Thomson (1993) use fracture width distribution $b(x, z)$ to characterize a rough-walled fracture with void space assumed to be perfectly planar, or in other words, fracture walls are mirror image about the x-z plane. Brown (1995) use an alternative method to generate a fracture with preserving undulation in the void space. His method requires the specification of only three main parameters: the fractal dimension, the RMS (root mean square) roughness at a reference length scale, and a length scale describing the degree of mismatch between the two fracture surfaces. Brush and Thomson (2003) generate a rough-walled fracture by combining random two-dimensional fields of the aperture and the mid-surface, both of which are generated by using spatially correlated standardized normal distribution.

Fractures have been traditionally idealized as parallel plates to get tractable mathematical formulation for fluid flow. The cubic law (Witherspoon et al., 1980) is derived for fluid flow in a fracture without leakoff on the walls. At the global scale, the fracture walls form a plane; while at local scale, fracture walls are rough surfaces with variable fracture width. For a fracture with rough surfaces, there are generally three ways to get velocity fields: solving Navier-Stokes (NS) equations, Stokes equations if inertial force is negligible, or Reynolds equation. In practice, because of extreme computational cost of solving NS or Stokes equations in a rough-walled fracture, it is a common practice to assume the three-dimensional flow may be approximated with two-

dimensional flow governed by Reynolds equation (Iwai, 1976; Tsang, 1984; Brown, 1987; Moreno et al., 1988). Reynolds equation, initially for hydrodynamic lubrication field, approximates Stokes equations with two-dimensional flow for the flow in a fracture with slightly nonparallel walls. The local cubic law (LCL) is a form of Reynolds equation for the fluid flow in fractures because local flow is proportional to the cube of local width. Using local cubic law, we can only get two-dimensional velocity fields, so to get three-dimensional velocity fields we need to solve Navier-Stokes equations or Stokes equation numerically in an irregular fracture shape.

Considering computational cost of solving NS equations, many researchers (Mourzenko et al., 1995; Brown et al., 1995; Brush and Thomson, 2003) compared the results from NS equations, Stokes equation, or Reynolds equation, the latter two of which cost less computation time. Brush and Thomson (2003) found that the difference of total flow rate from three-dimensional Stokes equation and LCL is within 10%, and the influence of inertial forces on bulk flow rate is small for very small Reynolds number (about 1 for fractures they used). Sarkar *et al.* (2004) simulated fluid flow in single fractures, fractures in parallel combination, fractures connected in series, and fracture networks by solving Stokes equation. They solved NS equations by using commercial implementation of Computational Fluid Dynamics (CFD) (Chung, 2002), FLUENT. They compared NS and Stokes simulation results and found that for low Reynolds number (about 100, depending on severity and frequency of aperture variation in the fracture), two methods gave comparable results.

Some researchers (Verberg and Ladd, 2002; Kim, 2002) use the Lattice Boltzmann method to solve flow fields in rough-walled fractures. Kim's model solves NS equations, and it takes a very long time even though he used parallel computation. Verberg and Ladd also reported numerical simulations of acid erosion in a fractured specimen of Carrara marble. Their results show that at large scales, erosion leads to increased heterogeneity via channel formation; whereas at small scales it tends to smooth out the roughness in the local aperture.

In acid fracturing, as the acid flows in the fracture, the acid is transported to the fracture surfaces to react with the rock. Non-uniform acid etching caused by heterogeneities generates rough and moving fracture walls, which makes it difficult to generate grids and impose boundary conditions in numerical calculation. The front fixing method (Crank, 1984) can handle this complexity by transforming a moving irregular physical domain into a regular fixed computational domain with coordinate transformation. Rhie (1985) and Acharya and Moukalled (1989) solved NS equations in curvilinear boundaries by using coordinate transformation, and their application is not for fluid flow in a fracture. Coakley et al. (1987) calculated fluid flow in rough-walled fractures to calculated equivalent permeability of fractures by using coordinate transformation to map a complex fracture shape into a simple one. For relatively simple fracture shape (four saw-tooth constrictions), they solve three-dimensional NS equations. Considering computational cost, they solved reduced NS equations (neglecting nonlinearity and zero velocity perpendicular to fracture walls) and Reynolds equation for complex fracture shape. It was found that Reynolds equation gives the largest equivalent

permeability, NS equations give the smallest equivalent permeability, and reduce NS equations gives an intermediate one.

### 2.4 Acid Transport to Fracture Surfaces and Acid Leakoff

Acid/rock reaction is a heterogeneous process involving acid transport to the rock surface, acid/rock reaction on the surfaces, and the products moving away from the surfaces. The overall reaction rate is controlled by the one with the slowest rate. Acid/rock reaction is classified into mass transfer limited, reaction rate limited, or both limited ones. In acid fracturing, acid/rock reaction and diffusion reduce acid concentration down the fracture. Reaction on the fracture walls consumes acid and leads to low acid concentration on the fracture surfaces, which generates acid concentration gradient across the fracture width direction so as to transport acid to the fracture surfaces by diffusion. Leakoff of acid into the formation also contributes part of acid transported to the fracture surfaces because part of leakoff acid etches the fracture walls before entering into the formation. Therefore, there are two mechanisms to transport acid to fracture walls: diffusion and convection by leakoff.

The acid concentration gradient and diffusion coefficient determine acid transport by diffusion. In laminar flow, acid diffusion coefficient equals the molecular diffusion but increases in the presence of turbulence. Williams and Nierode (1972) and Roberts and Guin (1975) used correlations developed from experiment measurements to calculate effective diffusion coefficients. Rozieres et al. (1994) conducted experiments to measure diffusion coefficients for straight acid, gelled acid, and emulsified acid for various temperatures.

In carbonate reservoir acidizing, wormholing occurs because acid preferentially flows along and reacts with relative large pores. In acid fracturing, wormholes caused by leakoff perpendicular to the fracture walls increase leakoff. Theoretical and experiment work was done to understand wormhole behavior (Hung, 1987; Daccord et al., 1989; Wang, 1993; Huang, 2000). It is difficult to predict wormhole effects analytically. Settari (1993) proposed a method to express leakoff increase in reacting fluid leakoff compared with an inert fluid. Acid leakoff is simulated with the general model (Settari 1985) in combination with increased ratio. First, generate leakoff velocity versus time from leakoff model used in the fracture simulator with realistic data for acid fluid but without acidizing effects. Secondly, in the laboratory, measure leakoff velocity for the acid. Compare leakoff velocity with and without acid effects to determine the increase ratio, which is a function of cumulative mass of acid loss to the formation per unit area or cumulative mass of acid contacting the walls per unit area. Third, with the increase ratio function established, calculate leakoff in acid fracturing.

Hill et al. (1995) proposed a leakoff model considering the effect of wormholing in acid fracturing. There are three mechanisms controlling the overall fluid leakoff: the compression of reservoir fluids, the thickness of the invaded zone, and filter cake formed on the fracture walls. Because of erosion of acid fluid, filter cake is not able to form in acid fracturing. Wormholes will primarily affect the invaded region. Because the wormhole dimension is much larger than the pore sizes in nonvugular formations, the pressure drop across the region penetrated by wormholes is negligible. The model predicts large leakoff increase in acid fracturing for gas reservoirs because of large

compressibility; while very small leakoff increase for oil reservoirs because of small compressibility.

# CHAPTER III

# INTERMEDIATE-SCALE ACID FRACTURING MODEL*

## 3.1 Introduction

The success of acid fracturing depends on heterogeneous acid etching along the fracture surfaces. Heterogeneity such as local mineralogy variation and leakoff variation because of permeability variations likely occurs on a scale that is neither used in the laboratory measurements of fracture conductivity which use samples too small to observe such features, nor in typical acid fracture simulators, in which the grid block size is much large than the scale of heterogeneity due to computational limitation. Small channels that are to remain open after fracture closure are sometimes seen in laboratory tests of acid fracture conductivity (Gong 1997), but this is not common or easily repeatable because the breadth of fracture in lab tests are typically a couple of inches. By modeling a fracture domain with dimensions up to ten feet in the height and length directions, the channels created can be predicted. In this study, we develop an intermediate-scale model with grid size small enough and total size big enough can capture the effects of local and macro-scale heterogeneities on fracture surface etching patterns and conductivity in acid fracturing. The reason that we call it intermediate-scale model is that the total dimensions of the model are comparable to a grid block size in an acid fracturing simulator and the grid sizes are comparable to core samples in

* Part of this chapter is reprinted with permission from "The Velocity Field and Pressure Drop Behavior in a Rough-Walled Fracture" by Mou, J., Hill, A.D., and Zhu, D., 2007. SPE © Paper SPE 105182 presented at the SPE Hydraulic Fracturing Technology Conference, College Station, TX.

experiments. In the model we focus on the fracture width variation because of rock dissolved by the acid instead of fracture propagation in the length and height directions, so we fix the length and height of the model as shown in Fig. 3.1. That is, the domain of the model is just a small portion of a whole fracture.

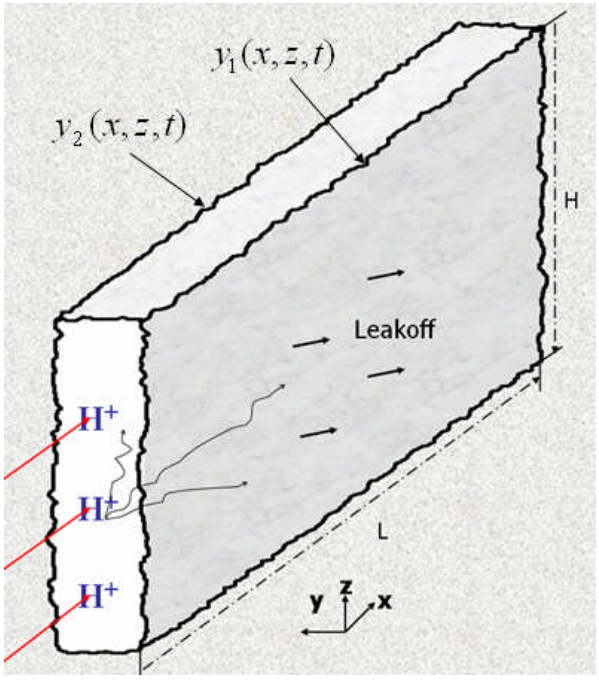


**Fig. 3.1 – The domain of the model.**

Like an acid fracturing simulator, the model simulates acid transport in the fracture, acid leakoff into the formation, acid/rock reaction on the fracture surfaces, and the fracture surface variation due to rock dissolution, but it does not track fracture propagation. From a mathematical view, we need to track fluid transport in the fracture to get velocity fields, track acid transport to get acid concentration distribution, calculate acid/rock reaction based on reaction kinetics, and update fracture surface profiles based

on acid/rock reaction. All these processes are coupled with each other. Practically, we can solve the governing equations sequentially if small time step is used in the numerical calculations. First, we calculate the Navier-Stokes equations with known boundary conditions to get velocity fields. Based on the velocity fields, we calculate acid concentration distribution, and then update fracture surface profiles according to rock/acid reaction. With updated boundary conditions, we repeat the procedure and we can get the fracture surface etching profiles with acid injection.

Acid/rock reaction generates heat so as to change the temperature distribution. Acid flow in the fracture changes temperature distribution because it has a different temperature from the formation temperature. These will affect acid/rock reaction in turn. We do not solve energy balance equation to calculate temperature distribution because of isothermal assumption. In acid fracturing, acid may be injected by multiple stages spaced with gel. In this research, only one-stage acid injection is considered.

### 3.2 Fluid Transport in a Fracture

Acid flow in a fracture is three-dimensional with flow in the width direction mainly caused by leakoff and irregular fracture shape. Three-dimensional velocity field calculation is the most time consuming part in the model. The fluid flow in the domain is transient because the fracture width changes with time due to acid/rock reaction and leakoff velocity changes with time. In numerical calculation, if time step is small, the fracture surfaces move very little in one time step, so it is reasonable that velocity and pressure fields are assumed to be steady state in one time step. In every time step, boundary conditions are updated to recalculate velocity and pressure fields. It is more

proper to call the process quasi-steady state. For feasibility, we make the following assumptions for fluid transport:

- Fluid is incompressible
- Newtonian fluid
- Acid/rock reaction does not affect volumetric flow rate
- Gravity is neglected
- Laminar flow
- Steady state

Reynolds number for flow through a fracture is defined as

$$\mathrm{Re} = \frac{\rho \bar{u} \bar{w}}{\mu} \quad \textbf{(3. 1)}$$

where $\bar{u}$ is the average velocity in the fracture length direction, and $\bar{w}$ is the average fracture width. According to Muralidhar and Long (1987), fluid flow in a fracture is laminar flow for Reynolds number less than 25. For a typical field acid fracturing job (Navarrete et al., 1998), Reynolds number is smaller than 25 for gelled acid, viscoelastic acid, and emulsified acid, but straight acid gives a Reynolds number much higher than 25, resulting to turbulence flow. In the simulations, we keep Reynolds number the same as typical field conditions. Therefore, the assumption of laminar flow is valid for gelled acid, viscoelastic acid, and emulsified acid, but not for straight acid.

Based on the assumptions, we use incompressible steady state Navier-Stokes equations (Chung, 2002) to calculate velocity fields. Navier-Stokes equations include momentum equations and continuity equation.

Momentum equations:

$$\rho(\vec{u}\cdot\nabla)\vec{u} = -\nabla p + \mu[\nabla^2\vec{u}] \quad \textbf{(3. 2)}$$

Continuity equation:

$$\nabla\cdot\vec{u} = 0 \quad \textbf{(3. 3)}$$

where $\vec{u} = (u, v, w)$

Boundary conditions are

- At the inlet, injection rate is given.

$$Q\big|_{x=0} = Q_{inj} \quad \textbf{(3. 4)}$$

- At the outlet, back pressure is given.

$$p\big|_{x=L} = p_{out} \quad \textbf{(3. 5)}$$

- On the fracture surfaces, velocity is known.

$$v\big|_{y=y_1,y_2} = v_L \quad \textbf{(3. 6)}$$

$$u\big|_{y=y_1,y_2} = 0 \quad \textbf{(3. 7)}$$

$$w\big|_{y=y_1,y_2} = 0 \quad \textbf{(3. 8)}$$

where $y_1$ and $y_2$ indicate the two fracture surfaces as shown in Fig. 3.1, and $v_L$ is leakoff velocity.

- At the bottom and top of the fracture, velocity is known.

$$u, v, w\big|_{z=0,H} = 0 \quad \textbf{(3. 9)}$$

### 3.3 Acid Transport in a Fracture

Tracking acid transport in the fracture is to get the acid concentration distribution with acid injection. Based on mass conservation and with the known velocity fields obtained from solving Navier-Stokes equations, we derive the acid balance equation. Acid is transported to the fracture surfaces by both diffusion and convection, so we consider diffusion and convection in the y direction. Diffusion in the x and z direction is neglected because convection dominates the acid flow in these directions.

Consider a control volume of $\Delta x \Delta y \Delta z$. During the time period of $\Delta t$, the amount of acid flowing into the control volume is

$$\Delta t C_i \left[ C_D u\big|_x \Delta y \Delta z + C_D w\big|_z \Delta x \Delta y + \left( C_D v - D_{eff} \frac{\partial C_D}{\partial y} \right)\Big|_y \Delta x \Delta z \right] \text{..... (3. 10)}$$

The amount of acid flowing out of the control volume is

$$\Delta t C_i \left[ C_D u\big|_{x+\Delta x} \Delta y \Delta z + C_D w\big|_{z+\Delta z} \Delta x \Delta y + \left( C_D v - D_{eff} \frac{\partial C_D}{\partial y} \right)\Big|_{y+\Delta y} \Delta x \Delta z \right] \text{..... (3. 11)}$$

where $C_D = C / C_i$. $C$ is acid concentration, $C_i$ is injected acid concentration. Their units are in $kg.mole/m^3$.

Accumulation of acid in the control volume during $\Delta t$ is

$$\Delta x \Delta y \Delta z C_i \left[ (C_D)^{n+1} - (C_D)^n \right] \text{..... (3. 12)}$$

Mass conservation means flow in – flow out = accumulation of acid, so we have

$$\Delta t C_i \left[ C_D u\big|_x \Delta y \Delta z + C_D w\big|_z \Delta x \Delta y + \left( C_D v - D_{eff} \frac{\partial C_D}{\partial y} \right)\Big|_y \Delta x \Delta z \right] -$$

$$\Delta t C_i \left[ C_D u\big|_{x+\Delta x} \Delta y \Delta z + C_D w\big|_{z+\Delta z} \Delta x \Delta y + \left( C_D v - D_{eff} \frac{\partial C_D}{\partial y} \right)\Big|_{y+\Delta y} \Delta x \Delta z \right] \text{..... (3. 13)}$$

$$= \Delta x \Delta y \Delta z C_i \left[ (C_D)^{n+1} - (C_D)^{n+1} \right]$$

Rearranging the above equation gives

$$\frac{C_D u\big|_x - C_D u\big|_{x+\Delta x}}{\Delta x} + \frac{C_D w\big|_z - C_D w\big|_{z+\Delta z}}{\Delta z} + \frac{C_D v\big|_y - C_D v\big|_{y+\Delta y}}{\Delta y} -$$

$$\frac{D_{eff} \frac{\partial C_D}{\partial y}\Big|_y - D_{eff} \frac{\partial C_D}{\partial y}\Big|_{y+\Delta y}}{\Delta y} = \frac{(C_D)^{n+1} - (C_D)^{n+1}}{\Delta t} \quad \text{..... (3. 14)}$$

Letting $\Delta t, \Delta x, \Delta y, \Delta z \to 0$ gives

$$\frac{\partial C_D}{\partial t} + u \frac{\partial C_D}{\partial x} + v \frac{\partial C_D}{\partial y} + w \frac{\partial C_D}{\partial z} = \frac{\partial}{\partial y} \left( D_{eff} \frac{\partial C_D}{\partial y} \right) \text{..... (3. 15)}$$

Boundary conditions are:

- At the inlet, acid concentration is constant.

  $$C_D(0, y, z, t) = 1 \text{..... (3. 16)}$$

- On the fracture walls, acid/rock reaction determines the acid concentration. This boundary condition cannot be specified explicitly. It is coupled with the acid balance equation. Following Romero et al. (1998), we have the boundary conditions:

  $$D_{eff} C_i \frac{\partial C_D}{\partial y} = E_f (C_i C_D - C_{eqm})^{n'} (1 - \phi)\Big|_{y_1} \text{..... (3. 17)}$$

$$-D_{eff}C_i\frac{\partial C_D}{\partial y}=E_f(C_iC_D-C_{eqm})^{n'}(1-\phi)\Big|_{y_2} \quad \text{..... (3. 18)}$$

where $C_{eqm}$ is the equilibrium concentration accounting for the effect of reverse reaction which is important for weak acids, $n'$ is the reaction order constant, $E_f$ is acid reaction rate constant, and $\phi$ is porosity.

- At the top and bottom of the fracture, we have closed boundaries.

$$\frac{\partial C_D}{\partial z}=0 \quad \text{..... (3. 19)}$$

Initial conditions are:

$$C_D(x,y,z,0)=0 \quad \text{..... (3. 20)}$$

### 3.4 Fracture Surface Variation

Acid/rock reaction occurring on the fracture surfaces causes the fracture surfaces to move with acid injection. The amount of rock dissolution depends on the amount of acid transported to the fracture surfaces. Fracture shape is irregular because of non-uniform etching on the fracture surfaces. Therefore, a fracture needs to be represented numerically. $y_1(x,z,t)$ and $y_2(x,z,t)$ denote positions of the two fracture surfaces. The fracture width is obtained by combining the two surfaces $b(x,z,t)=y_2(x,z,t)-y_1(x,z,t)$.

During time period of $\Delta t$, total acid transported to the area $\Delta x\Delta z$ on the fracture surface $y_1(x,z,t)$ is $\Delta tC_i\left(-fv_LC_D+D_{eff}\frac{\partial C_D}{\partial y}\right)\Big|_{x,y_1,z}$. $f$ is the percentage of leakoff acid

to react with the fracture surfaces before entering into the formation. This parameter empirically accounts for the fact that a portion of the acid leaking off into the formation does not contribute to the removal of rock from the fracture surfaces, but instead reacts inside the matrix. In this study, we have used a value of 0.3 determined from experiments. The volume of rock dissolved by the acid is $\Delta t\Delta x\Delta z\frac{\beta MW_{acid}C_i}{\rho(1-\phi)}\left(-fv_L C_D + D_{eff}\frac{\partial C_D}{\partial y}\right)\Big|_{x,y_1,z}$. The volume change caused by acid etching is $\Delta x\Delta z\left(y^{\,n}_{1x,z,t} - y^{\,n+1}_{1x,z,t}\right)$. $y_1(x,z,t)$ moves in the negative direction of the coordinate so that it is $y^{\,n}_{1x,z,t} - y^{\,n+1}_{1x,z,t}$. Equating the volume of the dissolved rock to the volume change gives

$$\Delta t\Delta x\Delta z\frac{\beta MW_{acid}C_i}{\rho(1-\phi)}\left(-fv_L C_D + D_{eff}\frac{\partial C_D}{\partial y}\right)\Big|_{x,y_1,z} = \Delta x\Delta z\left(y^{\,n}_{1x,z,t} - y^{\,n+1}_{1x,z,t}\right) \text{.....} \textbf{(3. 21)}$$

Rearranging the above equation gives

$$\frac{y^{\,n}_{1x,z,t} - y^{\,n+1}_{1x,z,t}}{\Delta t} = \frac{\beta MW_{acid}C_i}{\rho(1-\phi)}\left(-fv_L C_D + D_{eff}\frac{\partial C_D}{\partial y}\right)\Big|_{x,y_1,z} \text{.....} \textbf{(3. 22)}$$

Letting $\Delta t \to 0$ gives

$$\frac{\partial y_1(x,z,t)}{\partial t} = \frac{\beta MW_{acid}C_i}{\rho(1-\phi)}\left(fv_L C_D - D_{eff}\frac{\partial C_D}{\partial y}\right)\Big|_{x,y_1,z} \text{.....} \textbf{(3. 23)}$$

Following the same procedure, we can get the equation for another surface

$$\frac{\partial y_2(x,z,t)}{\partial t} = \frac{\beta MW_{acid}C_i}{\rho(1-\phi)}\left(fv_L C_D - D_{eff}\frac{\partial C_D}{\partial y}\right)\Big|_{x,y_2,z} \text{.....} \textbf{(3. 24)}$$

The fracture shape before acid injection is the initial conditions for the fracture surface position variation. The positions of fracture surfaces are updated explicitly based on acid/rock reaction after getting the acid concentration distribution in every time step.

### 3.5 Leakoff Model

Leakoff affects the model via changing velocity fields with time as boundary conditions in solving the Navier-Stokes equations. Wormholes caused by rock dissolution in matrix by leakoff acid increase acid leakoff in turn. It is necessary to include the effects of wormholes on leakoff. Hill et al. (1995) presented a leakoff coefficient formula taking into account the effect of wormholing on fluid in acid fracturing as

$$C_{wh} = \frac{-\frac{1}{C_c} + \sqrt{\frac{1}{C_c^2} + \frac{4}{C_{v,wh}^2}}}{2\left(\frac{1}{C_{v,wh}^2}\right)} \quad \text{..... (3. 25)}$$

where

$$C_c = \sqrt{\frac{\phi c_t k}{\pi \mu}}\left(p_f - p_R\right) \quad \text{..... (3. 26)}$$

$$C_{v,mh} = \sqrt{\frac{\phi k}{2\mu\left(1-\frac{1}{Q_{ibt}}\right)}}\left(p_f - p_R\right)^{\frac{1}{2}} \quad \text{..... (3. 27)}$$

$C_c$ is the compressibility fluid-loss coefficient, $C_{v,mh}$ is the viscous fluid-loss coefficient with wormholing, $p_f$ is the pressure in the fracture; and $p_R$ is the pressure in

the reservoir. $Q_{ibt}$ is the number of pore volume required for a wormhole to breakthrough in a coreflood. Dolomite, compared with limestone, has larger $Q_{ibt}$, which means slow wormhole growth rate. In acid fracturing, it is difficult to form filter cake, so its effect is neglected. With the definition of leakoff coefficient, leakoff rate is still defined as $v_L = C_{wh} / \sqrt{t}$.

### 3.6 Characterizing a Fracture

A fracture should be characterized numerically because of the irregular shape and the non-uniform permeability and mineralogy distributions. Generating a fracture includes the positions of the two fracture surface, permeability distribution, which determines leakoff distribution, and mineralogy distribution, which determines acid/rock reaction rate distribution. Combining the two fracture surfaces gives the fracture width distribution.

Permeability and mineralogy distributions show characteristics of directionality, that is, they are spatially correlated instead of completely random. For example, they are more correlated in the bedding direction and less correlated in the direction perpendicular to the bedding. It is common to observe permeability streaks in layered reservoirs. Mineralogy distribution shows layering in the bedding direction. A semi-varigrom model (Hardy and Beier, 1994), which is an important tool in geostatistics describing spatially correlated distributions, is used to describe permeability and mineralogy distributions. We use the geostatistical software GSLIB (Deutsch and Journel, 1998), which incorporates a semi-variogram model for spatial correlation, to

generate spatially correlated numbers, with which we generate permeability distribution, mineralogy distribution, and initial fracture shape. In GSLIB, we need to input correlation length. How the correlation length affects distribution will be demonstrated in the permeability distribution part.

### 3.6.1 Initial Fracture Shape

Initial fracture surfaces could be rough or flat. For a rough-walled fracture, we use GSLIB to generate random numbers, with which we generate the fracture shape. Fig. 3.2 shows an example of a rough-walled fracture. Considering the characteristics of a fracture that the fracture height and length are much larger than the fracture width, we can also use regular fracture shape as initial fracture shape, which just requires the fracture width as input.

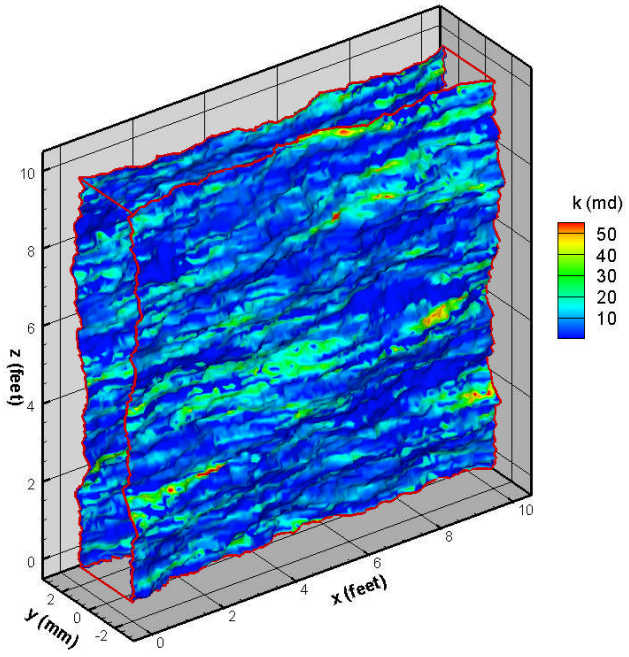


**Fig. 3.2 – An example of a rough-walled fracture.**

### 3.6.2 Permeability Distribution

Permeability distribution is lognormal, so we use the following formula to generate permeability distribution:

$$k(I,K) = e^{Mean\ln k + Stdev\ln k * N(I,K)} \quad \text{..... (3. 28)}$$

where $Mean\ln k$ is the mean of the natural log of the permeability distribution, $Stdev\ln k$ is the standard deviation of the natural log of the permeability distribution, and $N(I,K)$ is the spatially correlated number output from GSLIB.

GLIB needs input of the correlation length, which is the distance from a point beyond which there is no further correlation of a physical property associated with that point. How the correlation length affects the distribution is demonstrated by the comparison of Fig. 3.3 and Fig. 3.4. In Fig. 3.3, the horizontal correlation length is 0.06L, and the vertical correlation length is 0.03H, which means low correlation length in both directions. The permeability distribution is an almost random distribution. In Fig. 3.4, the horizontal correlation length is 0.5L, and the vertical correlation length is 0.03H, which means high correlation length in the horizontal direction and low correlation length in the vertical direction. The permeability distribution is more correlated in the horizontal direction. We can see the layering characteristics of the permeability distribution. The higher the correlation length, the more correlated the permeability distribution in that direction, and vice versa.

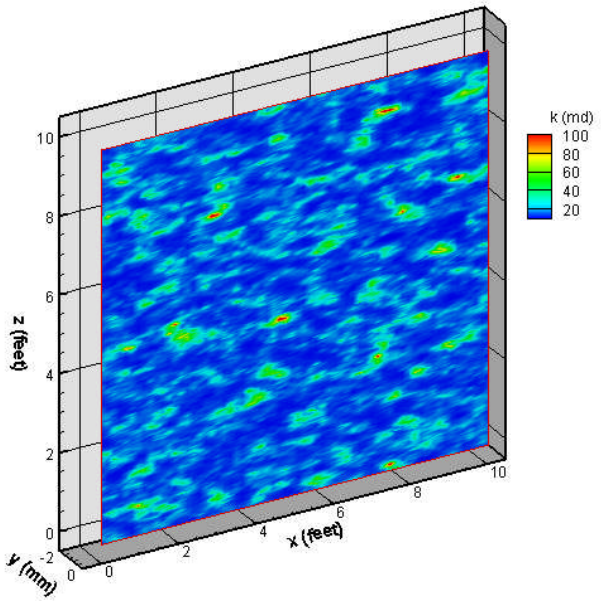


**Fig. 3.3 – Permeability distribution on one fracture surface (the horizontal correlation length is 0.06L, and the vertical correlation length is 0.03H).**

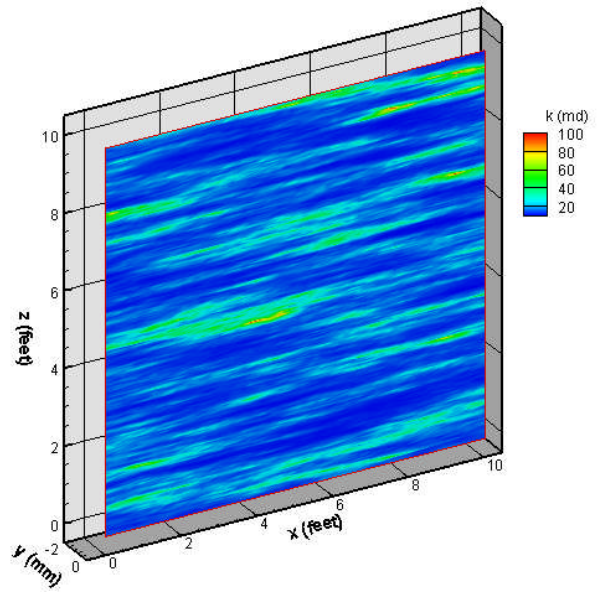


**Fig. 3.4 – Permeability distribution on one fracture surface (the horizontal correlation length is 0.5L, and the vertical correlation length is 0.03H).**

### 3.6.3 Mineralogy Distribution

In carbonate reservoirs, the spatial distribution of petrophysical properties is controlled by geologic processes of deposition and diagenesis. Diagenesis, including (1) calcite carbonate cementation, (2) mechanical and chemical compaction, (3) selective dissolution, (4) dolomitization, (5) evaporate mineralization, and (6) massive dissolution, cavern collapse, and fracturing, typically reduces porosity (Lucia 1999). Dolomitization is caused by presence of the mineral dolomite and requires fluid flow for introduction of Magnesium into the system. Therefore fluid flow is essential for the origin of dolomite fabrics, and dolomite patterns may not be linked to depositional pattern. Evaporite results from the presence of evaporite of minerals such as anhydrite and gypsum. Anhydrite and gypsum are commonly associated with dolomitization and require transporting sulfate into the system by hyper-saline water.

From the perspective of chemical composition, carbonate reservoirs are comprised of limestone, dolomite, and HCl insoluble materials (anhydrite, quarts, and shale). In this research, we just consider limestone and dolomite.

According to Blatt et al. (1980), most carbonate sediments show laminations. Carbonate rocks can change abruptly from dolomite to limestone. When generating mineralogy distributions, we always use a high horizontal correlation length. With the spatially correlated number output from GSLIB, we need the percentage of limestone and dolomite to generate mineralogy distributions. Fig. 3.5 shows an example of mineralogy distribution with 70% limestone and 30% dolomite.

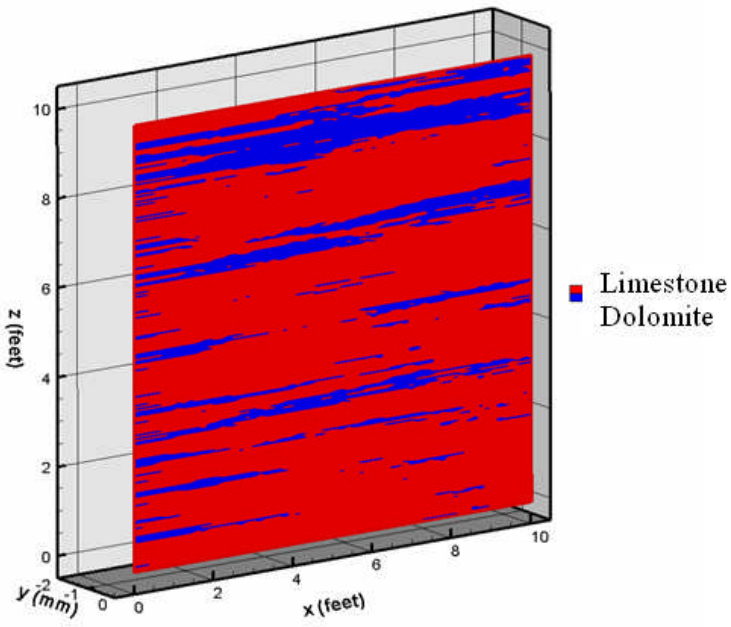


**Fig. 3.5 – An example of mineralogy distribution.**

# CHAPTER IV

# NUMERICAL SOLUTION OF THE MODEL*

## 4.1 Methodology

### 4.1.1 Front-Fixing Method

A fracture domain is irregular, and fracture walls move with time because of non-uniform acid etching along the fracture surfaces so that it is not convenient to generate grids and imposing boundary conditions in numerical calculations. We use the front-fixing method (Crank, 1984) to handle this complexity. By using a body-fitted coordinate transformation, we can transform an irregular, moving physical domain into regular, fixed computational domain by choosing proper coordinates. Fig. 4.1 shows an example of the physical and computational domains in three dimensions.

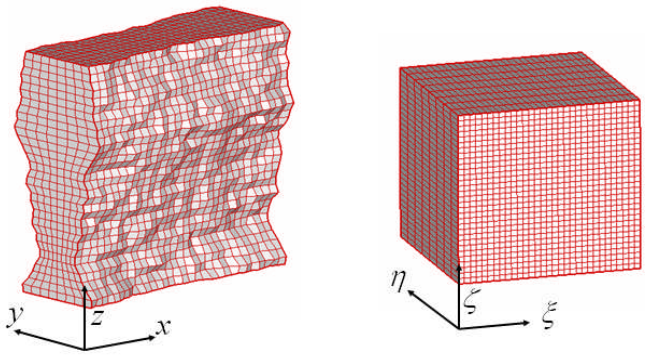


**Fig. 4.1 – An example of physical and computational domains in three dimensions.**

* Part of this chapter is reprinted with permission from "The Velocity Field and Pressure Drop Behavior in a Rough-Walled Fracture" by Mou, J., Hill, A.D., and Zhu, D., 2007. SPE © Paper SPE 105182 presented at the SPE Hydraulic Fracturing Technology Conference, College Station, TX.

The definition of new coordinates depends on the shape of boundaries. We will discuss the definition of new coordinates for a fracture domain later.

### 4.1.2 Solution Procedures

We solve the governing equations sequentially because some variables in one equation are output from the solution of other equations. First of all, we generate initial fracture shape and the distributions of permeability and mineralogy. Next, by choosing proper coordinates, we transform irregular fracture shape into regular computational domain for convenience of grid generation and imposing boundary conditions. Then, we solve the Navier-Stokes equations to get velocity fields, with which we solve the acid balance equation to get the acid concentration distribution. Based on the acid/rock reaction, we update fracture surface profiles, which are used as new boundary conditions to repeat the above processes. Fracture surface etching profiles are output for certain acid contact times. Conductivity at zero closure stress is calculated bases on fracture surface profiles. With the model, we do extensive numerical studies to develop fracture conductivity and average fracture width correlations at zero closure stress. The detailed procedure is as follows.

1. Generate initial fracture shape and the distributions of permeability and mineralogy with GSLIB.
2. Do coordinate transformation and generate grids with proper coordinate definition and known boundary conditions.

3. Solve the Navier-Stokes equations to get velocity and pressure fields. In every time step, with known fracture shape and boundary conditions, incompressible steady-state Navier-Stokes equations are solved to get velocity and pressure fields by iteration.
4. Solve the acid balance equation to get acid concentration distribution. With known velocity fields, we solve the acid balance equation to get acid concentration distribution in time sequence.
5. Update fracture surface profiles. With the acid concentration distribution, we compute acid/rock reaction to update fracture surface profiles.
6. With the updated fracture surface profiles and boundary conditions, repeat steps 2~5 for the whole simulation time. Output fracture surface profiles for certain acid contact times.
7. Calculate fracture conductivity at zero closure stress based on fracture profiles by bringing the two fracture surfaces into contact.

In the simulation, in every time step, we calculate incompressible steady-state Navier-Stokes equations with given boundary conditions. An implicit assumption is that boundaries change very little in one time step. Therefore, the time step should be very small. Most of computation time is spent in solving the Navier-Stokes equations because iteration is necessary to get solutions for every time step. Fig. 4.2 shows the flow chart of the model.

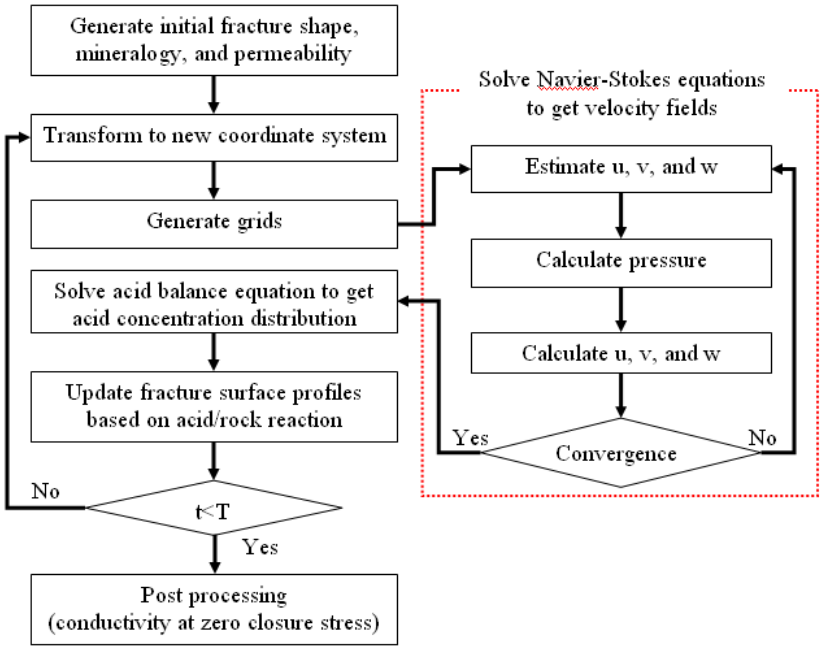


**Fig. 4.2 – Flow chart of the model.**

## 4.2 New Coordinates Definition

Before numerical simulation, new coordinates are defined to transform the irregular physical domain into a regular computational one. In acid fracturing, the focus is on fracture wall movement due to rock dissolution by acid instead of fracture propagation in the length and height directions. The characteristics of a fracture are $L, H >> width$, so the new coordinates are defined as

$$\xi = \frac{x}{L} \qquad 0 \le \xi \le 1 \quad \textbf{(4. 1)}$$

$$\eta = \frac{y - y_1(x,z,t)}{b(x,z,t)} \qquad 0 \le \eta \le 1 \quad \textbf{(4. 2)}$$

$$\zeta = \frac{z}{H} \qquad 0 \le \zeta \le 1 \quad \textbf{(4. 3)}$$

where

$$b(x,z,t) = y_2(x,z,t) - y_1(x,z,t) \quad \textbf{(4. 4)}$$

$y_2(x,z,t)$ and $y_1(x,z,t)$ denote the fracture surfaces as shown in Fig. 3.1.

### 4.3 Coordinate Transformation

With the definition of coordinate system above, we use chain rule to do coordinate transformation. The relationship between physical coordinates and computational one is as follows.

$$x_\xi = L \quad \textbf{(4. 5)}$$

$$x_\eta = 0 \quad \textbf{(4. 6)}$$

$$x_\zeta = 0 \quad \textbf{(4. 7)}$$

$$y_\xi = \eta \frac{\partial b(x,z,t)}{\partial \xi} + \frac{\partial y_1(x,z,t)}{\partial \xi} \quad \textbf{(4. 8)}$$

$$y_\eta = b(x,z,t) \quad \textbf{(4. 9)}$$

$$y_\zeta = \eta \frac{\partial b(x,z,t)}{\partial \zeta} + \frac{\partial y_1(x,z,t)}{\partial \zeta} \quad \textbf{(4. 10)}$$

$$z_\xi = 0 \quad \textbf{(4. 11)}$$

$$z_\eta = 0 \quad \textbf{(4. 12)}$$

$$z_\zeta = H \quad \textbf{(4. 13)}$$

Jacobian is

$$J = \begin{vmatrix} x_\xi & x_\eta & x_\zeta \\ y_\xi & y_\eta & y_\zeta \\ z_\xi & z_\eta & z_\zeta \end{vmatrix} = LHb(x,z,t) \quad \text{..... (4. 14)}$$

### 4.3.1 Navier-Stokes Equations

We use the SIMPEM (Acharya and Moukalled, 1989) method to solve the Navier-Stokes equations. With the definition of new coordinates, the Navier-Stokes equations are transformed into the new coordinate system. In the new system, we define contravariant velocity components as

$$U = J\left(u\xi_x + v\xi_y + w\xi_z\right) \quad \text{..... (4. 15)}$$

$$V = J\left(u\eta_x + v\eta_y + w\eta_z\right) \quad \text{..... (4. 16)}$$

$$W = J\left(u\zeta_x + v\zeta_y + w\zeta_z\right) \quad \text{..... (4. 17)}$$

After coordinate transformation, governing equations and boundary conditions in new coordinates are as follows.

- Continuity equation

$$\frac{\partial U}{\partial \xi} + \frac{\partial V}{\partial \eta} + \frac{\partial W}{\partial \zeta} = 0 \quad \text{..... (4. 18)}$$

- Momentum equations

$$\begin{aligned} &\frac{\partial}{\partial \xi}\left[\rho U u - \mu J\left(\alpha \frac{\partial u}{\partial \xi} + \lambda_1 \frac{\partial u}{\partial \eta} + \lambda_2 \frac{\partial u}{\partial \zeta}\right)\right] + \\ &\frac{\partial}{\partial \eta}\left[\rho V u - \mu J\left(\lambda_1 \frac{\partial u}{\partial \xi} + \beta \frac{\partial u}{\partial \eta} + \lambda_3 \frac{\partial u}{\partial \zeta}\right)\right] + \\ &\frac{\partial}{\partial \zeta}\left[\rho W u - \mu J\left(\lambda_2 \frac{\partial u}{\partial \xi} + \lambda_3 \frac{\partial u}{\partial \eta} + \gamma \frac{\partial u}{\partial \zeta}\right)\right] = s_1 \end{aligned} \quad \text{..... (4. 19)}$$

$$\frac{\partial}{\partial\xi}\left[\rho Uv-\mu J\left(\alpha\frac{\partial v}{\partial\xi}+\lambda_1\frac{\partial v}{\partial\eta}+\lambda_2\frac{\partial v}{\partial\zeta}\right)\right]+$$
$$\frac{\partial}{\partial\eta}\left[\rho Vv-\mu J\left(\lambda_1\frac{\partial v}{\partial\xi}+\beta\frac{\partial v}{\partial\eta}+\lambda_3\frac{\partial v}{\partial\zeta}\right)\right]+ \quad \text{..... (4. 20)}$$
$$\frac{\partial}{\partial\zeta}\left[\rho Wv-\mu J\left(\lambda_2\frac{\partial v}{\partial\xi}+\lambda_3\frac{\partial v}{\partial\eta}+\gamma\frac{\partial v}{\partial\zeta}\right)\right]=s_2$$

$$\frac{\partial}{\partial\xi}\left[\rho Uw-\mu J\left(\alpha\frac{\partial w}{\partial\xi}+\lambda_1\frac{\partial w}{\partial\eta}+\lambda_2\frac{\partial w}{\partial\zeta}\right)\right]+$$
$$\frac{\partial}{\partial\eta}\left[\rho Vw-\mu J\left(\lambda_1\frac{\partial w}{\partial\xi}+\beta\frac{\partial w}{\partial\eta}+\lambda_3\frac{\partial w}{\partial\zeta}\right)\right]+ \quad \text{..... (4. 21)}$$
$$\frac{\partial}{\partial\zeta}\left[\rho Ww-\mu J\left(\lambda_2\frac{\partial w}{\partial\xi}+\lambda_3\frac{\partial w}{\partial\eta}+\gamma\frac{\partial w}{\partial\zeta}\right)\right]=s_3$$

where

$$\alpha=(\xi_x)^2+(\xi_y)^2+(\xi_z)^2 \quad \text{..... (4. 22)}$$

$$\beta=(\eta_x)^2+(\eta_y)^2+(\eta_z)^2 \quad \text{..... (4. 23)}$$

$$\gamma=(\zeta_x)^2+(\zeta_y)^2+(\zeta_z)^2 \quad \text{..... (4. 24)}$$

$$\lambda_1=\xi_x\eta_x+\xi_y\eta_y+\xi_z\eta_z \quad \text{..... (4. 25)}$$

$$\lambda_2=\xi_x\zeta_x+\xi_y\zeta_y+\xi_z\zeta_z \quad \text{..... (4. 26)}$$

$$\lambda_3=\eta_x\zeta_x+\eta_y\zeta_y+\eta_z\zeta_z \quad \text{..... (4. 27)}$$

$$s_1=-J\left(\frac{\partial\xi}{\partial x}\frac{\partial p}{\partial\xi}+\frac{\partial\eta}{\partial x}\frac{\partial p}{\partial\eta}+\frac{\partial\zeta}{\partial x}\frac{\partial p}{\partial\zeta}\right) \quad \text{..... (4. 28)}$$

$$s_2=-J\left(\frac{\partial\xi}{\partial y}\frac{\partial p}{\partial\xi}+\frac{\partial\eta}{\partial y}\frac{\partial p}{\partial\eta}+\frac{\partial\zeta}{\partial y}\frac{\partial p}{\partial\zeta}\right) \quad \text{..... (4. 29)}$$

$$s_3 = -J\left(\frac{\partial \xi}{\partial z}\frac{\partial p}{\partial \xi} + \frac{\partial \eta}{\partial z}\frac{\partial p}{\partial \eta} + \frac{\partial \zeta}{\partial z}\frac{\partial p}{\partial \zeta}\right) \quad \textbf{(4. 30)}$$

Boundary conditions:

- On the fracture surfaces

$$V\big|_{\xi,\eta=0,1,\zeta} = LHv_L \quad \textbf{(4. 31)}$$

$$U,W\big|_{\xi,\eta=0,1,\zeta} = 0 \quad \textbf{(4. 32)}$$

- On the top and bottom

$$U,V,W\big|_{\xi,\eta,\zeta=0,1} = 0 \quad \textbf{(4. 33)}$$

- At the inlet and outlet

$$Q_{inj} = \int_A u\big|_{\xi=0}\, dA \quad \textbf{(4. 34)}$$

$$p\big|_{\xi=1} = p_0 \quad \textbf{(4. 35)}$$

### 4.3.2 Acid Balance Equation

In the new coordinate system, the acid balance equation becomes

$$\frac{\partial C_D}{\partial t} - \left(\frac{1}{b}\frac{\partial y_1}{\partial t} + \frac{\eta}{b}\frac{\partial b}{\partial t}\right)\frac{\partial C_D}{\partial \eta} + \frac{U}{J}\frac{\partial C_D}{\partial \xi} + \frac{V}{J}\frac{\partial C_D}{\partial \eta} + \frac{W}{J}\frac{\partial C_D}{\partial \zeta} - D_{eff}\frac{1}{b^2}\frac{\partial^2 C_D}{\partial \eta^2} = 0 \quad \textbf{(4. 36)}$$

with boundary conditions:

- At the inlet

$$C_D(0,\eta,\zeta,t) = 1 \quad \textbf{(4. 37)}$$

- On the fracture surfaces

$$-\frac{D_{eff}C_i}{b}\frac{\partial C_D}{\partial \eta} = E_f (C_i C_D - C_{eqm})^{n'}(1-\phi)\Big|_{\eta=0} \quad \text{..... (4. 38)}$$

$$\frac{D_{eff}C_i}{b}\frac{\partial C_D}{\partial \eta} = E_f (C_i C_D - C_{eqm})^{n'}(1-\phi)\Big|_{\eta=1} \quad \text{..... (4. 39)}$$

- On the top and bottom

$$\left[\left(-\frac{\eta}{Hb}\frac{\partial b}{\partial \zeta} - \frac{1}{Hb}\frac{\partial y_1}{\partial \zeta}\right)\frac{\partial C_D}{\partial \eta} + \frac{1}{H}\frac{\partial C_D}{\partial \zeta}\right]\Big|_{\zeta=0,1} = 0 \quad \text{..... (4. 40)}$$

Initial condition:

$$C_D(\xi,\eta,\zeta,0) = 0 \quad \text{..... (4. 41)}$$

### 4.3.3 Update Fracture Surface Positions

$$\frac{\partial y_1(x,z,t)}{\partial t} = \frac{\beta MW_{acid}C_i}{\rho(1-\phi)}\left(fv_L C_D - \frac{D_{eff}}{b}\frac{\partial C_D}{\partial \eta}\right)\Big|_{\eta=0} \quad \text{..... (4. 42)}$$

$$\frac{\partial y_2(x,z,t)}{\partial t} = \frac{\beta MW_{acid}C_i}{\rho(1-\phi)}\left(fv_L C_D - \frac{D_{eff}}{b}\frac{\partial C_D}{\partial \eta}\right)\Big|_{\eta=1} \quad \text{..... (4. 43)}$$

## 4.4 Finite Difference Equations

Partial differential equations are discretized with the control volume method. The finite difference equations are in Appendix A.

## 4.5 Model Validation

The model is validated by comparing velocity fields of numerical solution with analytical solutions for regular fracture shapes, in which analytical solution is possible,

by checking acid material balance, and by comparing simulation results with experiments.

### 4.5.1 Velocity Fields and Pressure Drop Behavior

The first results to be validated are velocity fields. Fig. 4.3 shows a comparison for slot flow without leakoff. The velocity is of parabolic shape across the fracture width according to the following formula.

$$u(y) = \frac{wy - y^2}{2\mu} \frac{\Delta p}{L} \quad \text{..... (4. 44)}$$

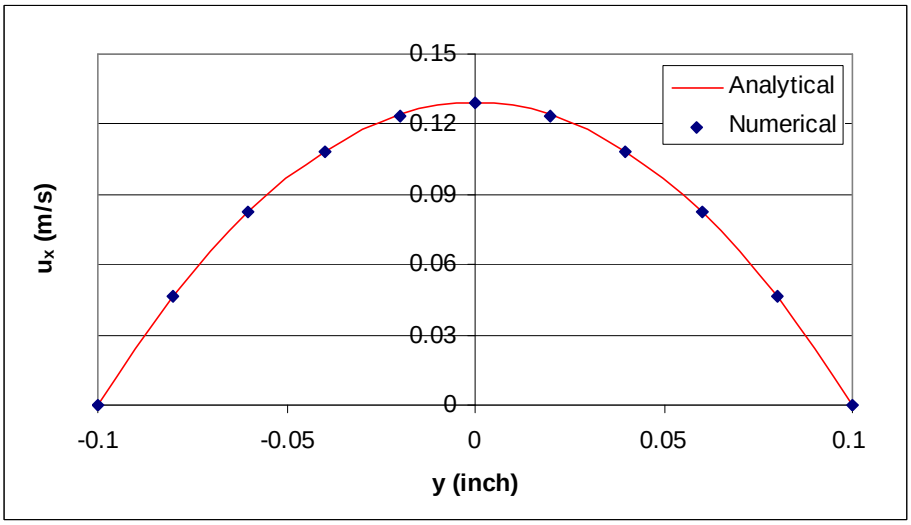


**Fig. 4.3 – The comparison of velocity in the x direction across the fracture width direction in slot flow without leakoff.**

Terrill (1964) gave analytical solution for slot flow with uniform leakoff on walls. Fig. 4.4 and Fig. 4.5 show the comparison of numerical and analytical results.

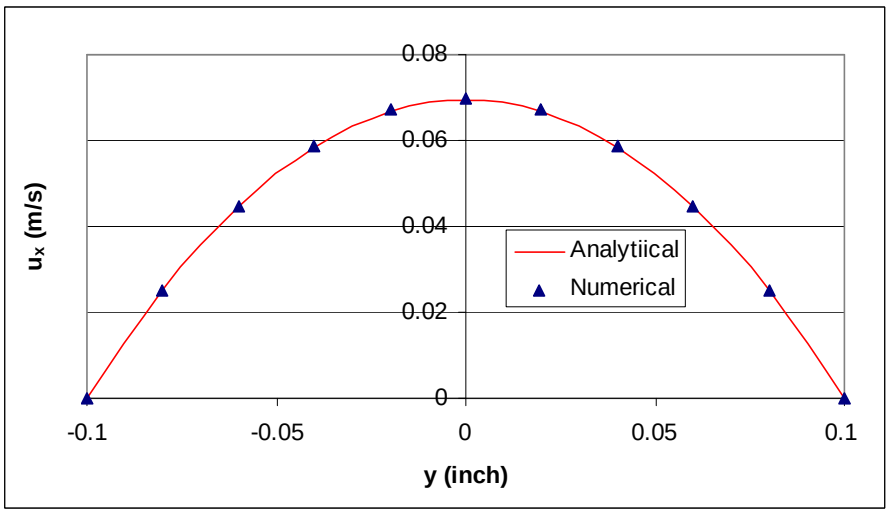


**Fig. 4.4 – The comparison of velocity in the x direction across the fracture width direction in slot flow with uniform leakoff.**

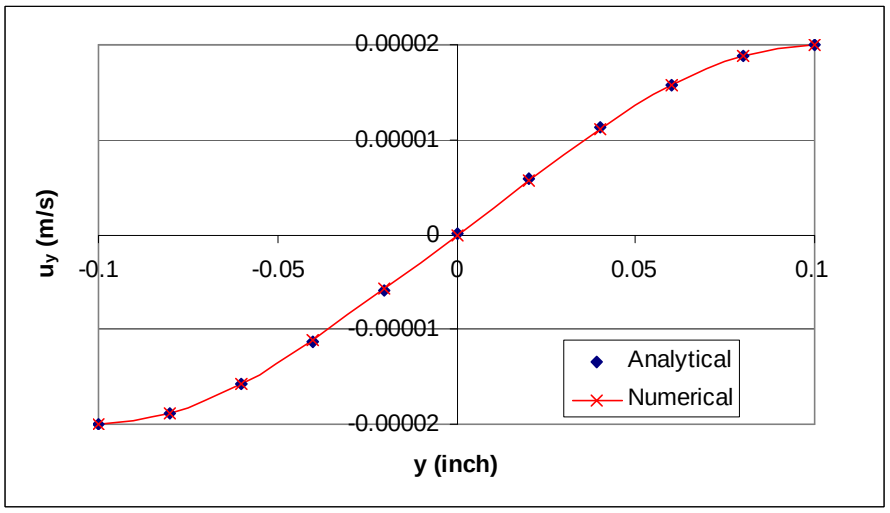


**Fig. 4.5 – The comparison of velocity in the y direction across the fracture width direction in slot flow with uniform leakoff.**

Fig. 4.6 shows how fracture shape affects velocity fields with uniform leakoff on the surfaces. Corresponding contour of velocity in the x direction is in Fig. 4.7. Down the fracture, velocity is very low because of leakoff.

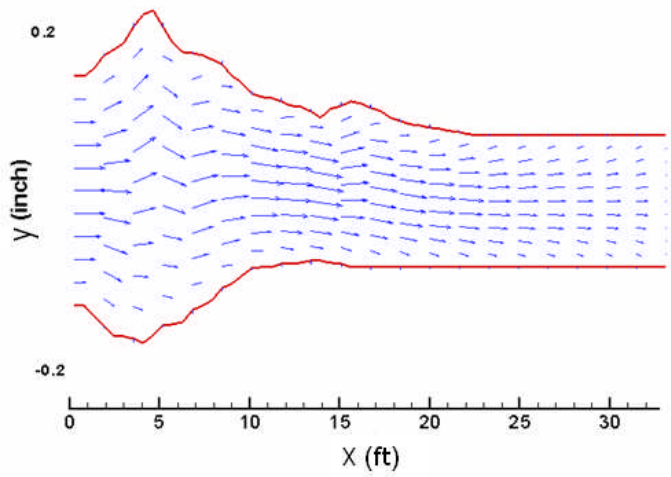


**Fig. 4.6 – Velocity fields for irregular fracture shape.**

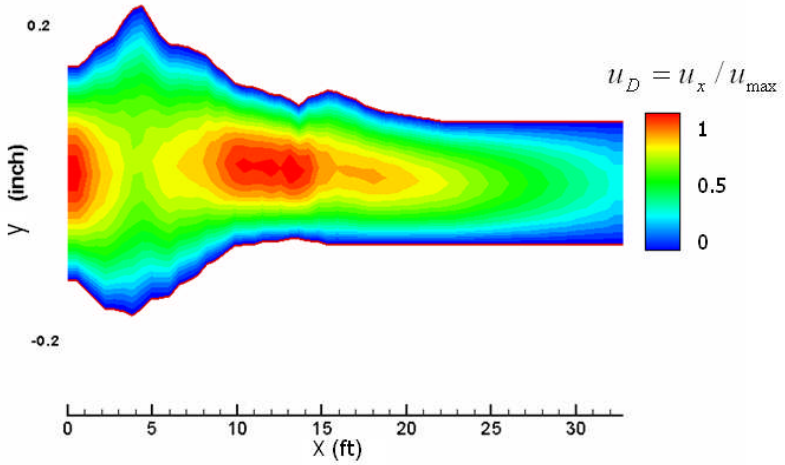


**Fig. 4.7 – The contour of velocity in the x direction for irregular fracture shape.**

Permeability heterogeneities lead to non-uniform leakoff velocity distribution on the fracture surfaces. Non-uniform leakoff velocity distribution affects fluid flow inside a fracture. Part of the leakoff acid etches fracture surfaces before entering into the

formation. Therefore, leakoff heterogeneities have large effects on final etching profiles. Fig. 4.8 shows how leakoff heterogeneities affect flow fields. Because of small fracture width, pressure change in the fracture width direction is negligible. Pressure distribution in the x direction is shown in Fig. 4.9. It is not a straight line because of leakoff, and its shape changes with the variation of leakoff distribution.

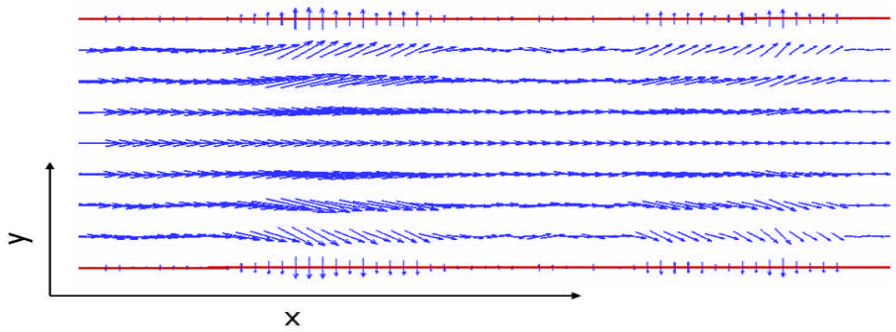


**Fig. 4.8 – Effect of non-uniform leakoff on velocity fields.**

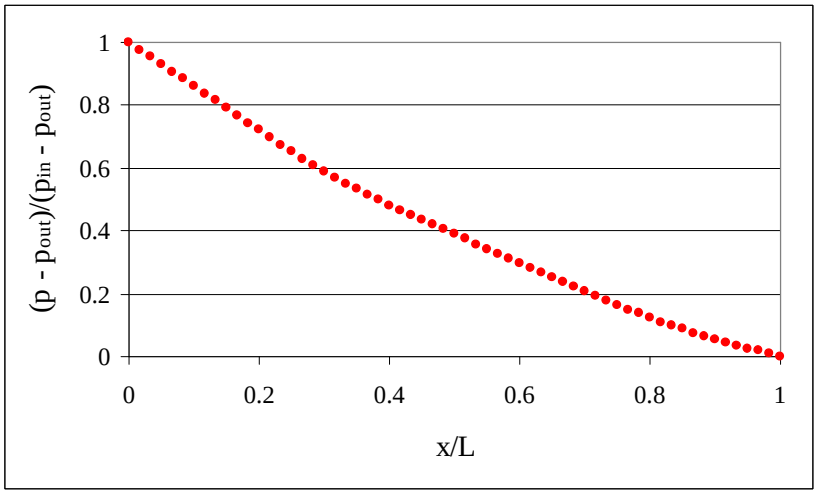


**Fig. 4.9 – Pressure drop behavior corresponding to Fig. 4.8.**

### 4.5.2 Acid Mass Conservation Checking

Acid/rock reaction occurs on the fracture surfaces, and leakoff varies with time, so acid concentration distribution is time dependent. Non-uniform acid/rock reaction makes fracture shape irregular, so no analytical solution is available to be compared with numerical solution. Material balance checking is a feasible way to validate the model. Acid injection is known because injection rate and concentration is known. The model can calculate the amount of acid inside the fracture, acid leakoff into the formation, acid consumption on the fracture surfaces caused by acid/rock reaction, and the amount of acid flowing out the fracture. Comparing the acid calculated by the model with known injection volume can validate the model indirectly. Fig. 4.10 shows material conservation error with time.

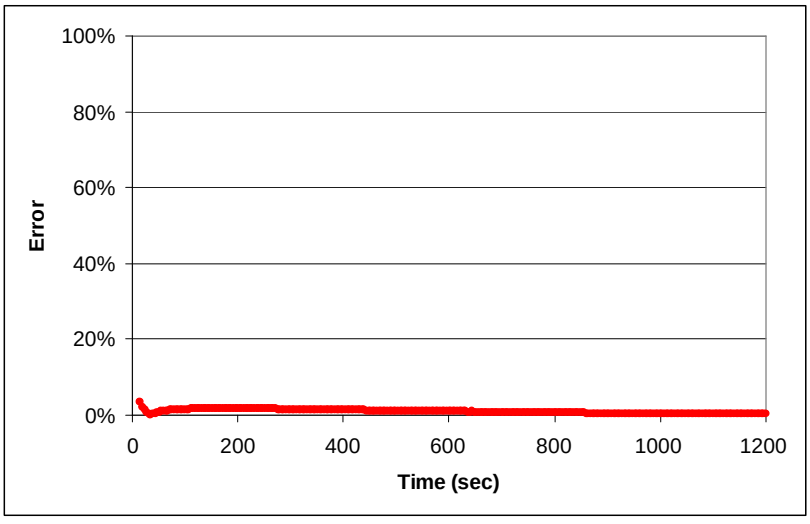


**Fig. 4.10 – Acid material conservation error with time.**

### 4.5.3 Comparison of Numerical Simulation to Experiment Results

The model was validated by simulating small-scale experimental results (Pournik, 2008). The fracture domain in the experiments is 7.5 inches long by 1.5 inches high. It is reasonable to assume a homogeneous mineralogy distribution for this small core sample, and thus, the etching profile is only controlled by the permeability distribution. The average permeability was measured in the experiment. The permeability distribution was generated synthetically with the measured average permeability by specifying the standard deviation and the correlation lengths. The comparison of experimental and simulation results is shown in Figs. 4.11, 4.12 and 4.13. Fig. 4.11 is the experimental etching profile, and Fig. 4.12 is the simulation etching profile. Fig. 4.13 shows the comparison of the etching depth. Except near the entrance where the hydrodynamics in the experimental configuration were not captured by the model, the comparison of overall etching depth between the experimental result and the model simulation shows a good match. Because the mineralogy in the simulation is assumed homogeneous and permeability distribution is a synthetic one instead of measured, the comparison just gives a general idea of how well the model works. Of significance is the match of average etching depth instead of the detailed etching profile. The acid is transported to the fracture surfaces by diffusion and convection. Convection is caused by acid leakoff into the formation. The empirical parameter $f$ , the percentage of leakoff acid to etching the fracture surfaces, is determined in experiments. The match of average etching depth shows a good estimation of this parameter in experiments.

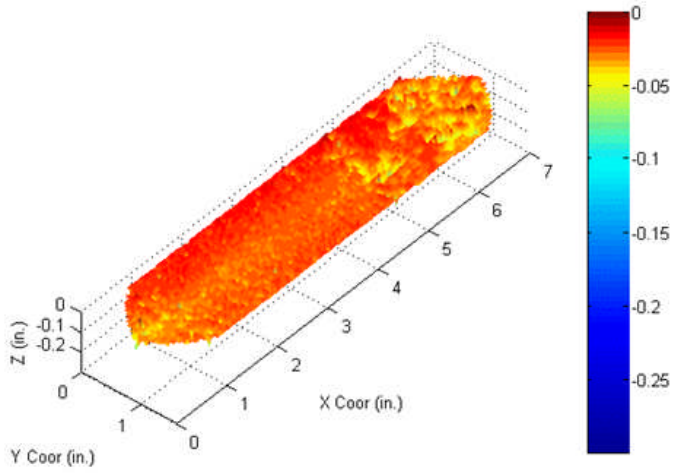


**Fig. 4.11 – Surface etching profile in experiment.**

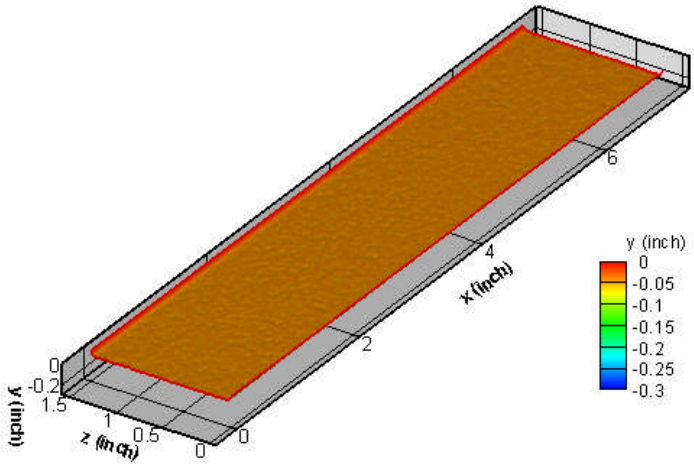


**Fig. 4.12 – Surface etching profile in simulation.**

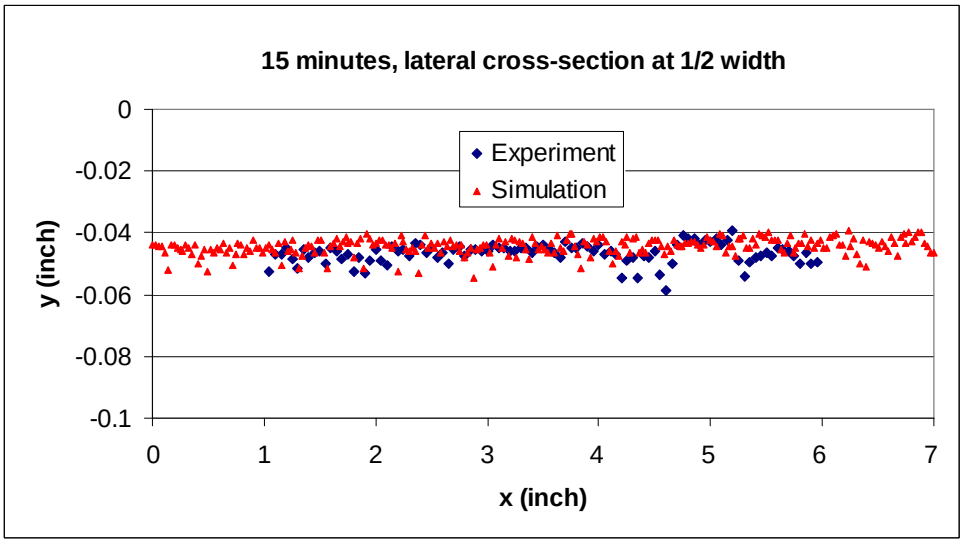


**Fig. 4.13 – The comparison of etched depth.**

# CHAPTER V

# RESULTS AND DISCUSSION*

## 5.1 Introduction

In this chapter, I analyze the effects of parameters such as permeability distribution, mineralogy distribution, temperature, acid properties, and initial fracture shape on etching patterns and corresponding conductivities. The focus is on the relationship between formation characteristics (permeability and mineralogy distributions) and etching patterns as well as fracture conductivity because they dominate etching patterns. The correlations of acid fracture conductivity and average fracture width at zero closure stress are developed based on extensive numerical experiments with the intermediate-scale model. Three categories are considered when developing the correlations considering the relative effects of leakoff and mineralogy distributions: leakoff distribution dominance, mineralogy distribution dominance, and competitive effects of leakoff and mineralogy distributions.

In the extensive numerical experiments, many realizations of permeability and mineralogy distributions are generated by varying statistical parameters. For the convenience of comparison and analysis, we make them dimensionless. The statistical properties of the permeability and mineralogy fields that were varied were the

* Part of this chapter is reprinted with permission from "Acid-Etched Channels in Heterogeneous Carbonates–A Newly Discovered Mechanism for Creating Acid Fracture Conductivity" by Mou, J., Zhu, D., and Hill, A.D., 2009. SPE © Paper SPE 119619 presented at the SPE Hydraulic Fracturing Technology Conference, The Woodlands, TX.

normalized correlation lengths in the $x$ and $z$ directions and the normalized standard deviation of the natural log of permeability. These are defined as follows: $\lambda_{D,x} = \lambda_x / L$ and $\lambda_{D,z} = \lambda_z / H$ for both permeability and mineralogy distributions, where $\lambda_x$ and $\lambda_z$ are correlation length in the $x$ and $z$ directions, $\sigma_D = \frac{\sigma(\ln(k))}{\ln(\bar{k})}$. $\sigma(\ln(k))$ is standard deviation of $\ln(k)$, and $\bar{k}$ is average permeability. When the average permeability is 1 md, $\sigma_D = \frac{\sigma(\ln(k))}{\ln(10)}$.

When calculating acid fracture conductivity based on etching patterns output from the intermediate-scale model, we bring the two surfaces into contact (zero closure stress). The conductivity calculation for the irregular fracture shape is described in Appendix C.

In the contour plots of surface etching profiles such as in Fig. 5.1, the unit is feet in the x and z directions and millimeters in the y direction. That is, in visualization, the fracture width direction is greatly enlarged to see the fracture surface etching profiles clearly.

To analyze how conductivity changes with etching patterns and formation characteristics, we make conductivity plots such as the example in Fig. 5.2. The x axis is the average fracture width obtained by dividing the fracture volume by the fracture surface area. The y axis is conductivity at zero closure stress with the two surfaces in contact. The cubic law is the conductivity calculated for flow between smooth parallel plates with a width equal to the average width of the rough-walled fracture. The reason

why it is called cubic law is that the conductivity is proportional to the cube of the width. On a log-log plot, the cubic law is a straight line. Using the cubic law and the average fracture width, we can generate a so called base line. In a simulation case, we generate many points on the plot with one point corresponding to one acid contact time. Using least-squares fitting method, we generate a straight trend line for one simulation case. It is found that the lines are approximately parallel to the base line. By comparing the conductivity lines to the base lines, we can see how fracture roughness affects conductivity and how the roughness makes conductivity deviate from the cubic law.

### 5.2 Influence of Initial Fracture Configuration

Before using the intermediate-scale model to simulate an acid injection processes, we need to initialize the fracture width distribution and shape. In acid fracturing, a fracture is created by hydraulic pressure before acid injection. The fracture width is non-uniform because of non-uniform stress and rock properties distributions, but the width variation is small compared to the width, which is not the case in a natural fracture where the fracture width is small and the width variation is large relative to the width. Therefore, it is reasonable to assume uniform initial fracture width distribution in the intermediate-scale model because it is just a small part of a whole fracture. Uniform fracture width distribution does not necessarily mean smooth fracture surfaces. Seen in large scale, fracture surfaces are flat, while in local scale they are rough. Whether the effects of the initial roughness of the fracture surfaces are important or not can be determined by comparing the results of smooth initial fracture surfaces and rough initial fracture surfaces.

To investigate the effects of rough initial fracture shape, we simulated two cases with the same parameters except for one case with rough initial surfaces but uniform width distribution and one case with smooth surfaces as shown in Fig. 5.1. Because fracture width is uniform, the two rough fracture surfaces have the same shape.

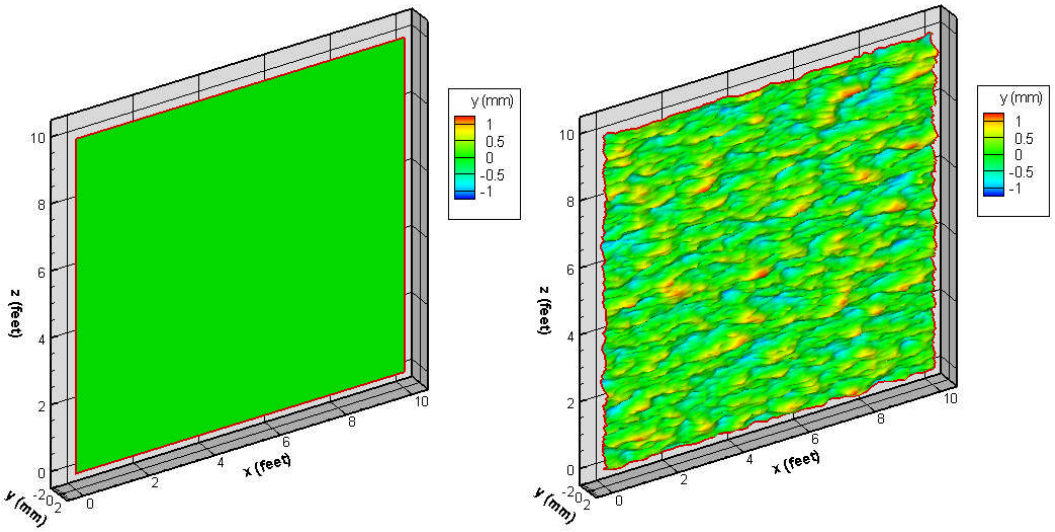


**Fig. 5.1 – Initial fracture surface shapes (left: smooth surface, right: rough surface).**

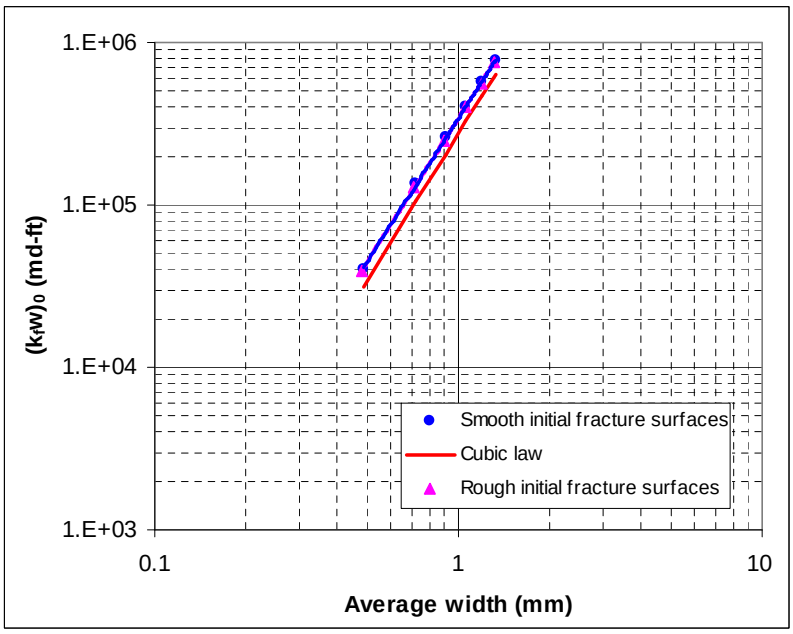


**Fig. 5.2 – Conductivity comparison for initial smooth and rough fracture surfaces.**

Fig. 5.2 shows that rough and smooth initial fracture surfaces give negligible differences on the conductivity plot. Therefore, in the following study we use a regular fracture shape as the initial fracture shape.

### 5.3 Influence of Leakoff

The effect of leakoff on acid fracturing is embodied in two aspects. Firstly, leakoff influences the flow fields, and hence affects acid concentration distribution and limits live acid penetration distance. Secondly, part of the acid will etch fracture surfaces before entering into the formation. Therefore, final etching profiles depend on leakoff distribution. How leakoff affects flow fields, acid concentration distribution, and final etching profiles can be simulated by the model. The percentage of the leakoff acid that etches the surface, which needs to be input in the model, however, needs to be

determined by experiments. In experiments, some were done with leakoff, and others without leakoff with the same conditions. The etching depth difference is caused by leakoff because other conditions are the same except leakoff. Although we can keep experimental operation conditions the same, we can not ensure all conditions the same. For example, core samples may be different. Although core samples are cut from the same big rock, they may have different properties. The percentage determined from experiments is just a possible range. Based on experiment results, the percentage is about 30%. Leakoff distribution depends on permeability and mineralogy distributions. Mineralogy affects leakoff by wormholing, which will be discussed next.

### 5.3.1 Influence of Wormholes

In acid fracturing, leakoff limits live acid penetration distance and weakens rock strength near fracture surfaces. Part of the leakoff acid etches fracture surfaces before entering into the formation, so leakoff will affect the surface etching pattern. Wormholes, generated by acid leakoff, have great influence on leakoff in turn. Wormhole effect is different for gas reservoirs, oil reservoirs, dolomite, and limestone. According to Hill et al. (1995), the ratio of leakoff coefficient with wormholes and without the wormhole effect is

$$\frac{C_{wh}}{C} = \frac{Q_{ibt}}{Q_{ibt}-1}\frac{\sqrt{4R_C\frac{Q_{ibt}-1}{Q_{ibt}}+1}-1}{\sqrt{4R_C+1}-1} \quad \text{..... (5. 1)}$$

where $Q_{ibt}$ is breakthrough pore volume for acid in a core flood; $R_C$ is the square of the ratio of the compressibility fluid loss coefficient and viscosity fluid loss coefficient.

$$R_C = \frac{2}{\pi}\frac{\mu_f}{\mu} c_t \Delta p \quad \text{..... (5. 2)}$$

The assumption is made in the formula that the filter cake resistance is neglected $C_w >> C_v$ and $C_c$ because acid etching on the fracture surfaces makes it difficult to form filter cake.

Two parameters $R_C$ and $Q_{ibt}$ determine the leakoff increase caused by wormholes. $R_C$ is a measure of the importance of viscous fluid loss coefficient relative to the compressibility fluid loss coefficient. $Q_{ibt}$ indicates how rapidly wormholes grow in the invaded zone. The necessary condition where wormholing increases leakoff significantly is that $R_C > 1$ and small $Q_{ibt}$. In oil reservoirs with typical compressibility, $R_C << 1$, so wormholing effect is negligible. In gas reservoirs, total compressibility is found to range from $2 \times 10^{-5}$ psi$^{-1}$ $\sim 10^{-3}$ psi$^{-1}$ (Gidley et al., 1989). In typical fracturing situations, since $R_C > 1$, $Q_{ibt}$ is the factor determining the wormholing effects. In dolomite, $Q_{ibt} >> 1$, and wormholing has an insignificant effect on acid leakoff. In limestone, $Q_{ibt}$ is close to 1 under optimal injection conditions, and the wormhole effect on acid leakoff is pronounced.

### 5.3.2 Permeability Distribution Effect

The permeability distribution affects surface etching profiles via acid leakoff because the permeability distribution determines the leakoff distribution. Acid leakoff not only limits live acid penetration distance, but also affects fracture surface profiles

because a part of the leakoff acid etches the surfaces before entering into the formation. When analyzing permeability distribution effect, a uniform mineralogy distribution is used to eliminate mineralogy effects. There are three cases, in which leakoff distribution dominates surface etching patterns, reservoirs with high leakoff, reservoirs with medium leakoff and the uniform mineralogy distribution (100% limestone or dolomite). It is found that when leakoff coefficient is higher than about $0.004\,\text{ft}/\sqrt{\text{min}}$, leakoff distribution dominates the etching patterns. In order to check whether the mineralogy distribution effect can be neglected or not for the cases with a high leakoff rate, we ran some cases with different limestone and dolomite percentage. Fig. 5.3 shows the etching profiles for 20% and 80% limestone with injected straight acid. The etching depth contour maps show very little etching depth difference. Conductivities for different percentages of limestone and dolomite are shown in Fig. 5.4, indicating the conductivities do not change with mineralogy. Similar results are obtained for gelled acid injection cases as shown in Fig. 5.5 and Fig. 5.6. Therefore, for cases with leakoff distribution dominating surface etching patterns, mineralogy effects can be neglected.

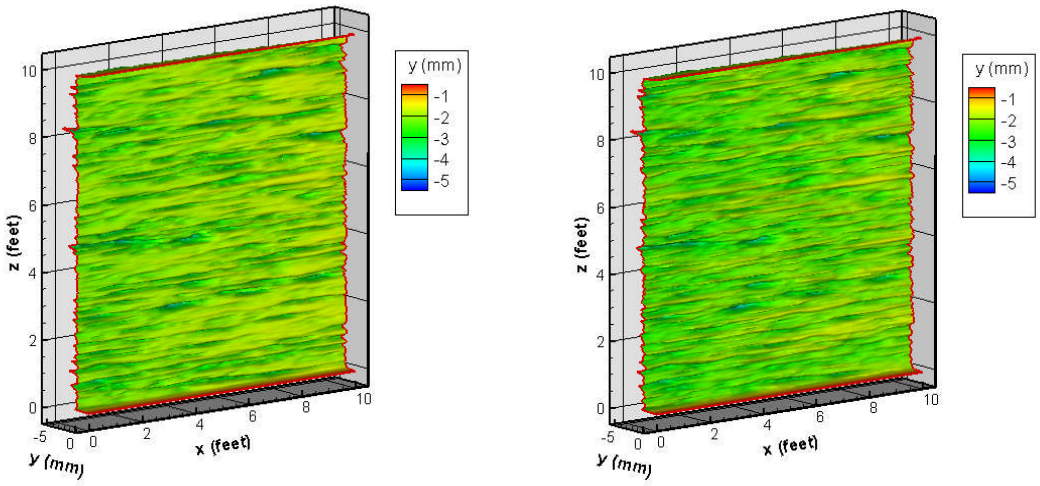


(a) 20% limestone (b) 80% limestone

**Fig. 5.3 – Etching patterns for permeability distribution dominance (straight acid).**

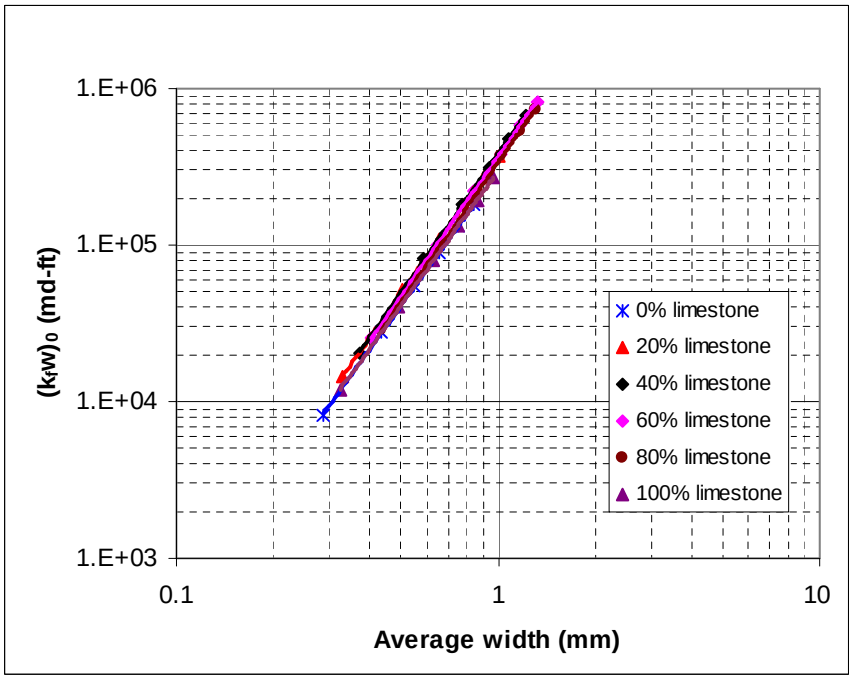


**Fig. 5.4 – Conductivities for permeability distribution dominance (straight acid).**

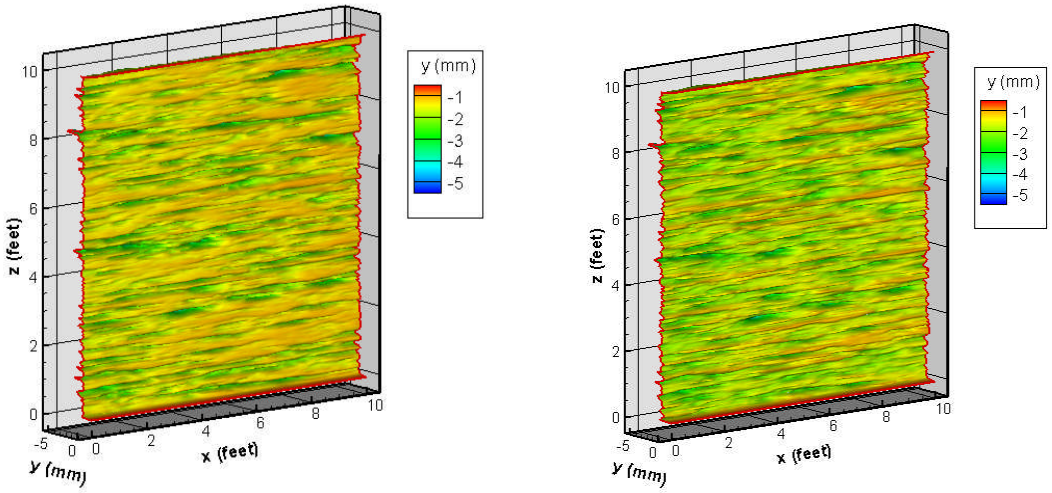


(a) 20% limestone (b) 80% limestone

**Fig. 5.5 – Etching patterns for permeability distribution dominance (gelled acid).**

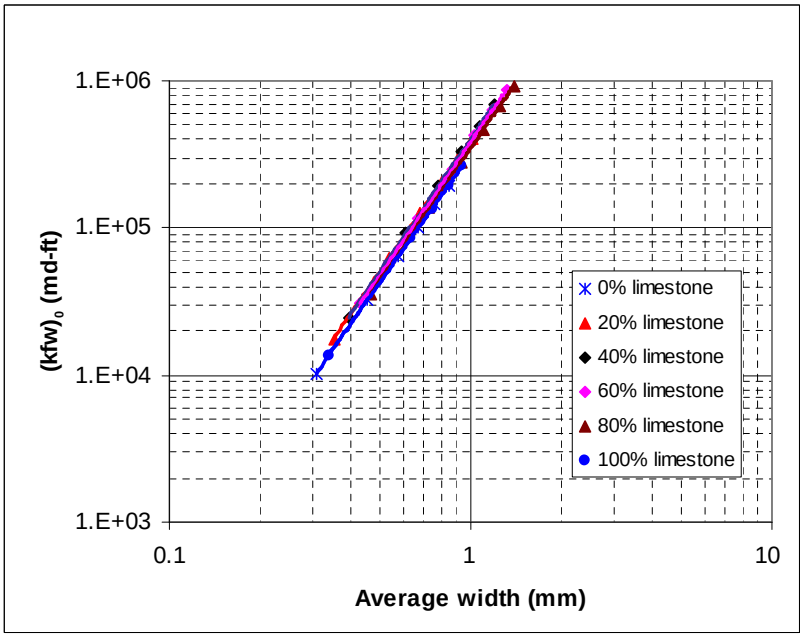


**Fig. 5.6 – Conductivities for permeability distribution dominance (gelled acid).**

When analyzing the effects of one parameter, we fix all other parameters. Firstly, we analyze the effect of horizontal correlation length of permeability on etching patterns and conductivity.

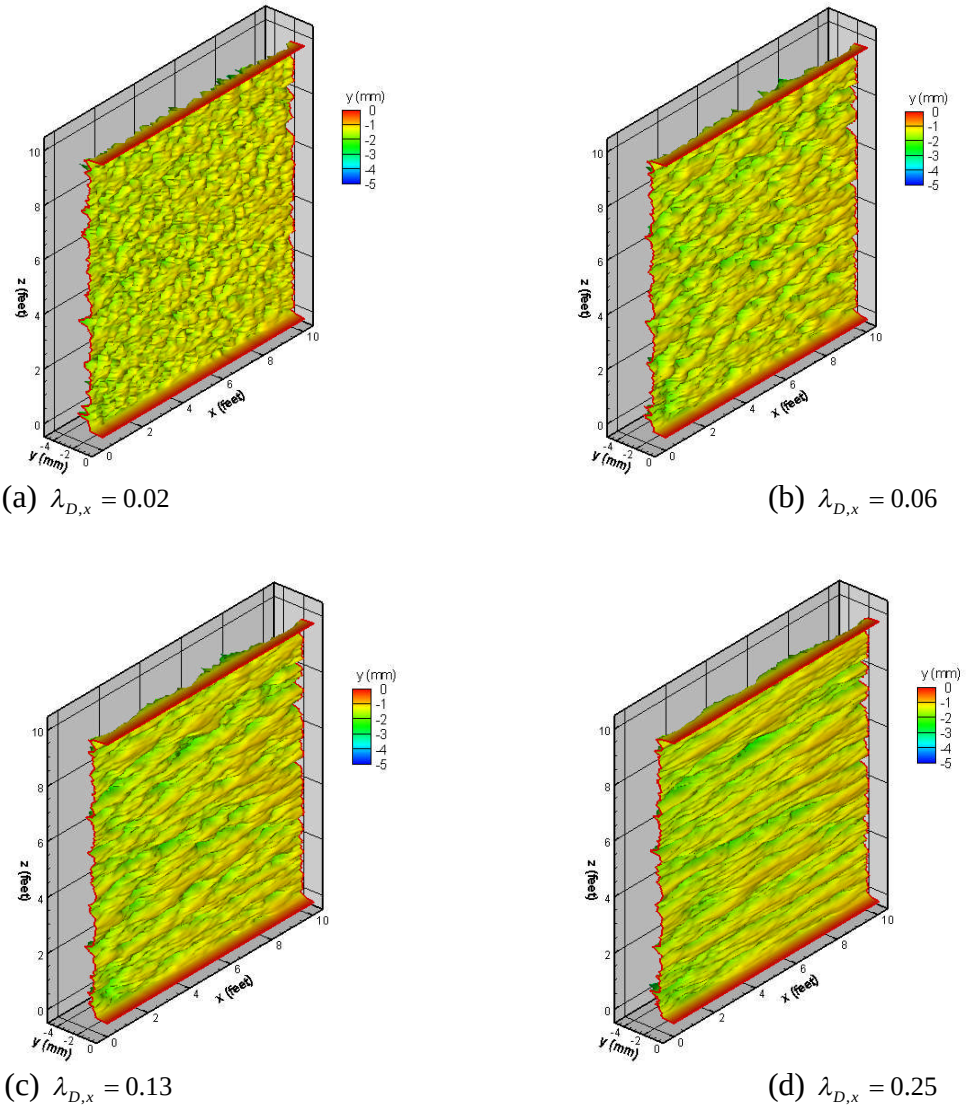


(a) $\lambda_{D,x} = 0.02$ (b) $\lambda_{D,x} = 0.06$

(c) $\lambda_{D,x} = 0.13$ (d) $\lambda_{D,x} = 0.25$

**Fig. 5.7 – Effects of horizontal correlation length of permeability distribution on etching patterns.**

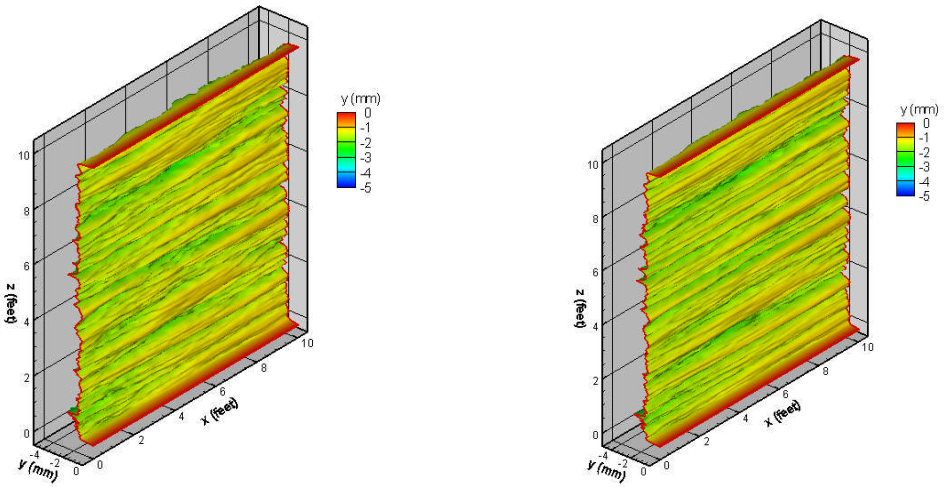


(e) $\lambda_{D,x} = 0.5$ (f) $\lambda_{D,x} = 1$

**Fig. 5.7 – Continued.**

In Fig. 5.7, we fix $\lambda_{D,z} = 0.02$ and $\sigma_D = 0.5$ for permeability. From Fig. 5.7 (a) to (f), $\lambda_{D,x}$ of permeability are 0.02, 0.06, 0.13, 0.25, 0.5, and 1 respectively. Distinct etching patterns are obtained as seen in the figure. Small horizontal correlation length of permeability (Fig. 5.7 (a) and (b)) gives rise to almost random permeability distributions, which cause random and isolated void space distributions after acid attack. Increasing horizontal correlation length makes void spaces arranged more favorably to connect to each other. Large horizontal correlation lengths (Fig. 5.7 (e) and (f)) cause void spaces to be connected, forming channels from the inlet to the outlet of the fracture.

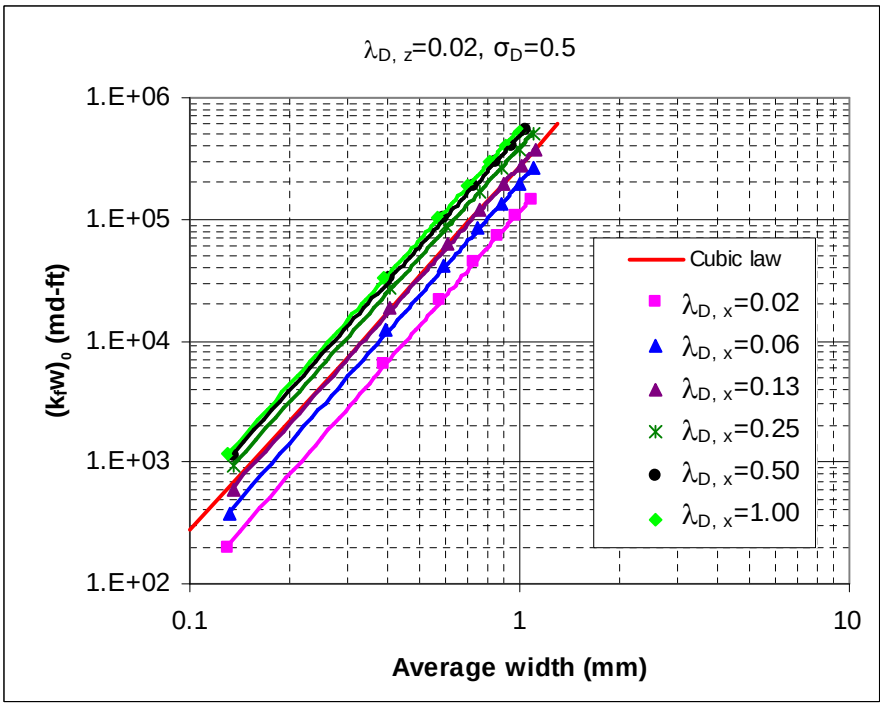


**Fig. 5.8 – Conductivities for different horizontal permeability correlation lengths ($\lambda_{D,x} = 0.02$ and $\sigma_D = 0.5$ for permeability distribution).**

When bringing two rough fracture surfaces into contact, some places are closed, and some places are open. Closed places have the permeability of the matrix. Fluid flow in deep channels causes negligible pressure drop, while the flow in closed parts causes a large pressure drop. For fluid flow in a fracture, most of the pressure drop is caused by the closed parts. If there are channels extending from the inlet to the outlet, a small pressure gradient gives a large flux, which means a large conductivity for the fracture. Fig. 5.7 shows that, when increasing $\lambda_{D,x}$ from 0.02 to 1, more void spaces are connected to each other to form channels, and corresponding conductivity lines shown in Fig. 5.8 move upward from below the base line to above the base line. When $\lambda_{D,x}$ is about 0.15,

the conductivity line coincides with the cubic law line for these cases. If $\lambda_{D,x}$ is smaller than 0.15, conductivity lines are below the base line.

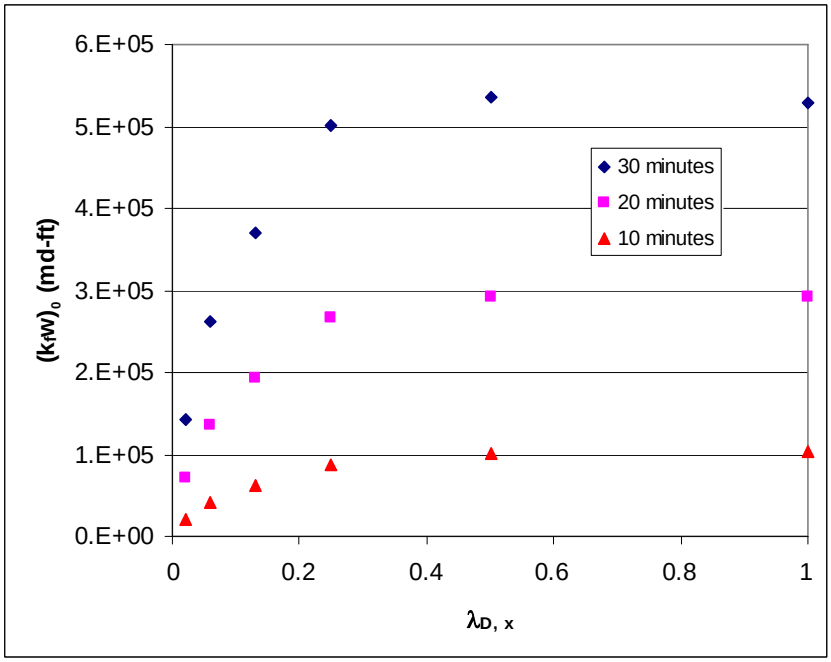


**Fig. 5.9 – Conductivity increases with horizontal correlation length ($\lambda_{D,x} = 0.02$ and $\sigma_D = 0.5$ for permeability distribution).**

Fig. 5.9 shows how conductivity increases with increasing horizontal correlation length for three acid contact times. Conductivity increases very rapidly when increasing horizontal correlation length from a very small value, and then levels off when $\lambda_{D,x}$ approaches about 0.5. After 0.5 of $\lambda_{D,x}$, increasing $\lambda_{D,x}$ does not increase conductivity because the channels are already continuous from inlet to outlet when $\lambda_{D,x}$ is about 0.5.

When analyzing the effects of the vertical correlation length of permeability, we fix the horizontal correlation length and the standard deviation of permeability. Fig. 5.10 shows the etching patterns for different $\lambda_{D,z}$ with fixed $\lambda_{D,x} = 0.5$ and $\sigma_D = 0.5$. Because of high horizontal correlation length, channels are obtained for low vertical correlation length. As the vertical correlation length increases, channels become wider and wider, and then disappear.

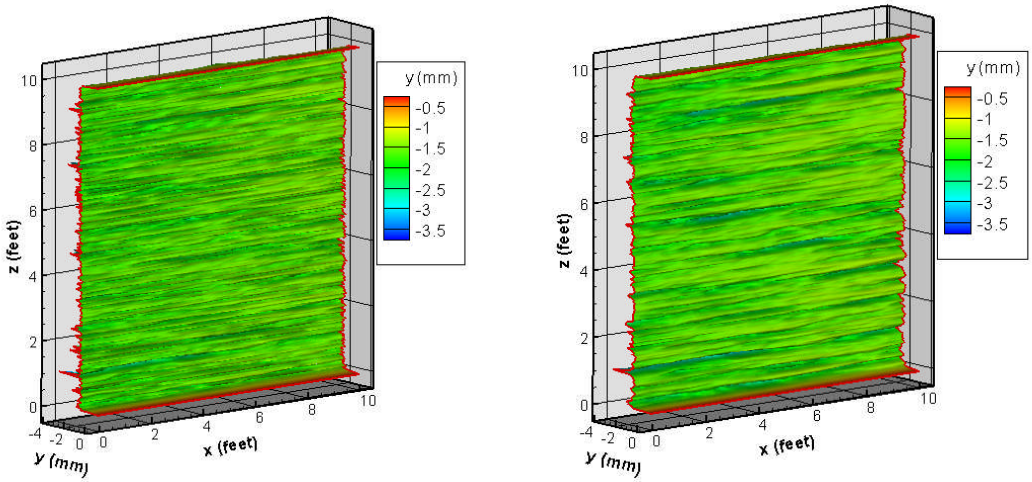


(a) $\lambda_{D,z} = 0.004$ (b) $\lambda_{D,z} = 0.016$

**Fig. 5.10 – Effects of vertical correlation length of permeability distribution on etching patterns ($\lambda_{D,x} = 0.5$ and $\sigma_D = 0.5$ for permeability distribution).**

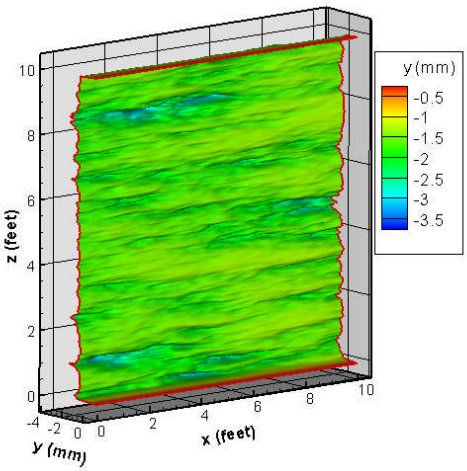


(c) $\lambda_{D,z} = 0.06$

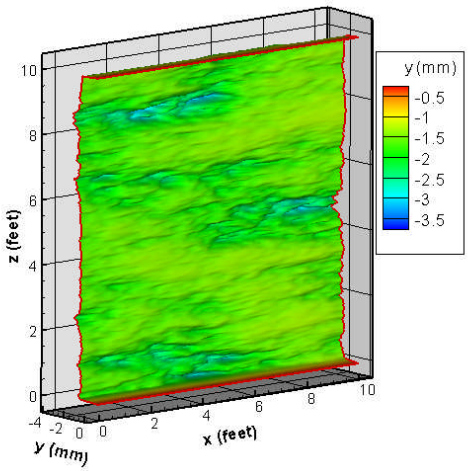


(d) $\lambda_{D,z} = 0.13$

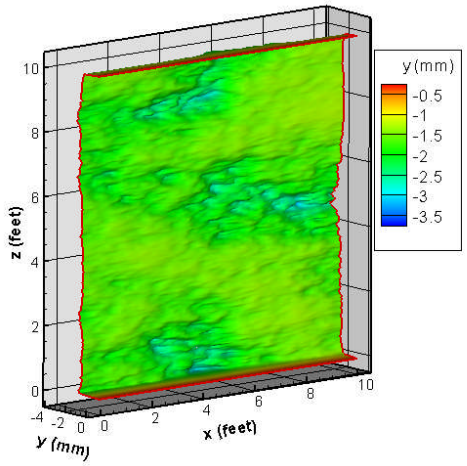


(c) $\lambda_{D,z} = 0.25$

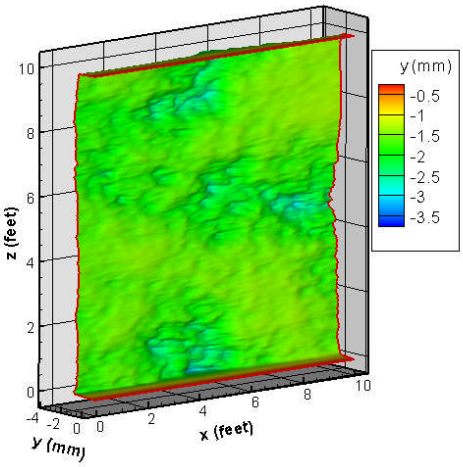


(d) $\lambda_{D,z} = 0.375$

**Fig. 5.10 – Continued.**

Fig. 5.11 shows the corresponding conductivities. We can see that the conductivity lines move downward from above the cubic line to below the cubic law line when increasing $\lambda_{D,z}$. Generally, reservoirs have a higher horizontal correlation length than the vertical correlation length because the bedding direction is generally horizontal, so all the cases have $\lambda_{D,z}$ smaller than $\lambda_{D,x}$.

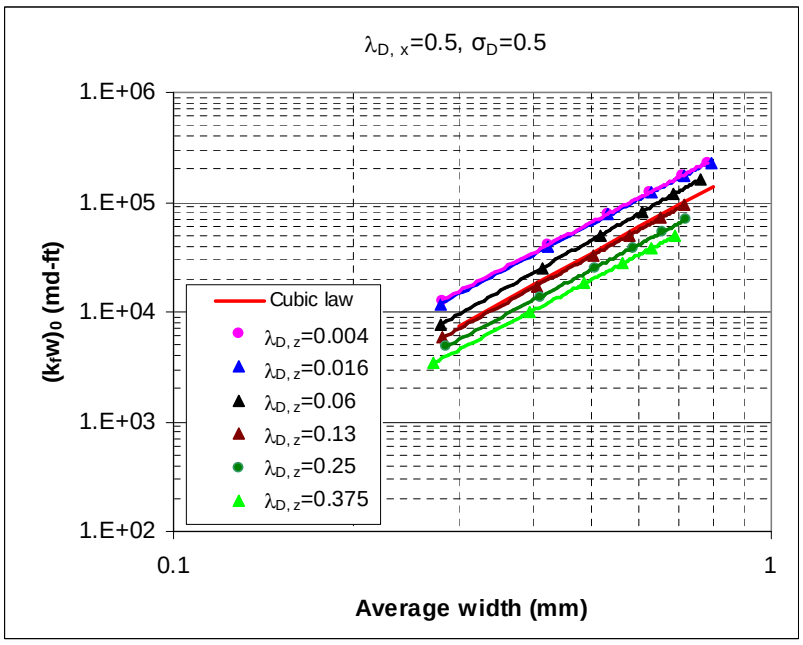


**Fig. 5.11 – Conductivities for different vertical permeability correlation lengths ($\lambda_{D,x} = 0.5$ and $\sigma_D = 0.5$ for permeability distribution).**

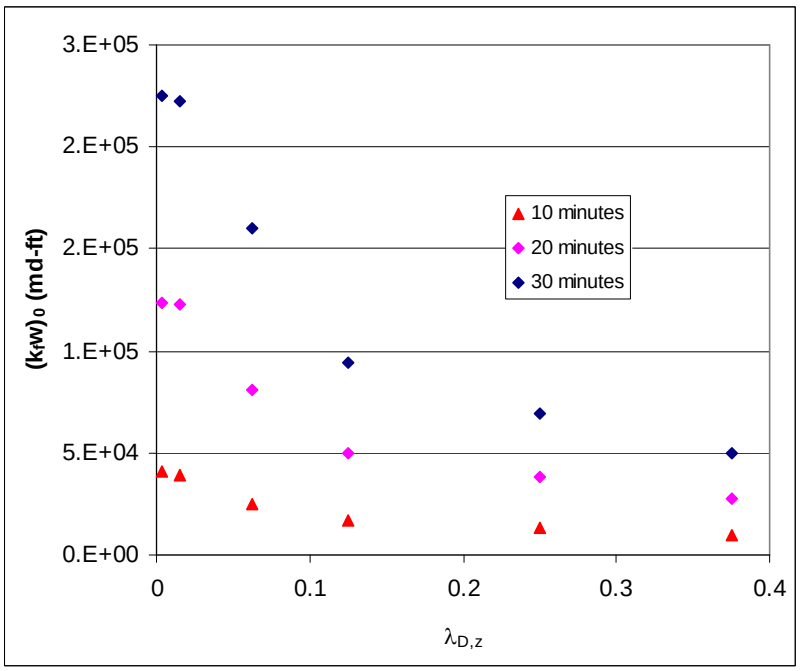


**Fig. 5.12 – Conductivity decreases with vertical correlation length ($\lambda_{D,x} = 0.5$ and $\sigma_D = 0.5$ for permeability distribution).**

Fig. 5.12 shows conductivities decrease with $\lambda_{D,z}$ for three acid contact times. Conductivity decreases rapidly with increasing $\lambda_{D,z}$ when $\lambda_{D,z}$ is smaller than about 0.12, while decreasing slowly with increasing $\lambda_{D,z}$ when $\lambda_{D,z}$ is higher than about 0.12.

The standard deviation, $\sigma_D$, of the natural log of permeability indicates the degree of heterogeneity of permeability distributions. How $\sigma_D$ affects etching profiles and corresponding conductivities depends on the spatial distribution of permeability. That is, for the same permeability standard deviation, different horizontal and vertical correlation lengths give different etching profiles and conductivities. Two categories are analyzed here: high and low horizontal correlation lengths of permeability distribution. Fig. 5.13 shows the etching profiles for $\sigma_D$ of 0.1, 0.3, 0.5, and 0.7 with $\lambda_{D,x}$ and $\lambda_{D,z}$ of 0.5 and 0.02. $\lambda_{D,x} = 0.5$ indicates a high horizontal correlation length, in which case void spaces are connected to each other to form channels in the horizontal direction. The larger the standard deviation, the deeper the channels generated. Corresponding conductivities are shown in Fig. 5.14. We can see that all conductivity lines are above the cubic law line. Because of high correlation strength in the horizontal direction, roughness is arranged orderly to form channels. The larger $\sigma_D$, the deeper the channels are, and the higher the conductivity.

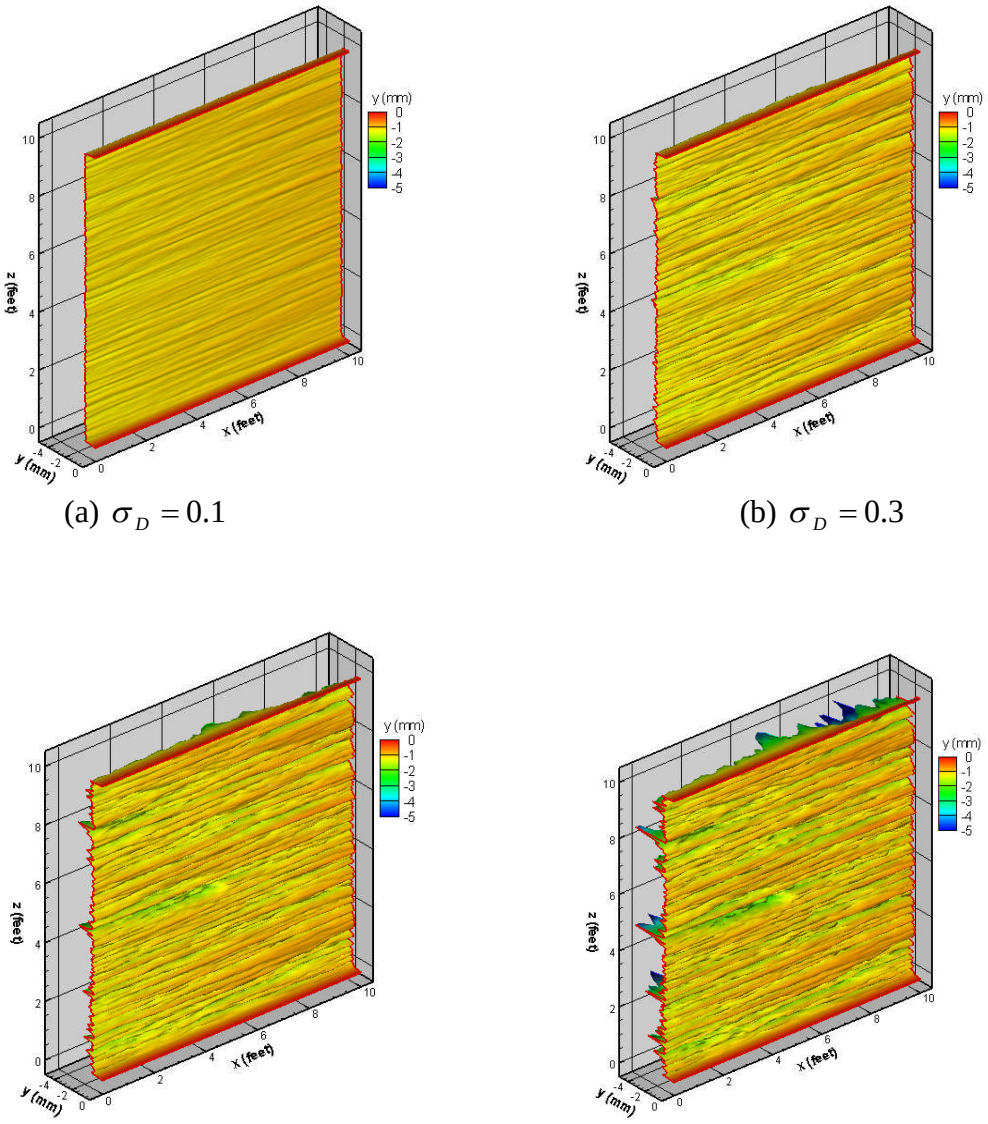


(a) $\sigma_D = 0.1$ (b) $\sigma_D = 0.3$

(c) $\sigma_D = 0.5$ (d) $\sigma_D = 0.7$

**Fig. 5.13 – Effects of standard deviation of permeability distribution on etching patterns ( $\lambda_{D,x} = 0.5$ and $\lambda_{D,z} = 0.02$ for permeability distribution).**

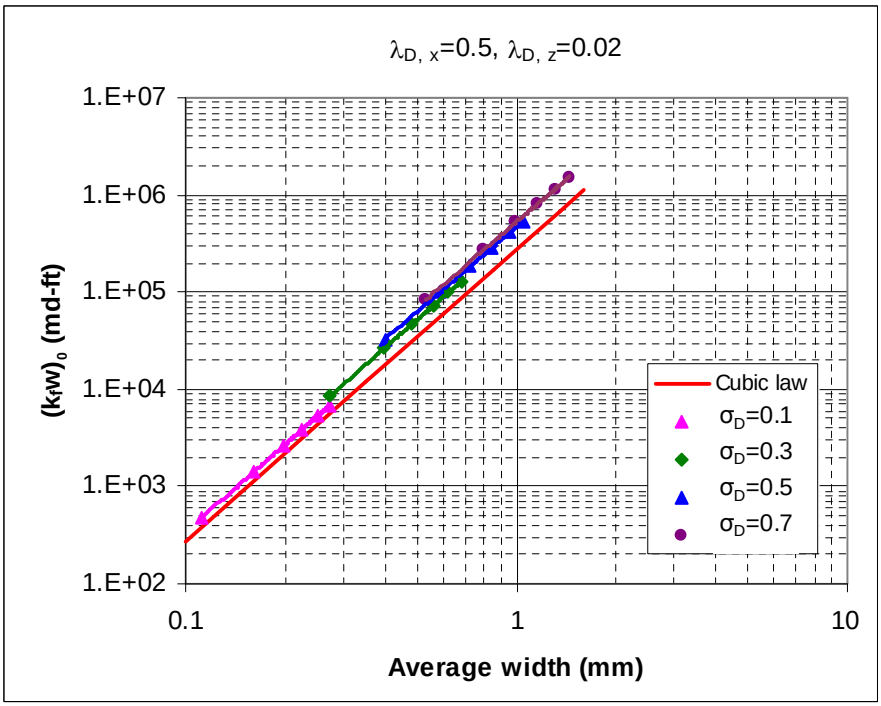


**Fig. 5.14 – Effects of standard deviation of permeability distribution on conductivity ( $\lambda_{D,x} = 0.5$ and $\lambda_{D,z} = 0.02$ for permeability distribution).**

Fig. 5.15 shows etching patterns for cases with $\lambda_{D,x}$ and $\lambda_{D,z}$ of 0.06 and 0.02. Because of small correlation length in the horizontal and vertical directions, the void spaces are randomly distributed and isolated from each other. No channels extend from the inlet to the outlet. Fluid flow in these kinds of fractures caused a large pressure drop, thus a small conductivity is obtained. We can see from Fig. 5.16 that all conductivity lines are below the base line. The larger the $\sigma_D$, the rougher surfaces we get, and the higher the conductivity.

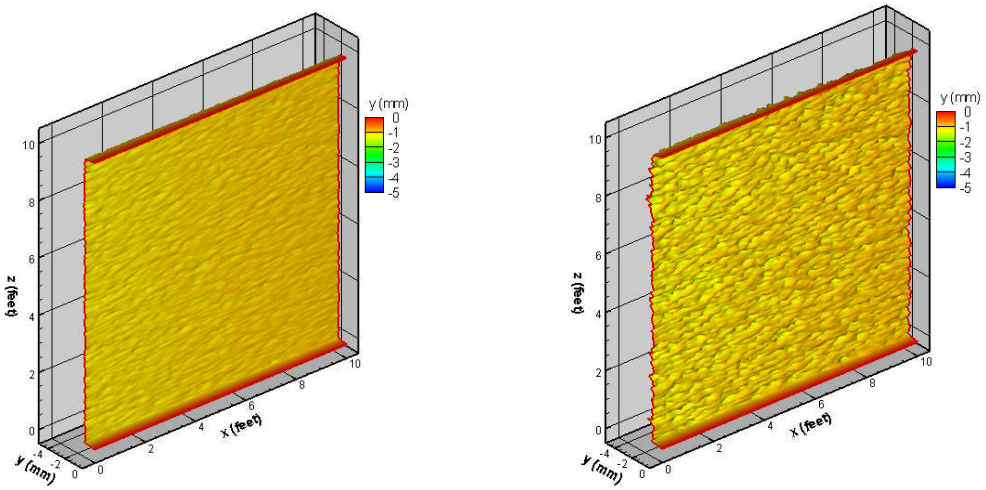


(a) $\sigma_D = 0.1$ (b) $\sigma_D = 0.3$

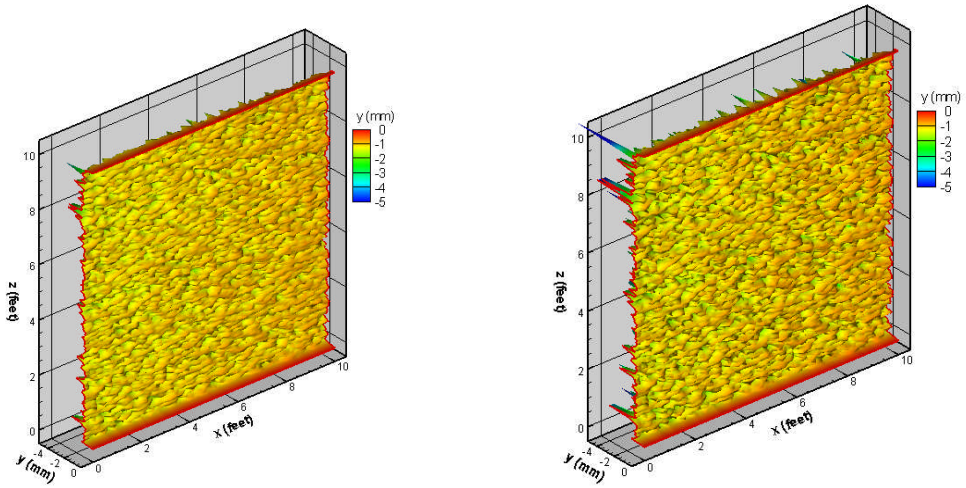


(d) $\sigma_D = 0.5$ (d) $\sigma_D = 0.7$

**Fig. 5.15 – Effects of standard deviation of permeability distribution on etching patterns ( $\lambda_{D,x} = 0.06$ and $\lambda_{D,z} = 0.02$ for permeability distribution).**

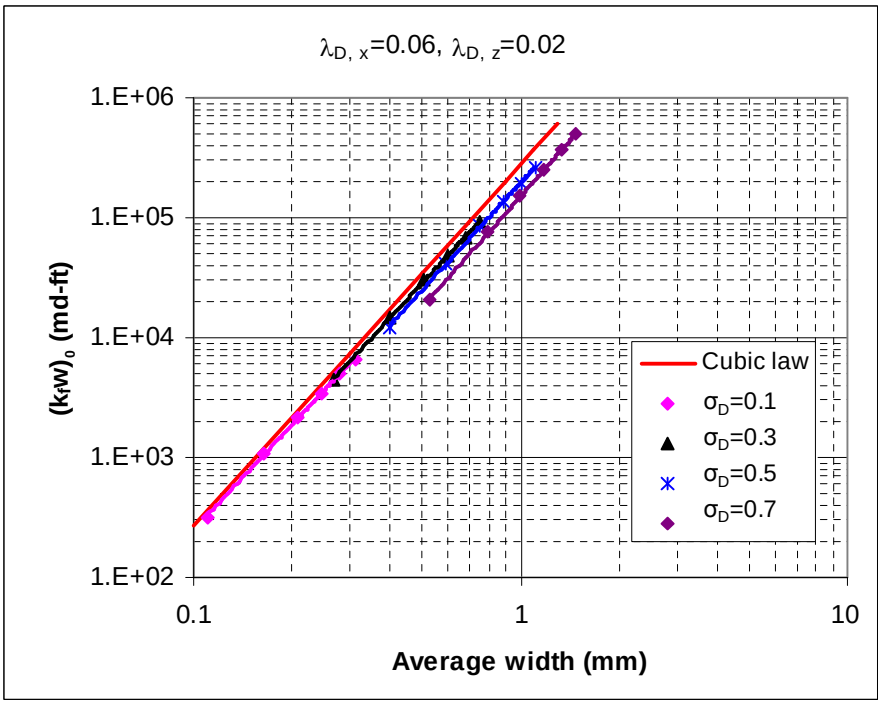


**Fig. 5.16 – Effects of standard deviation of permeability distribution on conductivity ( $\lambda_{D,x} = 0.06$ and $\lambda_{D,z} = 0.02$ for permeability distribution).**

## 5.4 Influence of Mineralogy

When analyzing the effects of mineralogy distribution, leakoff is shut off to isolate the effect of permeability distribution, which is the case where permeability is very low so that mineralogy distribution has the dominant effect on etching patterns and corresponding conductivities, for example, leakoff coefficient less than about $0.0004\ \text{ft}/\sqrt{\text{min}}$ under typical operation conditions.

From the perspective of chemical composition, carbonate reservoirs are comprised of limestone, dolomite, and HCl insoluble materials (anhydrite, quarts, and shale). In this study, just limestone and dolomite are considered. Mineralogy determines the acid/rock reaction rate, and the reaction rate determines acid concentration on the

fracture surfaces. Acid transported to the fracture surfaces by diffusion is dependent on the acid concentration gradient. In the end, mineralogy affects the acid transportation rate by diffusion. Overall reaction rate depends on mass transfer and surface reaction rate, the slower one of which will determine the overall reaction rate. Limestone reacts with acid faster than dolomite, so more rock is dissolved where limestone lies than where dolomite lies, which results in rough etched fracture surfaces. According to Blatt (1980), most carbonate sediments show laminations. That is, the mineralogy distribution has a high correlation length in the bedding direction. Carbonate rocks can change abruptly from dolomite to limestone. Therefore, we use a strong horizontal correlation length to generate mineralogy distributions. An example of a mineralogy distribution is shown in Fig. 5.17. Because of high horizontal correlation length for mineralogy distribution, channels are obtained when mineralogy distribution dominates the surface etching patterns. The depths of the channels depend on temperature, which affects the surface reaction rate and acid diffusion coefficient (Conway et al., 1999). The temperature effect on acid diffusion coefficient is discussed in the later section. Here we use the same acid diffusion coefficient of $6\times10^{-9} m^2/s$ for both temperatures. That is, the temperature dependence of the acid diffusion coefficient is neglected here. When temperature is high, surface reaction rates of limestone and dolomite are both so high that the overall reaction rate is mass transfer limited, in which cases mineralogy cause very shallow channels as shown in Fig. 5.18 for a temperature of 210 $^{o}$F. With temperature decrease, the overall reaction rate shifts from mass transfer limited to surface reaction rate limited, so that the reaction rate difference of limestone and

dolomite has more and more effect on the etching depth. Fig. 5.19 shows a case of deep channels with a temperature of 150 $^{o}$F. Therefore, to get deep channels caused by mineralogy distribution, we low temperature is desired.

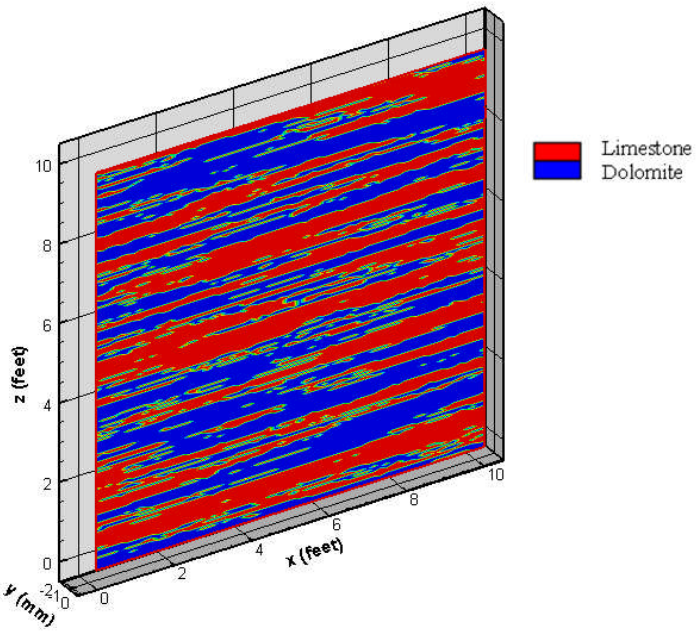


**Fig. 5.17 – Mineralogy distribution.**

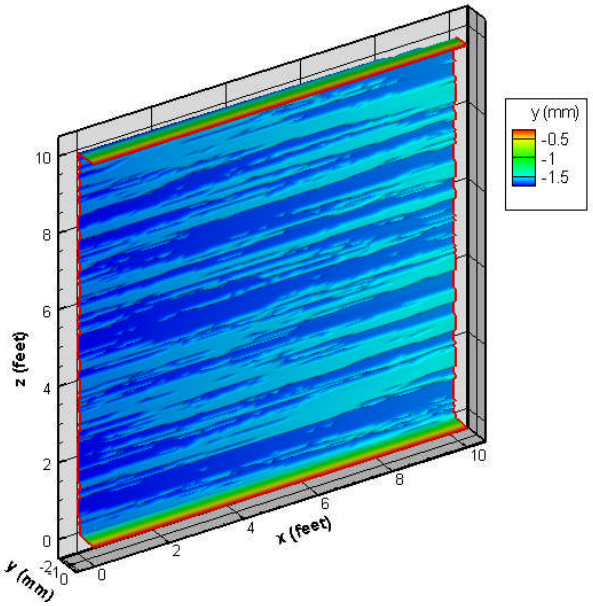


**Fig. 5.18 – Etching pattern at a temperature of 210 $^{o}$F**

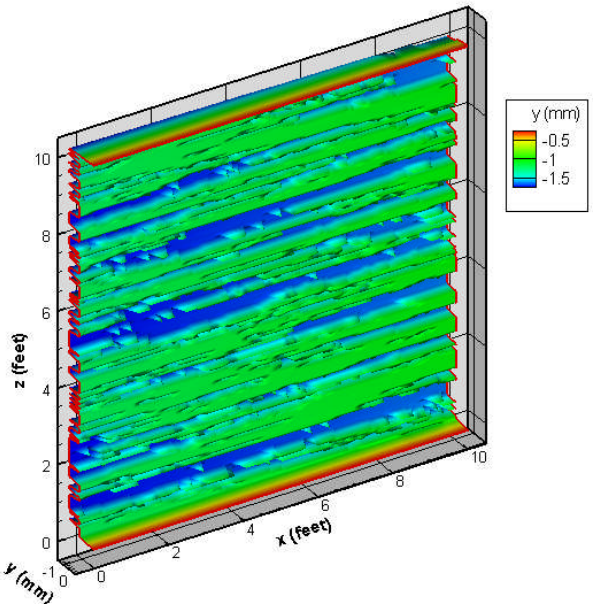


**Fig. 5.19 – Etching pattern at a temperature of 150 $^{o}$F.**

How the vertical correlation length of mineralogy distribution affects etching patterns and corresponding conductivities is investigated by using cases with 50% limestone and 50% dolomite. Fig. 5.20 shows the etching patterns for different vertical correlation lengths of mineralogy distribution. A small vertical correlation length leads to narrow channels as in Fig. 5.20 (a). Increasing vertical correlation makes channels wider and wider. A high vertical correlation length makes the channels so wide that channels disappear as in Fig. 5.20 (f). However, the vertical correlation length of mineralogy distribution does not affect conductivity at zero closure stress as shown in Fig. 5.21, although the width of channels will affect surface deformation under closure stress.

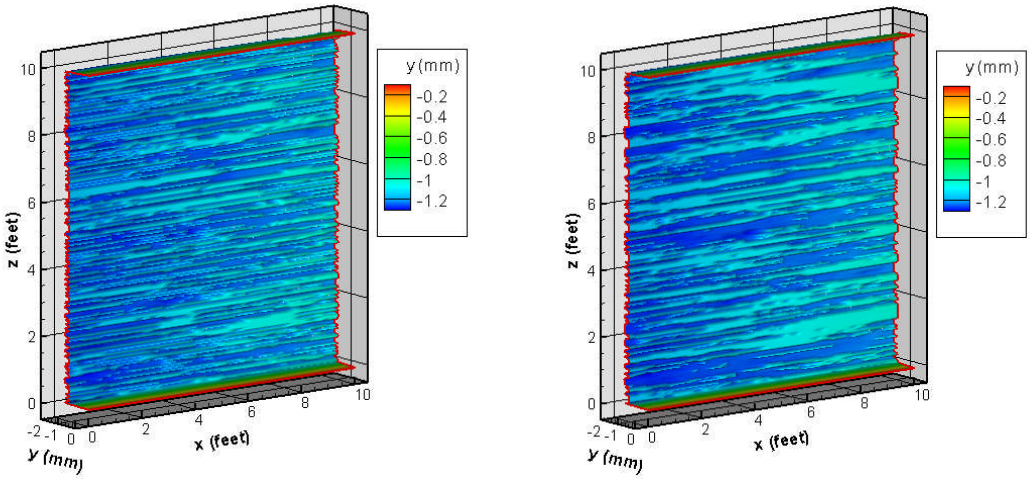


(a) $\lambda_{D,z} = 0.004$ (b) $\lambda_{D,z} = 0.016$

**Fig. 5.20 – Etching patterns for different vertical correlation lengths of mineralogy distribution.**

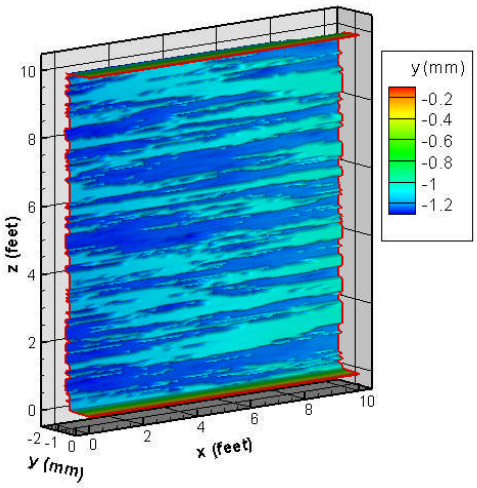


(a) $\lambda_{D,z} = 0.03$

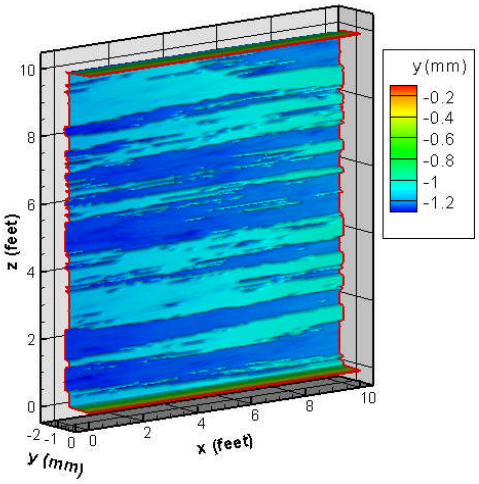


(b) $\lambda_{D,z} = 0.06$

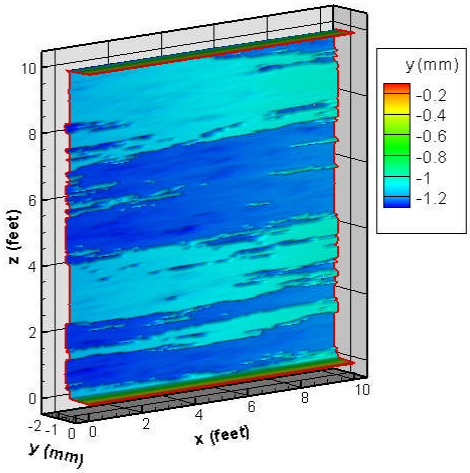


(a) $\lambda_{D,z} = 0.13$

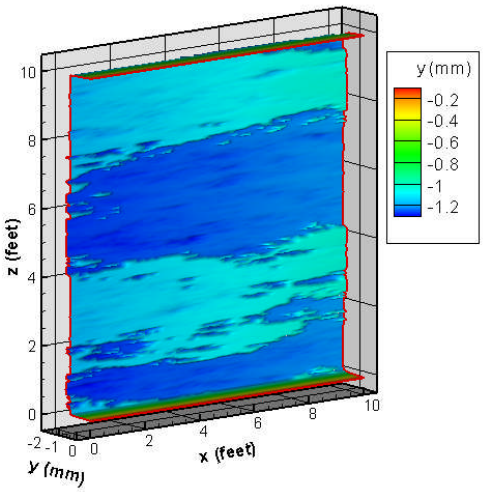


(b) $\lambda_{D,z} = 0.25$

**Fig. 5.20 – Continued.**

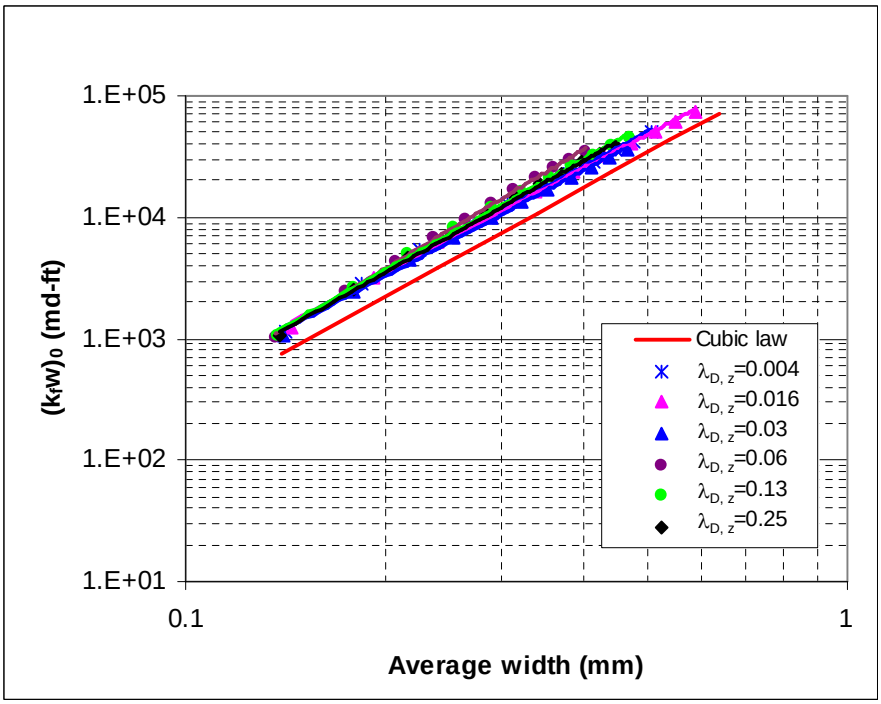


**Fig. 5.21 – Effects of the vertical correlation length of mineralogy distribution on conductivity.**

The percentage of limestone and dolomite affects the etching patterns because limestone has a faster reaction rate with the acid than dolomite. Fig. 5.22 shows the etching patterns for different percentage of limestone. The higher the percentage of limestone, the larger the average fracture width for a certain time of acid contact, and the higher the conductivity as shown in Fig. 5.23. When the percentage is low, narrow channels are obtained; when the percentage is very high, the fracture is more like a parallel plate with some asperities on the surfaces, and the conductivity line is very close to the cubic line. Fig. 5.24 shows conductivity increase with limestone percentage, which looks trivial. No simulation with limestone percentage lower than 20% is shown

on the plot because discontinuous channels give almost no conductivity when contacting the two fracture surfaces.

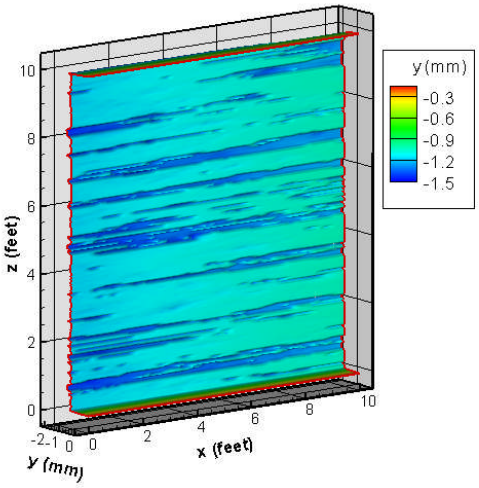


(a) 20% limestone

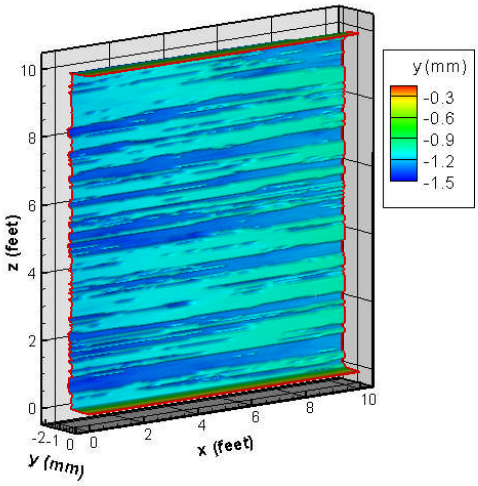


(b) 40% limestone

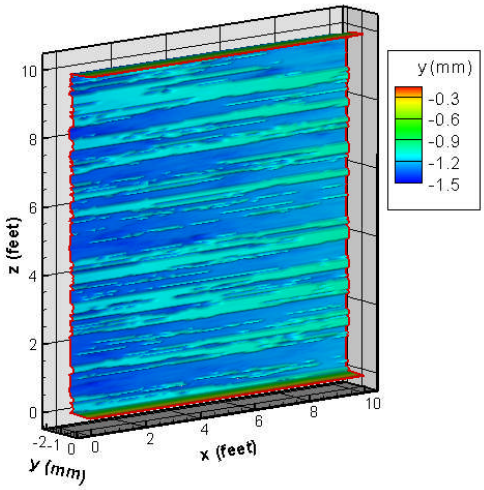


(a) 60% limestone

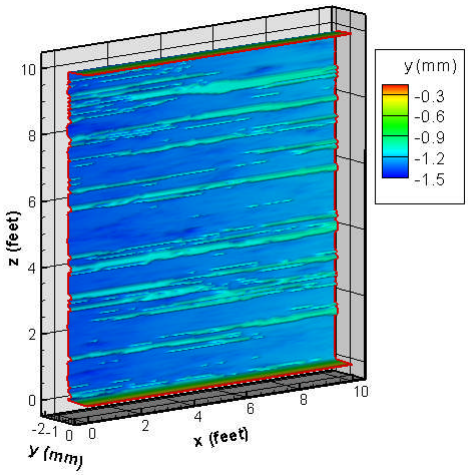


(b) 80% limestone

**Fig. 5.22 – Etching patterns for different percentages of limestone.**

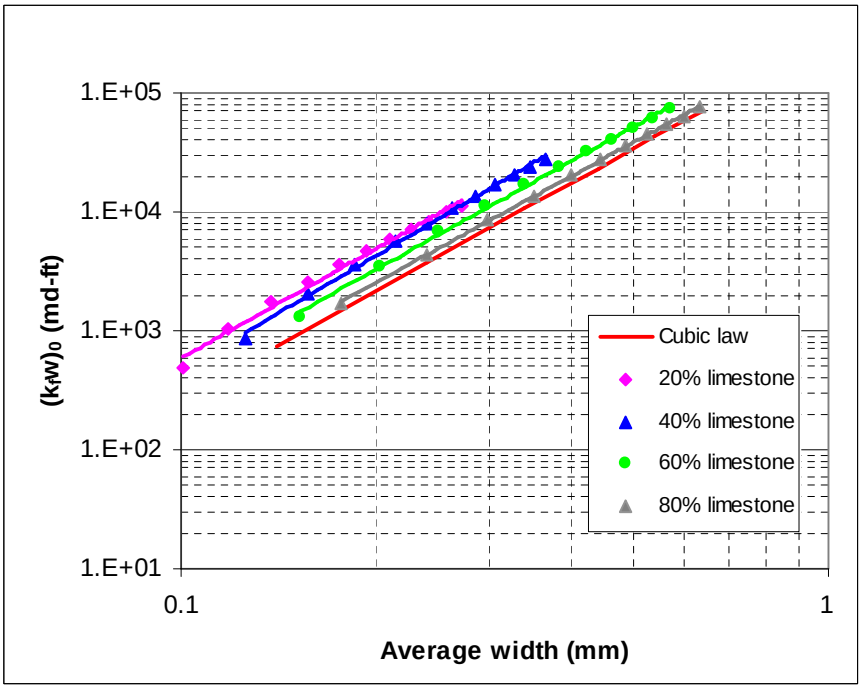


**Fig. 5.23 – Conductivity for different percentages of limestone.**

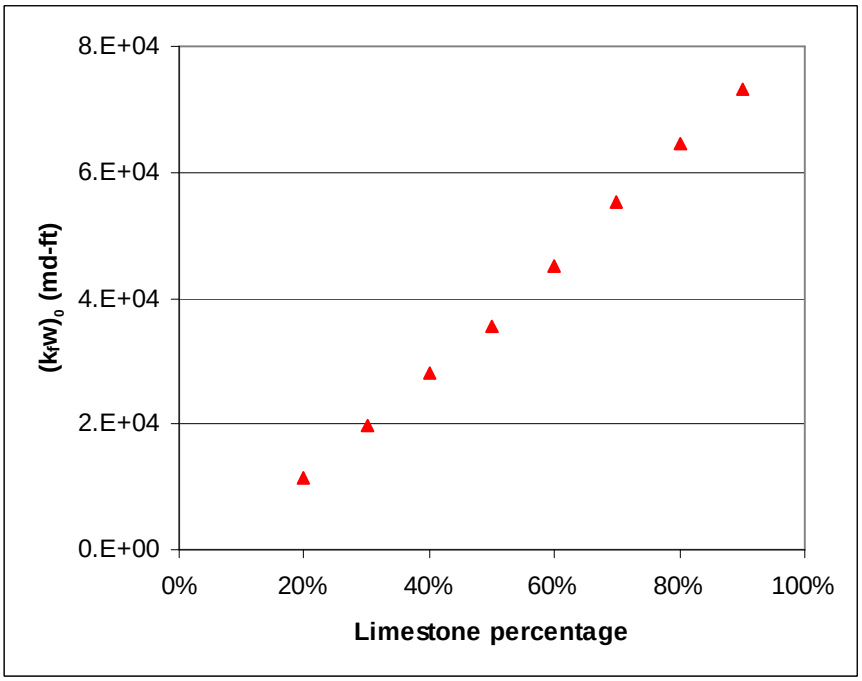


**Fig. 5.24 – Conductivity changes with limestone percentage.**

## 5.5 Competing Effect of Permeability and Mineralogy Distributions

In addition to the two extreme categories of permeability distribution dominance and mineralogy distribution dominance, there is one category between them. That is, both permeability and mineralogy distributions have competing effects on etching patterns and corresponding conductivities. The condition for this category is medium leakoff with leakoff coefficient of about 0.001 $ft/\sqrt{\text{min}}$ (for example, 1 md oil reservoirs under typical fracturing conditions).

First, we discuss the effect of mineralogy distribution on etching patterns and corresponding conductivities for this category. As shown in the previous section, the mineralogy distribution has a high horizontal correlation length, and the vertical correlation length does not affect conductivity, so we use a fixed high horizontal correlation length and a low vertical correlation length for the mineralogy distribution. By changing the percentage of limestone and dolomite, we can determine the effect of mineralogy distribution. Fig. 5.25 shows the etching patterns for different percentages of limestone. From the figure we can see the percentage of mineralogy has some effects on etching patterns but not large effect. Fig. 5.26 through 5.29 show that conductivity changes very little with mineralogy no matter what kind of permeability distribution, which means that there is no need to include any mineralogy distribution parameters in conductivity correlation development.

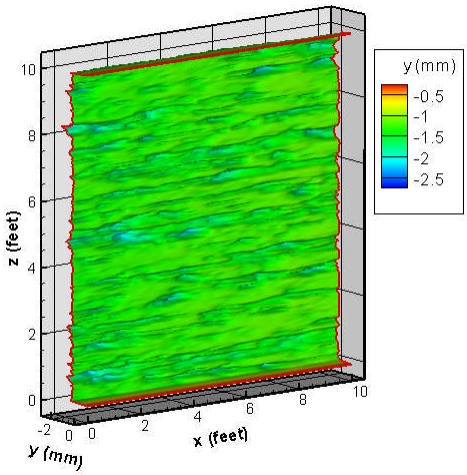


(a) 30% limestone

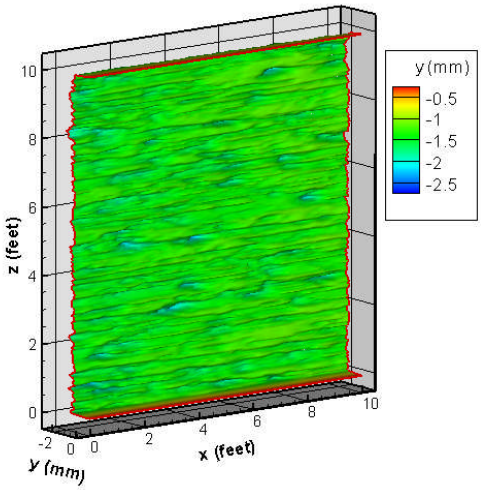


(b) 50% limestone

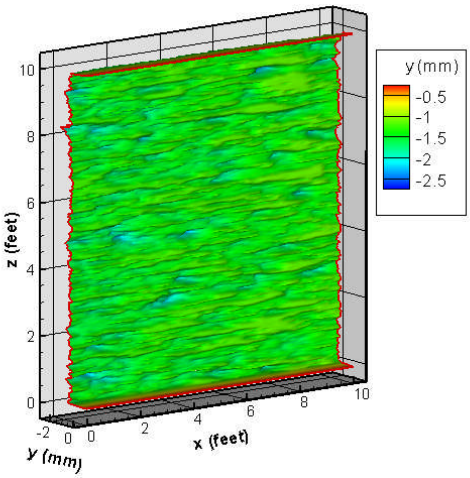


(a) 70% limestone

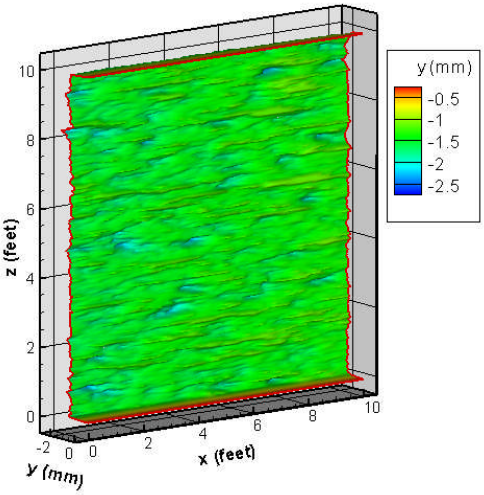


(b) 90% limestone

**Fig. 5.25 – Etching patterns with different limestone percentages (permeability distribution parameters: $\lambda_{D,x} = 0.06$, $\lambda_{D,z} = 0.03$, and $\sigma_D = 0.5$).**

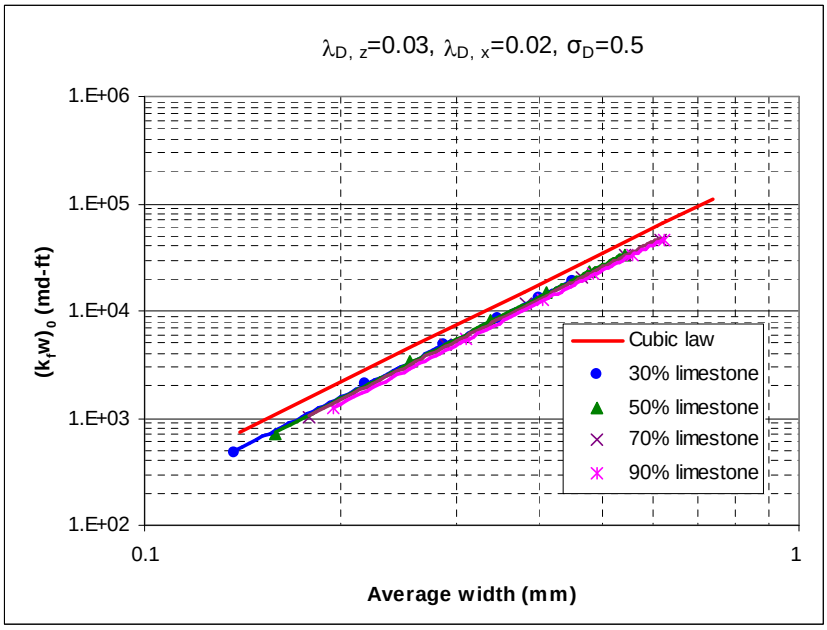


**Fig. 5.26 – Conductivities for different percentages of limestone (permeability distribution parameters: $\lambda_{D,x} = 0.02$, $\lambda_{D,z} = 0.03$, and $\sigma_D = 0.5$).**

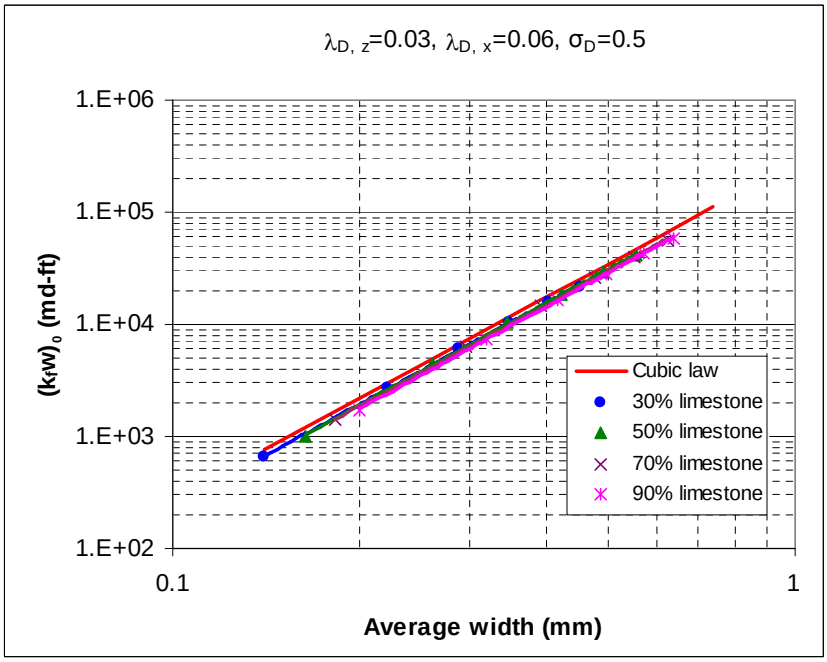


**Fig. 5.27 – Conductivities for different percentages of limestone (permeability distribution parameters: $\lambda_{D,x} = 0.06$, $\lambda_{D,z} = 0.03$, and $\sigma_D = 0.5$).**

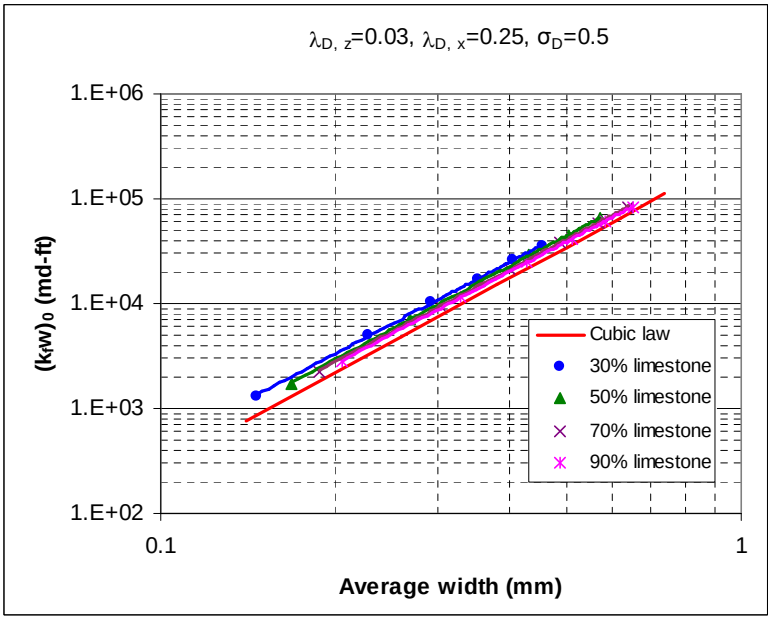


**Fig. 5.28 – Conductivities for different percentages of limestone (permeability distribution parameters: $\lambda_{D,x} = 0.25$, $\lambda_{D,z} = 0.03$, and $\sigma_D = 0.5$).**

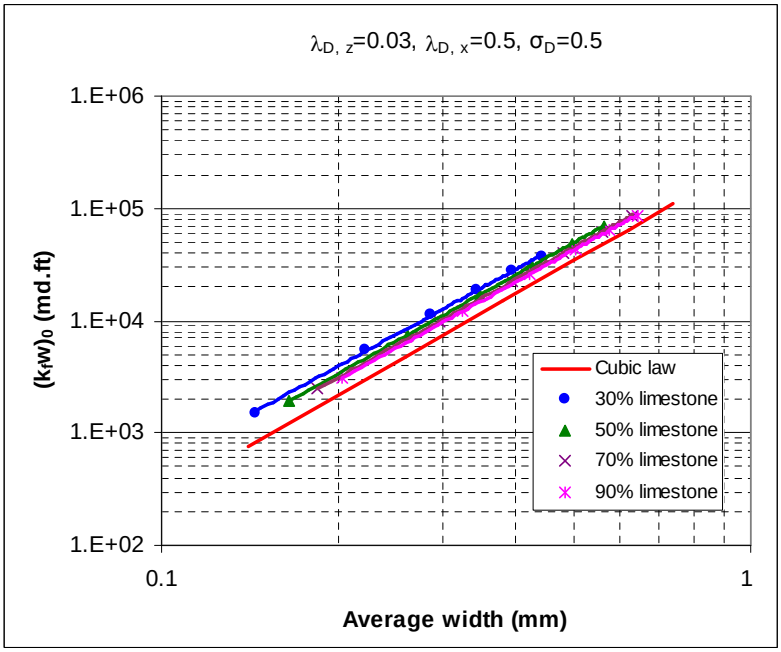


**Fig. 5.29 – Conductivities for different percentages of limestone (permeability distribution parameters: $\lambda_{D,x} = 0.5$, $\lambda_{D,z} = 0.03$, and $\sigma_D = 0.5$).**

Because the mineralogy distribution has a high horizontal correlation length due to layering characteristics of formations, whose contribution to conductivity is channeling, it is more likely to form channels in this category than the leakoff dominant category. When the horizontal correlation length of permeability distribution is small, isolated void spaces caused by leakoff are connected by channels caused by mineralogy distribution, but not continuous from the inlet to the outlet. Increasing the horizontal correlation length of permeability distribution causes more isolated void spaces to be connected to form longer channels until channels are continuous from the inlet to the outlet. Fig. 5.30 shows how etching patterns vary with the horizontal correlation length of permeability distribution. Corresponding conductivity is shown in Fig. 5.31. Increasing the horizontal correlation of permeability distributing make the conductivity lines move upward from below the base line to above the base line.

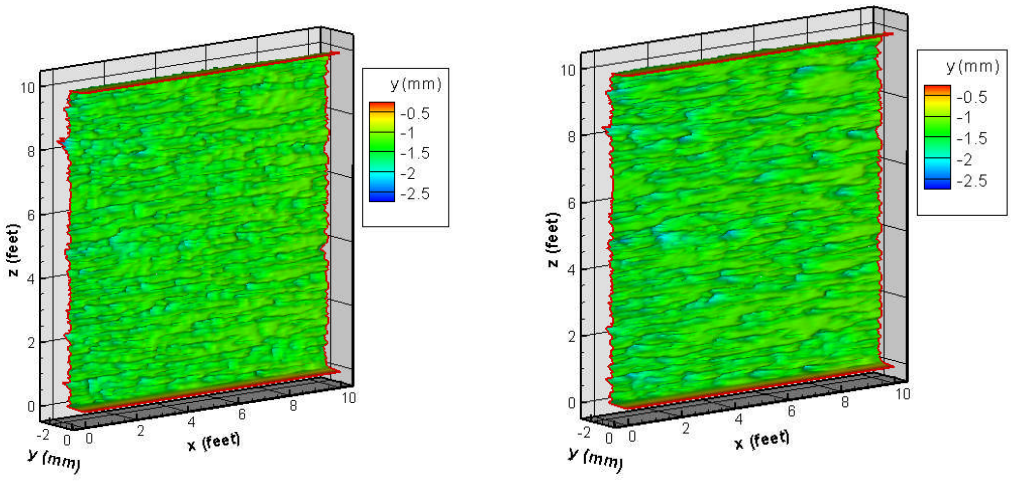


(a) $\lambda_{D,z} = 0.02$ (b) $\lambda_{D,z} = 0.06$

**Fig. 5.30 – Etching patterns for different horizontal permeability correlation lengths ($\lambda_{D,z} = 0.03$ and $\sigma_D = 0.5$ for permeability distribution).**

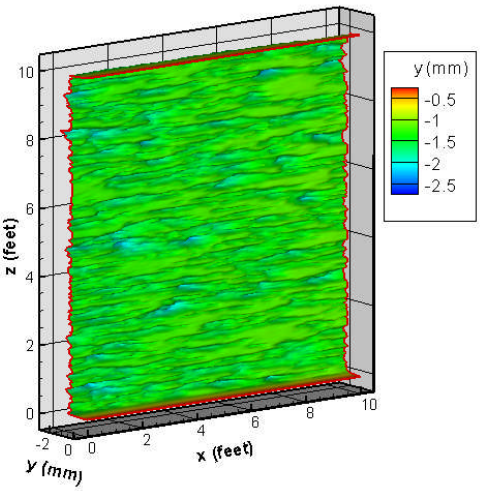


(a) $\lambda_{D,z} = 0.13$

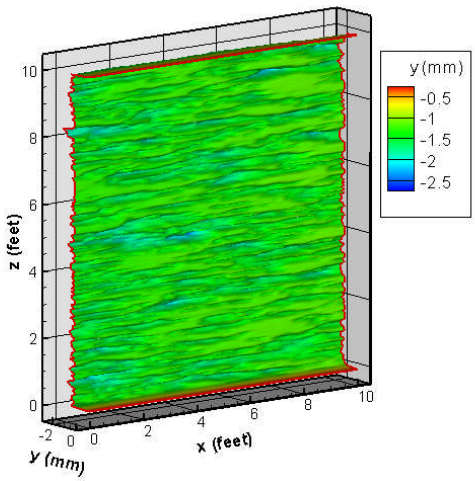


(b) $\lambda_{D,z} = 0.25$

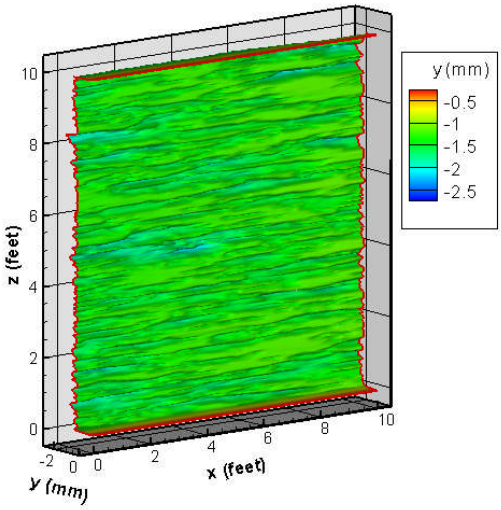


(a) $\lambda_{D,z} = 0.5$

**Fig. 5.30 – Continued.**

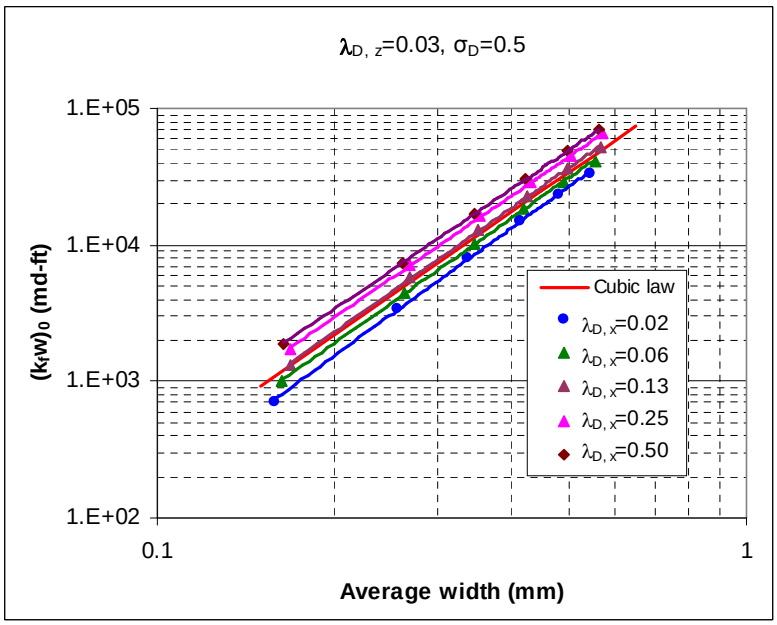


**Fig. 5.31 – Conductivities for different horizontal permeability correlation lengths ($\lambda_{D,z} = 0.03$ and $\sigma_D = 0.5$ for permeability distribution).**

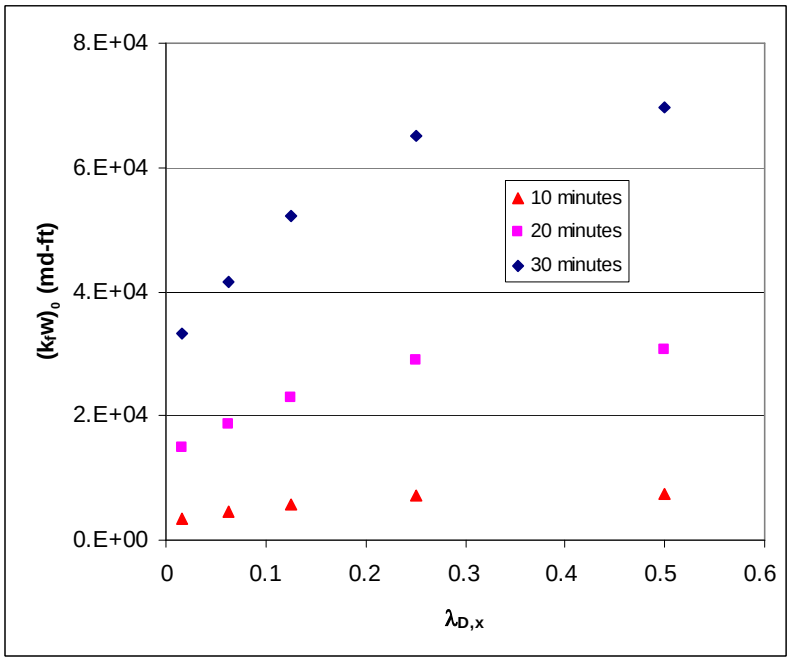


**Fig. 5.32 – Conductivities increase with the horizontal permeability correlation lengths ($\lambda_{D,z} = 0.03$ and $\sigma_D = 0.5$ for permeability distribution).**

Fig. 5.32 shows conductivity increases with increasing horizontal correlation length of the permeability distribution for three acid contact times. When $\lambda_{D,x}$ of the permeability distribution is small, conductivity increases rapidly with increasing $\lambda_{D,x}$. At about $\lambda_{D,x} = 0.5$, conductivity will level off. The trend is similar to the category of leakoff distribution dominant cases, but the increase magnitude is smaller than the category of leakoff distribution dominant cases when increasing $\lambda_{D,x}$ of permeability distribution from a small value to a high value.

Fig. 5.33 shows the etching patterns when increasing $\lambda_{D,z}$ of the permeability distribution. Because of high $\lambda_{D,x}$ for both permeability and mineralogy distributions, we got deep, narrow channels for low $\lambda_{D,z}$ of permeability distribution. Increasing $\lambda_{D,z}$ of the permeability distribution makes channels wider and wider until some large isolated void spaces form, but some channels still remain because of the contribution of mineralogy distribution. The corresponding conductivities are shown in Fig. 5.34 and Fig. 5.35. They show how conductivity decreases with increasing vertical correlation of permeability distribution. Increasing the vertical correlation of the permeability distribution does not decrease conductivity as drastically as in the category of permeability distribution dominant cases because of the channeling contribution of mineralogy distribution.

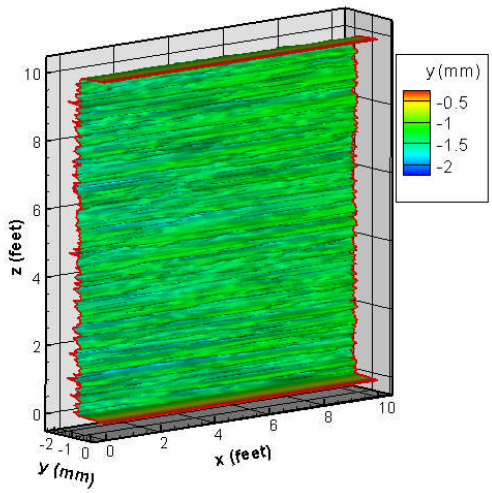


(a) $\lambda_{D,z} = 0.004$

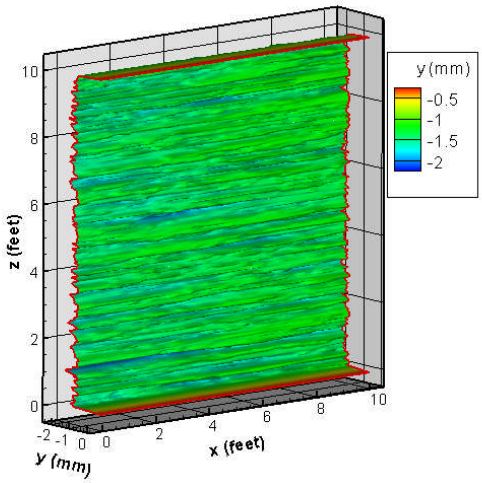


(b) $\lambda_{D,z} = 0.016$

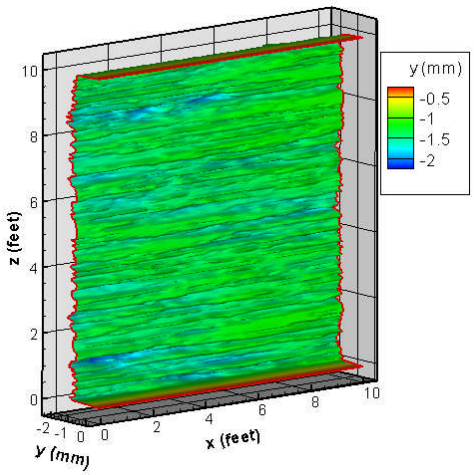


(c) $\lambda_{D,z} = 0.06$

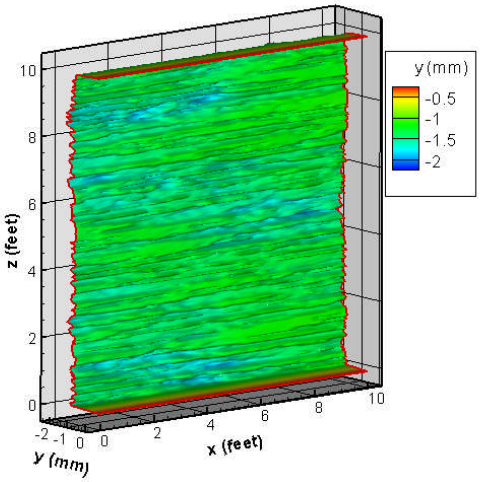


(d) $\lambda_{D,z} = 0.125$

**Fig. 5.33 – Etching patterns for different vertical correlation lengths of permeability distributions ( $\lambda_{D,x} = 0.5$ and $\sigma_D = 0.5$ for permeability distribution).**

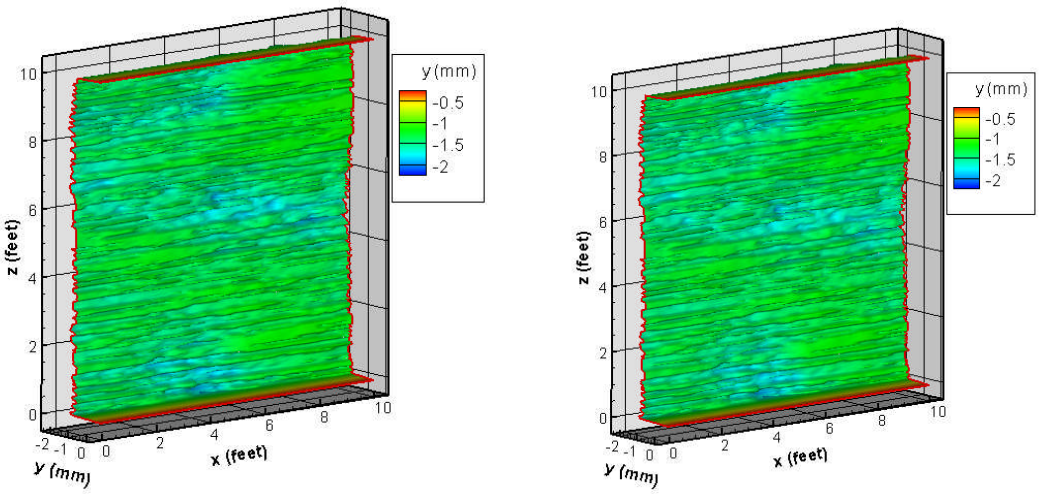


(e) $\lambda_{D,z} = 0.25$ (f) $\lambda_{D,z} = 0.375$

**Fig. 5.33 – Continued.**

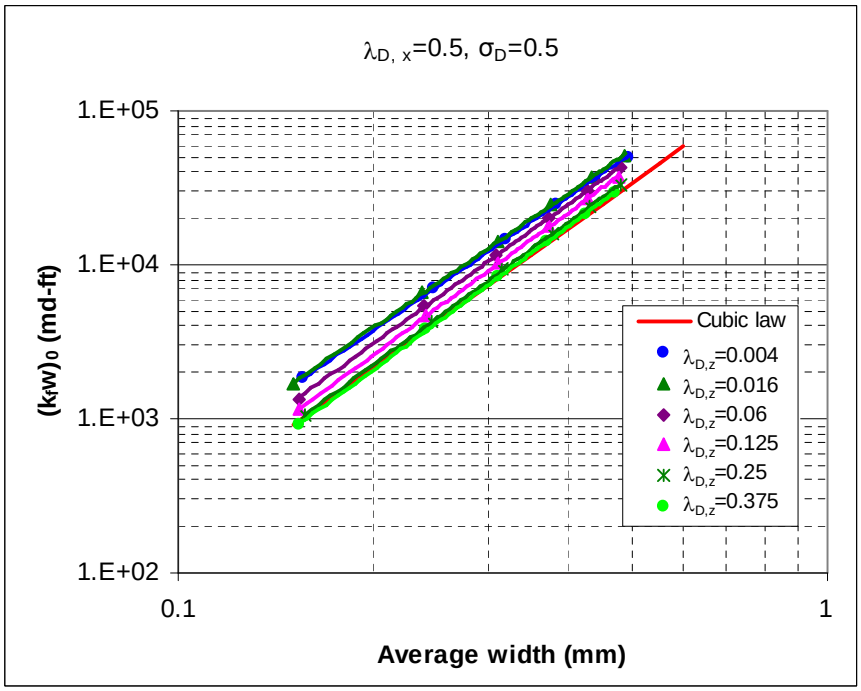


**Fig. 5.34 – Conductivities for different vertical correlation lengths of permeability distributions ($\lambda_{D,x} = 0.5$ and $\sigma_D = 0.5$ for permeability distribution).**

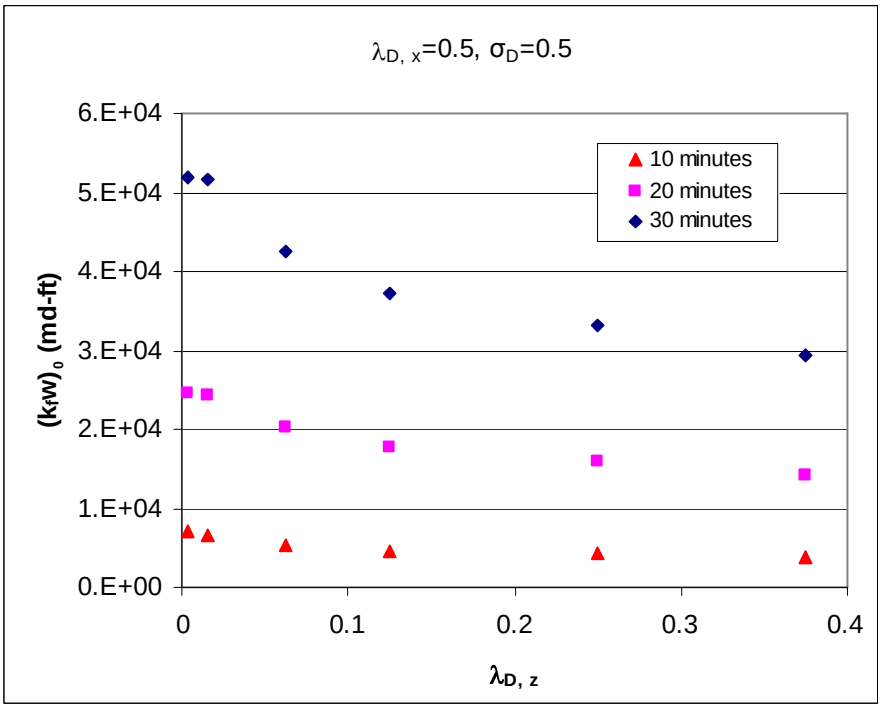


**Fig. 5.35 – Conductivities decrease with the vertical correlation length of permeability distributions ( $\lambda_{D,x} = 0.5$ and $\sigma_D = 0.5$ for permeability distribution).**

## 5.6 Influence of Acid Properties

### 5.6.1 Acid Concentration

The most commonly used HCl has a concentration of 15 weight%. Higher concentrations such as 20% or 28% are also used in practice. To investigate the effect of acid concentration on etching pattern, we simulate two cases, leakoff distribution dominance on etching patterns and mineralogy distribution dominance on etching patterns, with the same parameters except for one case with 15% HCl and the other one with 28% HCl. Fig. 5.36 shows 28% HCl causes deeper etching depth than 15% HCl at the same acid contact time, but etching patterns look similar for the two concentrations

for the leakoff distribution dominance case. Fig. 5.37 shows that the conductivity lines of 15% and 28% HCl almost lies on the same curve although at the same acid contact time 28% HCl gives larger fracture width than 15% HCl. A similar phenomenon is observed for mineralogy distribution dominance cases (Fig. 5.38 and Fig. 5.39). Therefore, acid concentration does not affect etching patterns.

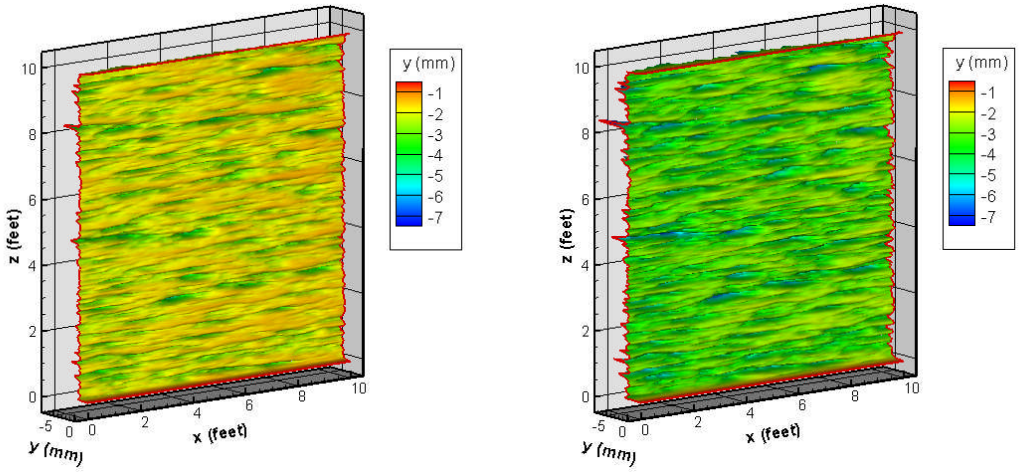


(a) 15% HCl (b) 28% HCl

**Fig. 5.36 – Etching patterns for different acid concentrations (permeability distribution dominance).**

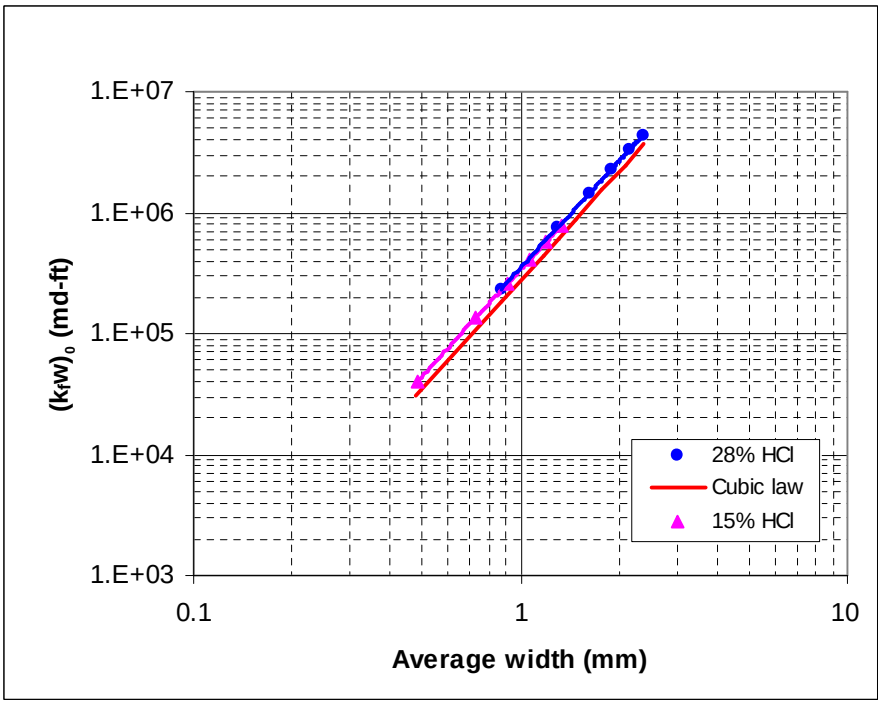


**Fig. 5.37 – Conductivities for different acid concentrations (permeability distribution dominance).**

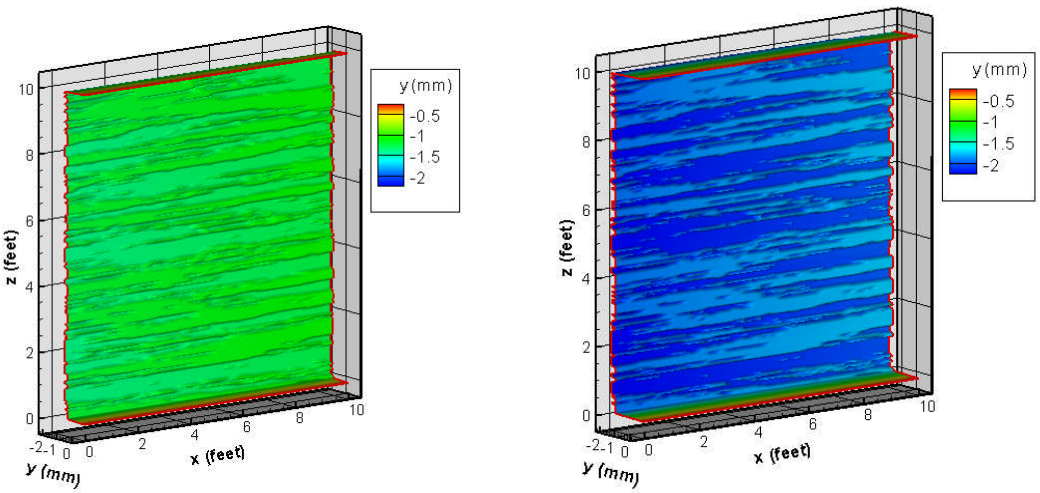


(a) 15% HCl (b) 28% HCl

**Fig. 5.38 – Etching patterns for different acid concentrations (mineralogy distribution dominance).**

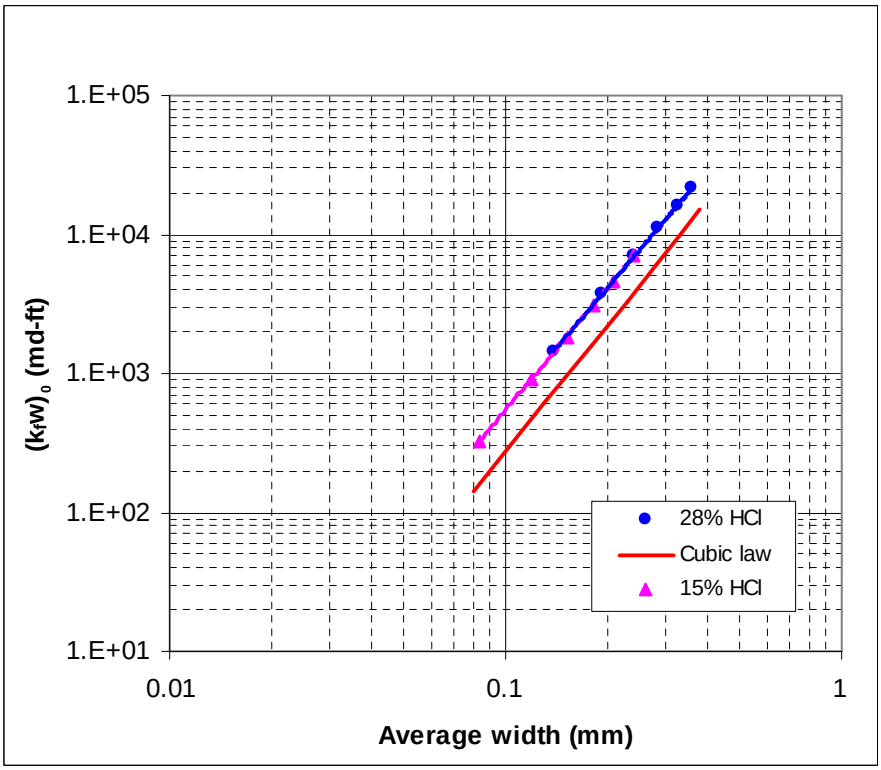


**Fig. 5.39 – Conductivities for different acid concentrations (mineralogy distribution dominance).**

### 5.6.2 Diffusion Coefficient

The acid is transported to the fracture surfaces by convection and diffusion. The former is contributed by acid leakoff, which is determined by the permeability distribution; and the latter is controlled by acid diffusion coefficient. To study the effect of diffusion coefficient on etching patterns and conductivity, we compared etching patterns and conductivity for gelled acid and straight acid. We used a diffusion coefficient of $6\times10^{-9} m^2/s$ and $10^{-8} m^2/s$ for gelled acid and straight acid respectively (De Rozieres et al., 1994; Navarrete et al., 1998; Conway et al, 1999). A temperature of

210 $^{o}$F is used for reaction rate calculation. For permeability distribution dominant cases, we used uniform limestone distribution on the fracture surfaces. The etching profiles shown in Fig. 5.40 indicate straight acid gives a little more etched depth than gelled acid for the same contact time. Fig. 5.41 shows almost the same conductivity for gelled acid and straight acid, which means that the acid diffusion coefficient has little effect on etching patterns for permeability distribution dominant cases. For mineralogy distribution dominant cases, straight acid causes much deeper etched depth than gelled acid for the same acid contact time, but the fracture surface shape looks similar as shown in Fig. 5.42. Corresponding conductivity lines shown in Fig. 5.43 lie almost on the same straight line for gelled acid and straight acid although average fracture width is different, which means the relationship between conductivity and average fracture width for gelled acid and straight acid is the same. Therefore, acid diffusion coefficient does not need to be included in developing acid fracture conductivity correlations. However, acid diffusion coefficient has an effect on live acid penetration distance. Higher acid diffusion coefficient causes faster transport of acid to the fracture surfaces, so less acid moves down the fracture as shown in Fig. 5.44.

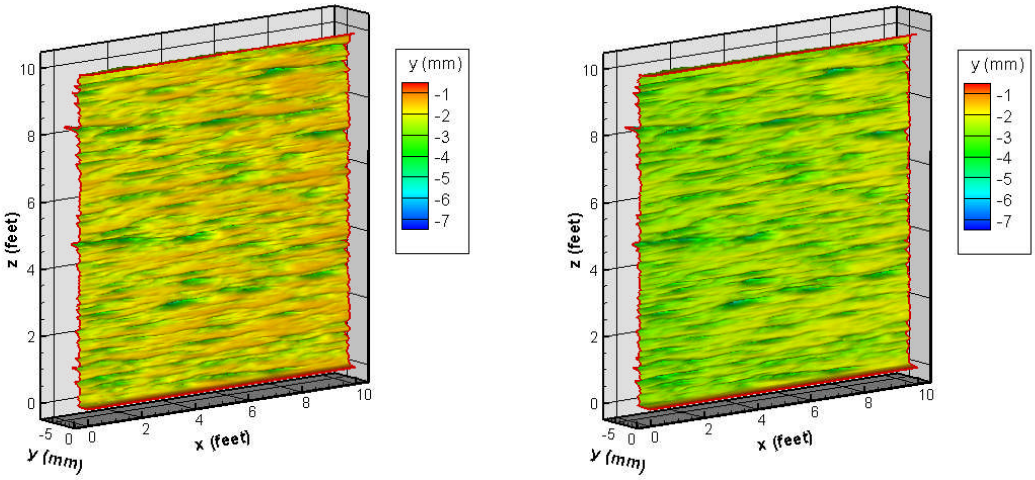


(a) Gelled acid (b) Straight acid

**Fig. 5.40 – Etching patterns for gelled and straight acids (permeability distribution dominance).**

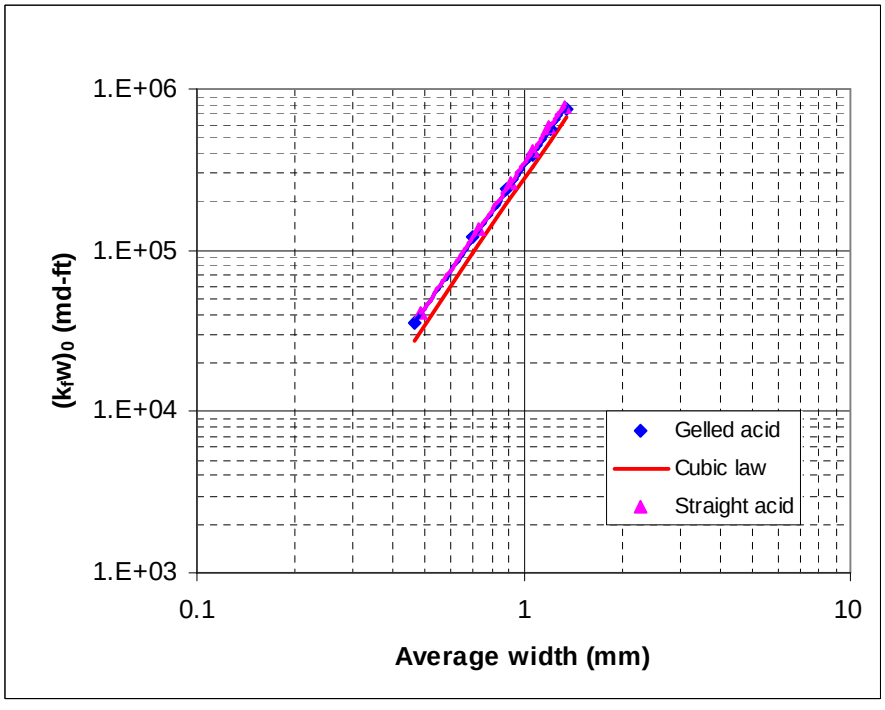


**Fig. 5.41 – Conductivities for gelled and straight acids (permeability distribution dominance).**

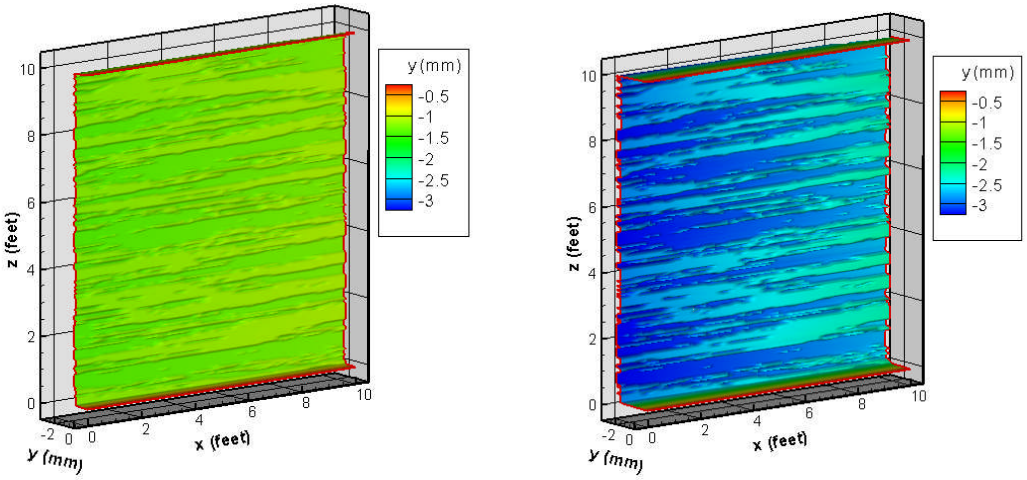


(a) Gelled acid (b) Straight acid

**Fig. 5.42 – Etching patterns for gelled and straight acids (mineralogy distribution dominance).**

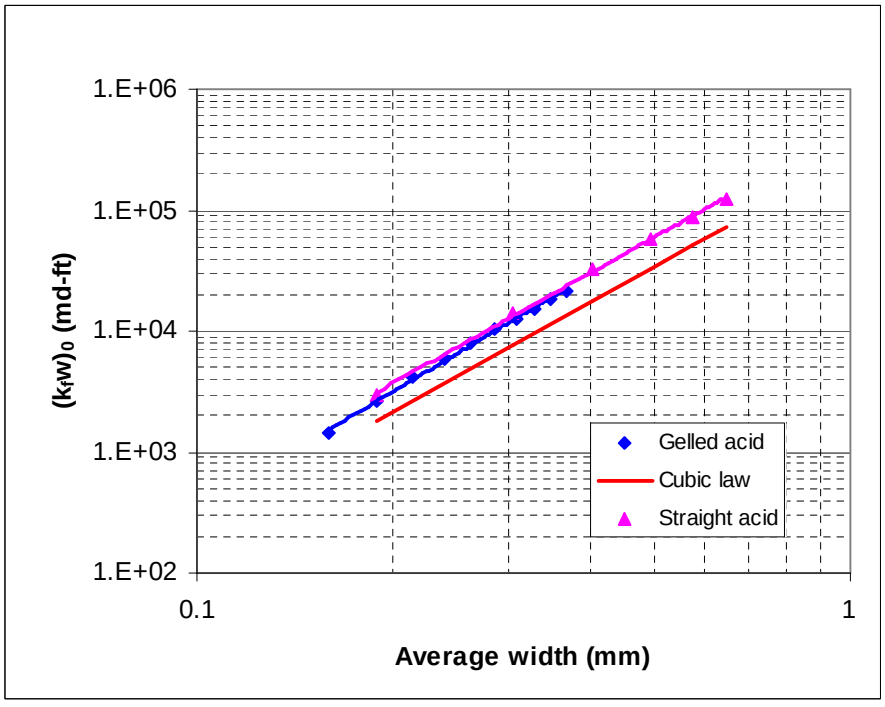


**Fig. 5.43 – Conductivities for gelled and straight acids (mineralogy distribution dominance).**

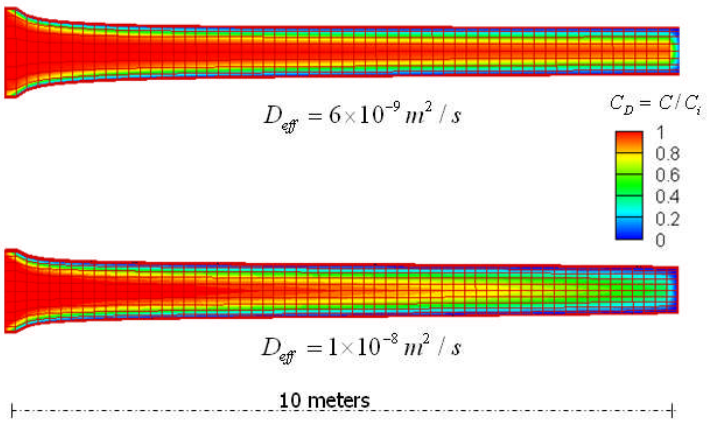


**Fig. 5.44 – Acid diffusion coefficient effect on live acid penetration distance.**

## 5.7 Conditions Leading to Deep, Narrow Channels

Fracture surface etching patterns affect not only conductivities at zero closure stress but also the deformation of the surfaces under closure stress and corresponding conductivities. Deep, narrow channels can remain open under closure stress so as to create high conductivities. Based on previous analysis, the factors determining etching patterns are statistical parameters of permeability and mineralogy distributions. General conditions leading to deep, narrow channels are high horizontal correlation strengths and low vertical correlation strengths of permeability and mineralogy distributions, high standard deviation of permeability distribution, and low temperature because low temperature can cause more etching depth difference by mineralogy.

Fig. 5.45 shows a case in which narrow channels are created. The statistical parameters used are $\lambda_{D,x} = 0.8$ , $\lambda_{D,z} = 0.04$ , and $\sigma_D = 0.5$ for permeability; $\lambda_{D,x} = 0.8$ , $\lambda_{D,z} = 0.04$ for mineralogy, 30 % limestone, and 70% dolomite. Permeability

has a high horizontal correlation length and a low vertical correlation length. $\sigma_D = 0.5$ gives permeability range of 0.1 ~ 500 md, indicating a strong heterogeneity. Mineralogy distribution has a high horizontal correlation length and a low vertical correlation length. Temperature is 150 $^{o}$F. With those parameters, we obtained the deep, narrow channels shown in Fig. 5.45.

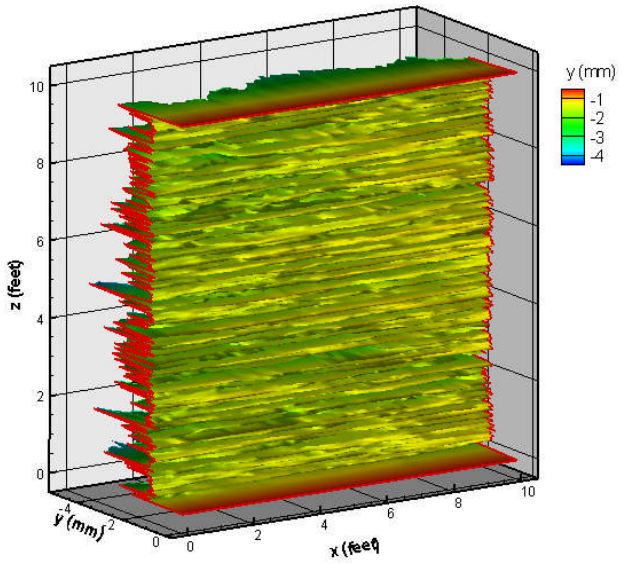


**Fig. 5.45 – An example of narrow, deep channels.**

## 5.8 Correlations of Conductivity at Zero Closure Stress

An acid fracture conductivity correlation generally has two parts, conductivity at zero closure stress and the conductivity decrease rate with increasing closure stress. In this research, I just studied the conductivity at zero closure stress. The fundamental principal of fracture conductivity at zero closure stress is the cubic law, which characterizes the flow in narrow slots with smooth surfaces. For fractures with rough

walls, the relationship between flux and pressure drop will deviate from the cubic law. Several researchers developed conductivity correlations at zero closure stress based on the cubic law by coupling surface characteristics.

1) Nierode and Kruk (1973)

Nierode and Kruk developed the acid fracture conductivity correlation at zero closure stress based on experiments. By comparing the weight difference of the dry core before and after experiments, they calculated idea fracture width, which is the dissolved rock volume divided by the fracture area. They measured corresponding conductivities at zero closure stress. By correlating the calculated idea fracture width to measured conductivity at zero closure stress, they got the following correlation.

$$\left(k_f w\right)_0 = 1.47 \times 10^7 \, w_i^{2.47} \quad \text{..... (5. 3)}$$

where $w_i$ is the idea fracture width.

2) Patir and Cheng (1978)

Patir and Cheng developed a correlation semi-theoretically.

$$\left(k_f w\right)_0 = \frac{\overline{w}^3}{12}\left(1 - C_1 \exp\left(-C_2\left(\overline{w}/\sigma_w\right)\right)\right) \quad \text{..... (5. 4)}$$

where $C_1$ and $C_2$ are empirical constants of 0.9 and 0.6 respectively obtained by numerical experiments and data regression.

3) Walsh (1981)

Walsh developed the following correlation theoretically.

$$\left(k_f w\right)_0 = \frac{\overline{w}^3}{12}\left(\frac{1-\alpha}{1+\alpha}\right) \quad \text{..... (5. 5)}$$

where $\alpha$ is the ratio of the contact area to the total area of the fracture.

The correlations do not consider the effect of fracture surface etching patterns (the spatial distribution of roughness) on fracture conductivity. They are for random roughness distributions. Spatially correlated roughness distributions can form channels in the flow direction, which contribute greatly to conductivity because of negligible pressure drop for fluid flow in channels. Therefore, we developed new correlations incorporating the effect of spatial distribution of formation properties, which determine fracture surface etching patterns, on conductivity using our simulator.

With the intermediate-scale model we can do extensive numerical experiments by changing permeability and mineralogy distributions, and then use the data to develop conductivity correlations including parameters describing spatial distributions of permeability and mineralogy. As discussed in previous sections, etching patterns can be classified into three categories according to relative effect of permeability and mineralogy distribution on etching patterns: permeability distribution dominance, mineralogy distribution dominance, and competing effects of permeability and mineralogy distributions. When developing conductivity correlations, we follow the three categories because different parameters are used in different categories.

### 5.8.1 Permeability Distribution Dominance

This is the case with high leakoff or medium leakoff with 0% or 100% limestone, in which the permeability distribution determines fracture surface etching patterns. As discussed previously, mineralogy distributions do not affect conductivity as shown in Fig. 5.4 and Fig. 5.6, so in the conductivity correlation, the parameters associated with

mineralogy distribution will not appear. The parameters used in the correlation include average fracture width, the dimensionless horizontal and vertical correlation length of permeability, and the dimensionless standard deviation of the natural log of the permeability distribution. The dimensionless parameters are defined previously. By fitting the simulation data output from the intermediate-scale model, we get the following correlation for the cases where leakoff dominates fracture surface etching patterns. The average fracture width, $\overline{w}$, is the fracture volume divided by the fracture surface area. How to get $\overline{w}$ is discussed in the later section.

$$\left(k_f w\right)_0 = \frac{\overline{w}^3}{12}\left[1+\left(a_1 erf\left(a_2(\lambda_{D,x}-a_3)\right)-a_4 erf\left(a_5(\lambda_{D,z}-a_6)\right)\right)\sqrt{(e^{\sigma_D}-1)}\right] \quad \textbf{(5. 6)}$$

where

$a_1 = 1.63$ $\quad a_2 = 5.0$ $\quad a_3 = 0.15$

$a_4 = 1.39$ $\quad a_5 = 11.0$ $\quad a_6 = 0.03$

Fig. 5.46 shows a comparison of fracture conductivity between numerical calculation and correlation calculation.

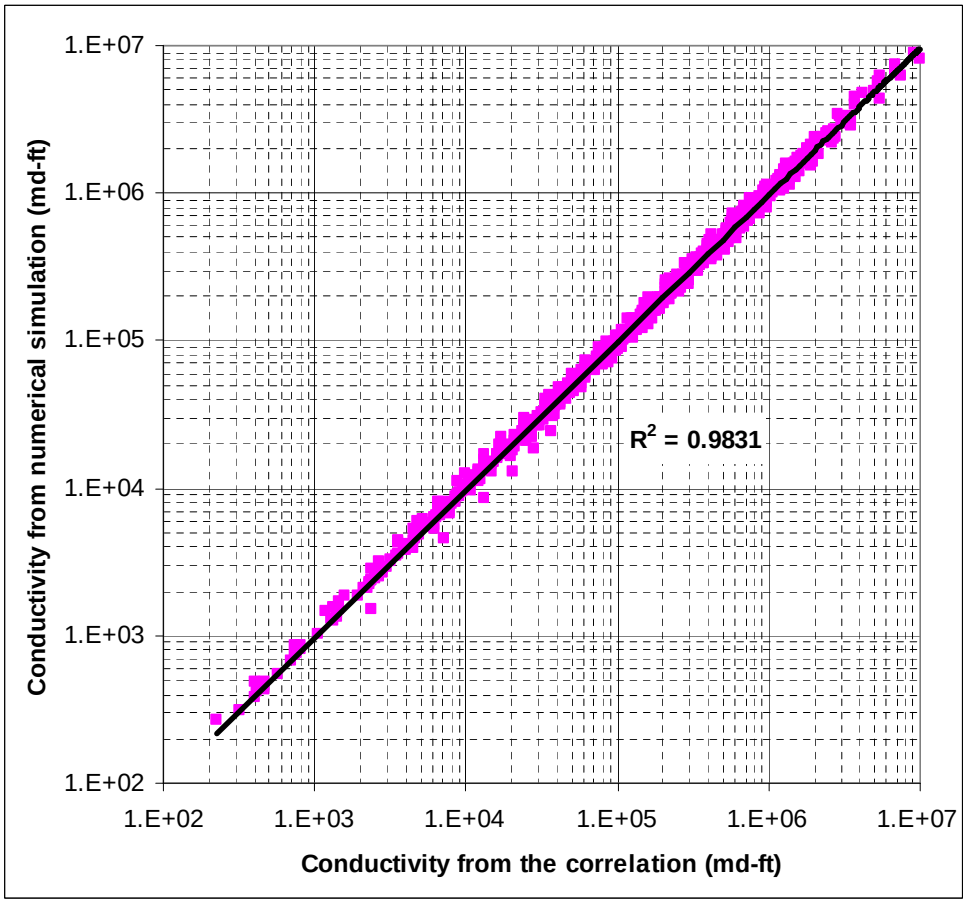


**Fig. 5.46 – Comparison of fracture conductivity between numerical calculation and correlation calculation (permeability distribution dominance).**

### 5.8.2 Mineralogy Distribution Dominance

In cases of very low permeability reservoirs, leakoff is so small that its effects on surface etching patterns is negligible compared to mineralogy distribution effects, which is called mineralogy distribution dominance. In this situation, the conductivity correlation includes parameters describing the mineralogy distribution and average fracture width. As discussed previously, we use high horizontal correlation length for mineralogy distribution to represent the characteristics of layered formations. The

vertical correlation length of mineralogy distribution affects the etching patterns as shown in Fig. 5.20, but Fig. 5.21 shows that conductivity changes little as the vertical correlation length of mineralogy distribution changes, which means the conductivity correlation does not need to include the vertical correlation length of mineralogy distribution. Therefore, the only parameter about the mineralogy distribution included in the correlation is the mineralogy percentage. Only the limestone and dolomite are considered in this study. The percentages of limestone and dolomite add up to 1, so only limestone percentage is used in the correlation.

By fitting the simulation data output from the intermediate-scale model, we get the correlation for mineralogy distribution dominant cases.

$$\left(k_f w\right)_0 = \frac{\overline{w}^3}{12}\left[1 + a_1\left(1 - f_{\text{limestone}}\right)^{a_2}\right] \quad \textbf{(5. 7)}$$

where

$a_1 = 2.97$ $\qquad$ $a_2 = 2.02$

$f_{\text{limestone}}$ : limestone percentage

Fig. 5.47 shows the comparison of fracture conductivity between numerical calculation and correlation calculation.

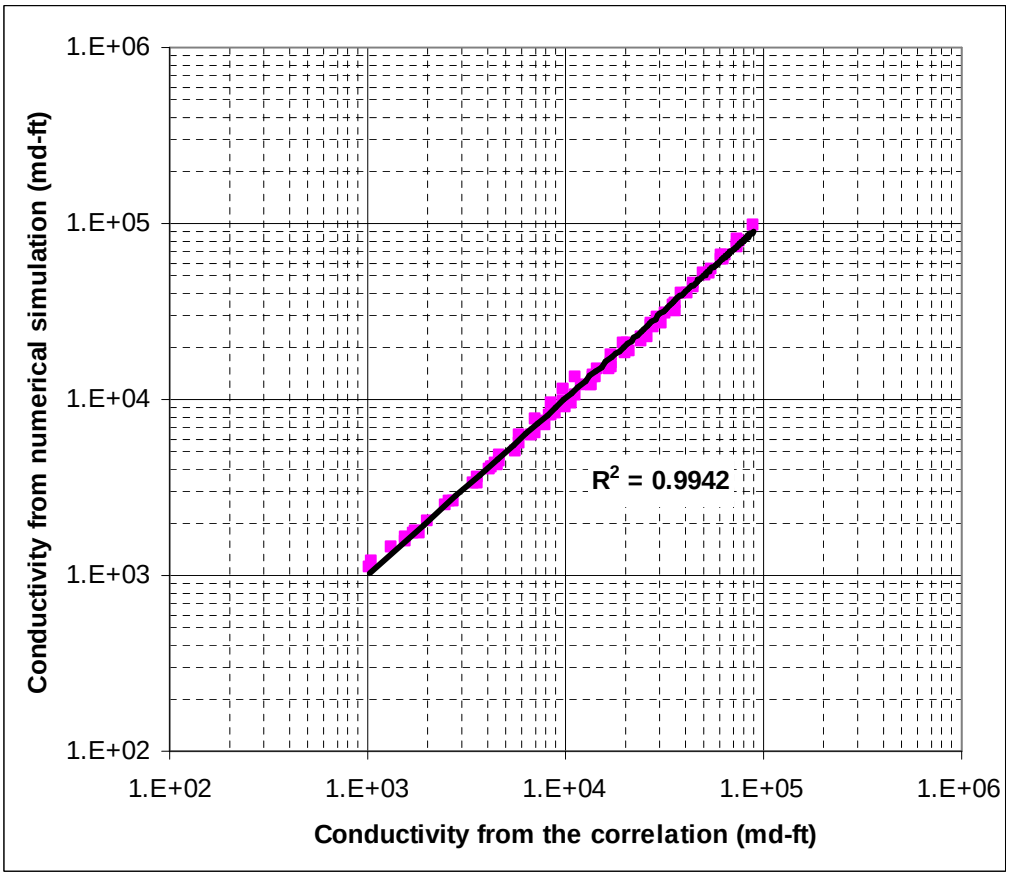


**Fig. 5.47 – Comparison of fracture conductivity between numerical calculation and correlation calculation (mineralogy distribution dominance).**

There are two extreme cases for this category: 0% or 100% limestone, in which the mineralogy distribution will give flat surface etching patterns because permeability distribution affect is negligible. Therefore, for these two extreme cases, we do not need to calculate conductivity because the conductivity is zero, or more precisely, very low.

### 5.8.3 Competing Effects of Permeability and Mineralogy Distributions

For medium leakoff cases, both permeability and mineralogy distributions determine fracture surface etching patterns. Fig. 5.26 through Fig. 5.29 show different

percentages of mineralogy give almost the same conductivity for different kinds of permeability distributions, which means we do not need to include the parameters of mineralogy distribution explicitly, but the mineralogy distribution does affect conductivity. Because of high horizontal correlation of the mineralogy distribution, the contribution of mineralogy distribution to conductivity is always channeling, which can connect isolated void spaces caused by leakoff. For the same permeability distribution, coupling the mineralogy effect will give higher conductivity than the case without mineralogy effect. Of course, there is an implicit assumption that rock is not purely composed of one kind of mineralogy, that is, 100% limestone or dolomite. By fitting the simulation data, we get the following conductivity correlation, the format of which is the same as that for leakoff distribution dominance except 0.2 in the bracket, which is related to the effect mineralogy distribution.

$$\left(wk_f\right)_0 = \frac{\overline{w}^3}{12}\left[1 + a_1 + \left(a_2 erf\left(a_3(\lambda_{D,x} - a_4)\right) - a_5 erf\left(a_6(\lambda_{D,z} - a_7)\right)\right)\sqrt{(e^{\sigma_D} - 1)}\right] \text{.....} \quad \textbf{(5. 8)}$$

where

$a_1 = 0.2$ $\quad a_2 = 0.95$ $\quad a_3 = 5.0$ $\quad a_4 = 0.15$

$a_5 = 0.6$ $\quad a_6 = 12.2$ $\quad a_7 = 0.03$

Fig. 5.48 shows the comparison of fracture conductivity between numerical calculation and correlation calculation.

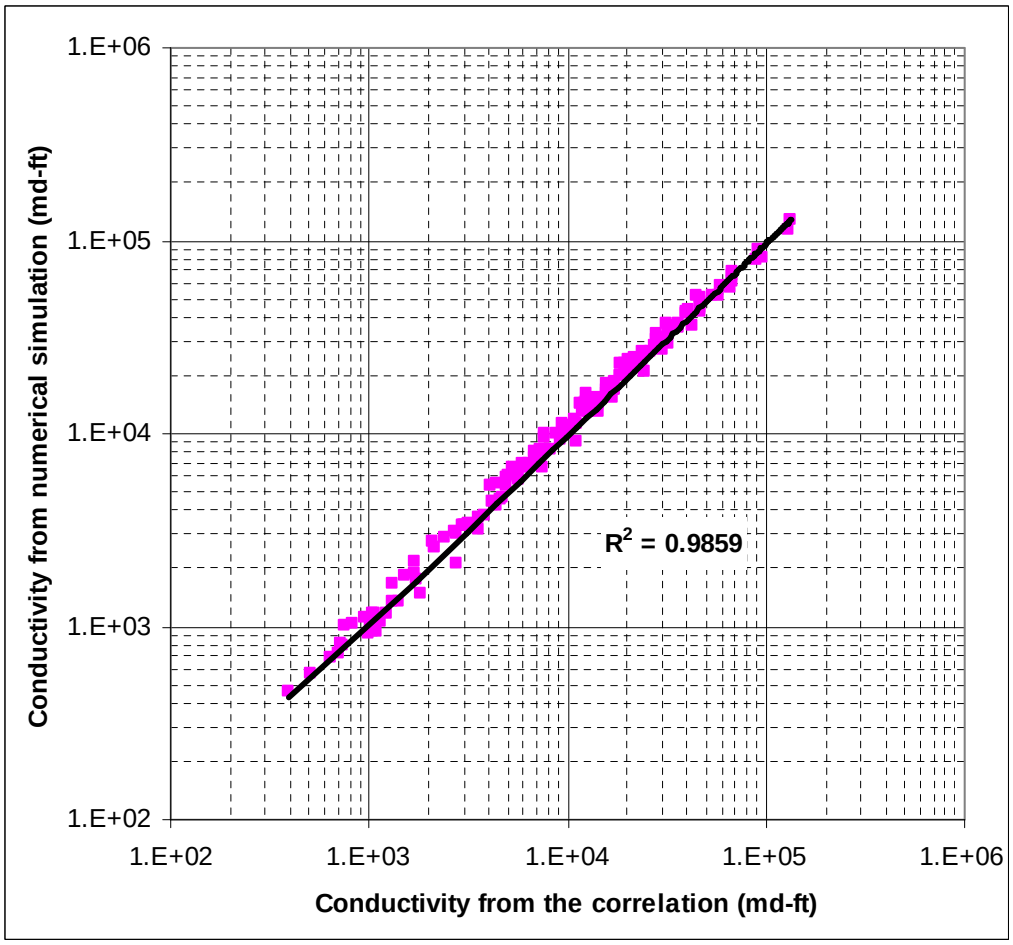


**Fig. 5.48 – Comparison of fracture conductivity between numerical calculation and correlation calculation (competing effect of permeability and mineralogy distributions).**

## 5.9 Correlations of Average Fracture Width

To use the correlations developed above, we need to know the average fracture width with the two fracture surfaces contacted at zero closure stress, which is called average fracture width, $\overline{w}$, hereafter. Without the detailed fracture surface etching profiles, we cannot calculate the average fracture width directly. The objective of the development of acid fracture correlations is to calculate conductivity without the detailed

fracture surface profiles. Therefore, we need to develop average fracture width correlations as a function of other parameters, which are easily obtained. An acid fracturing simulator can conveniently calculate the volume of rock dissolved in grid blocks, which can be converted into dissolved rock equivalent width $w_{dre}$ by the formula defined as $w_{dre} = \frac{\text{dissolved rock volume}}{\text{area}}$. The intermediate-scale model can calculate the total volume of dissolved rock for the whole domain, and hence the $w_{dre}$. By extensive simulations, we can find the relationship between $w_{dre}$ and $\overline{w}$. Apparently, $w_{dre}$ is larger than $\overline{w}$. The relationship between them depends on the surface etching profiles. For the same $w_{dre}$, the rougher the surface, the larger the $\overline{w}$, and vice versa. In the Nierode-Kruk correlation, dissolved rock equivalent conductivity is used to calculated conductivity at zero closure stress. In fact, dissolved rock equivalent conductivity is correlated to the dissolved rock equivalent width by the cubic law. Nierode and Kruk use a single correlation for all kinds of rock they used in the experiment. Corresponding to the development of conductivity correlations, the three categories are used for the correlations of average fracture width.

### 5.9.1 Permeability Distribution Dominance

For this category, the permeability distribution determines fracture surface etching patterns. The heterogeneity, indicated by $\sigma_D$ of permeability, determines the relationship of $w_{dre}$ and average fracture width. For this category, there are three cases: high leakoff and medium leakoff with 100% limestone or dolomite.

- High leakoff cases

Fig. 5.49 shows how $\sigma_D$ affects the relationship of $w_{dre}$ and average fracture width. By fitting the simulation data, we get the following correlation. $a_1$ has a unit of $(l)^{1-a_3}$, so the values of coefficients of $a_1$, $a_2$, and $a_3$ depend on the unit of $w_{dre}$. Millimeter is used in the correlation.

$$\overline{w} = a_1 erf(a_2 \sigma_D) w_{dre}^{a_3} \quad \text{..... (5. 9)}$$

where

$a_1 = 0.99$ $a_2 = 0.80$ $a_3 = 0.80$

$w_{dre}$ : dissolved equivalent rock width

Fig. 5.50 shows the comparison of average fracture between numerical calculation and correlation calculation.

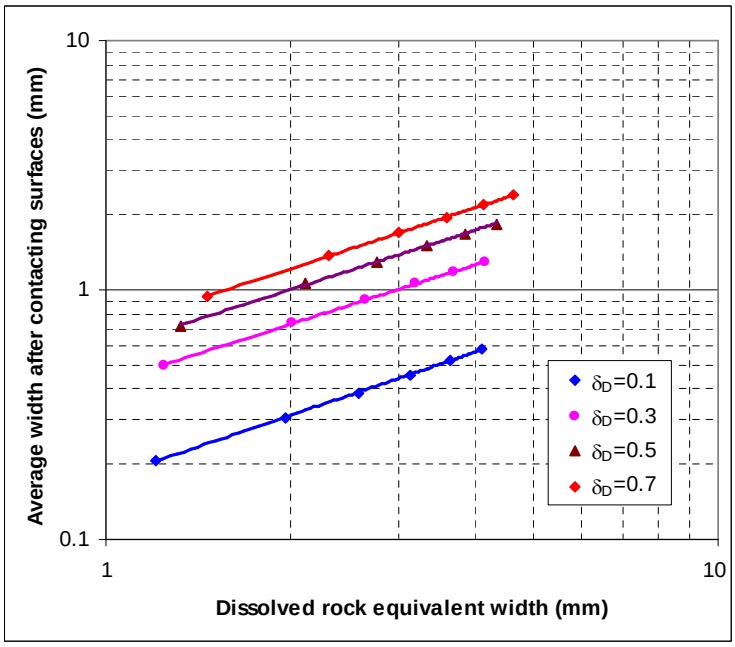


**Fig. 5.49 – Effect of $\sigma_D$ on average fracture width (high leakoff cases).**

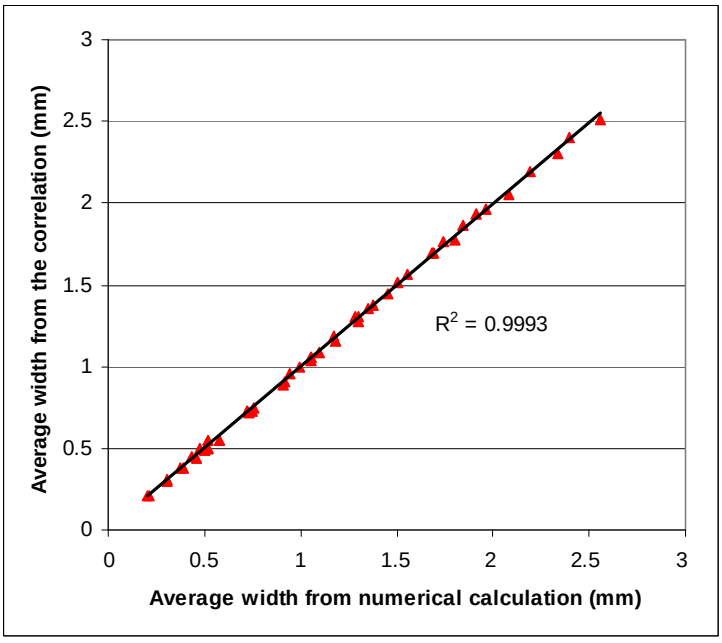


**Fig. 5.50 – Comparison of average fracture width between numerical calculation and correlation calculation (high leakoff cases).**

- Medium leakoff with 0% limestone

Fig. 5.51 shows how $\sigma_D$ affects average fracture width. Data fitting gives the following correlation. The unit of $w_{dre}$ is millimeter, and the unit of $a_1$ is $(\text{millimeter})^{1-a_3}$.

$$\overline{w} = a_1 erf(a_2 \sigma_D) w_{dre}^{a_3} \quad \text{..... (5. 10)}$$

where

$a_1 = 0.43$ $a_2 = 0.69$ $a_3 = 0.71$

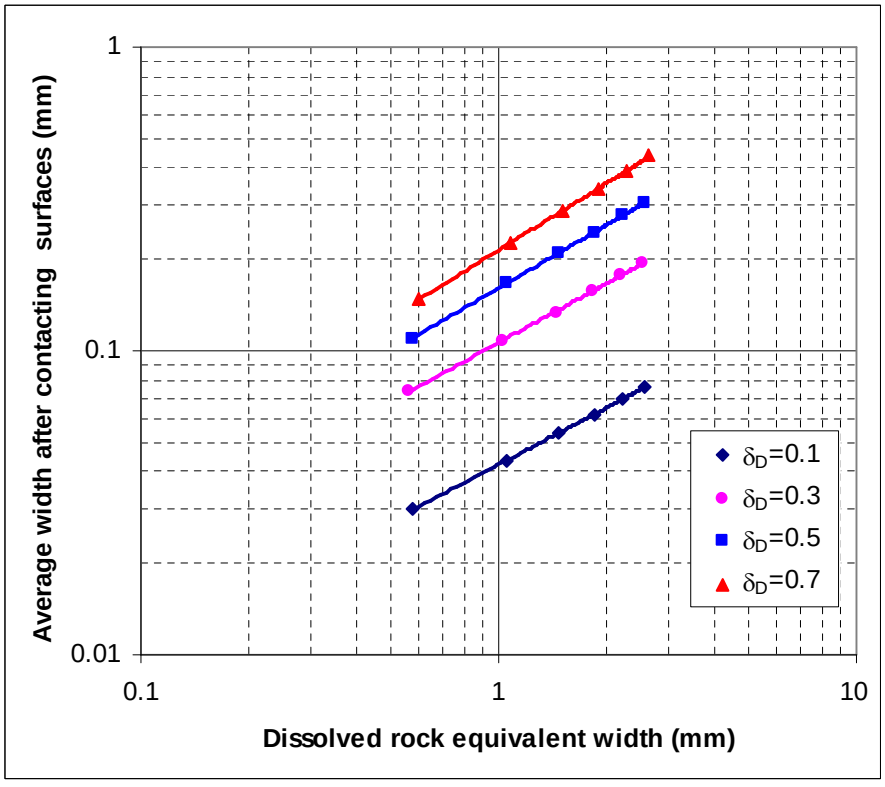


**Fig. 5.51 – Effect of $\sigma_D$ on average fracture width (medium leakoff and 0% limestone).**

Fig. 5.52 shows the comparison of average fracture width between numerical calculation and correlation calculation.

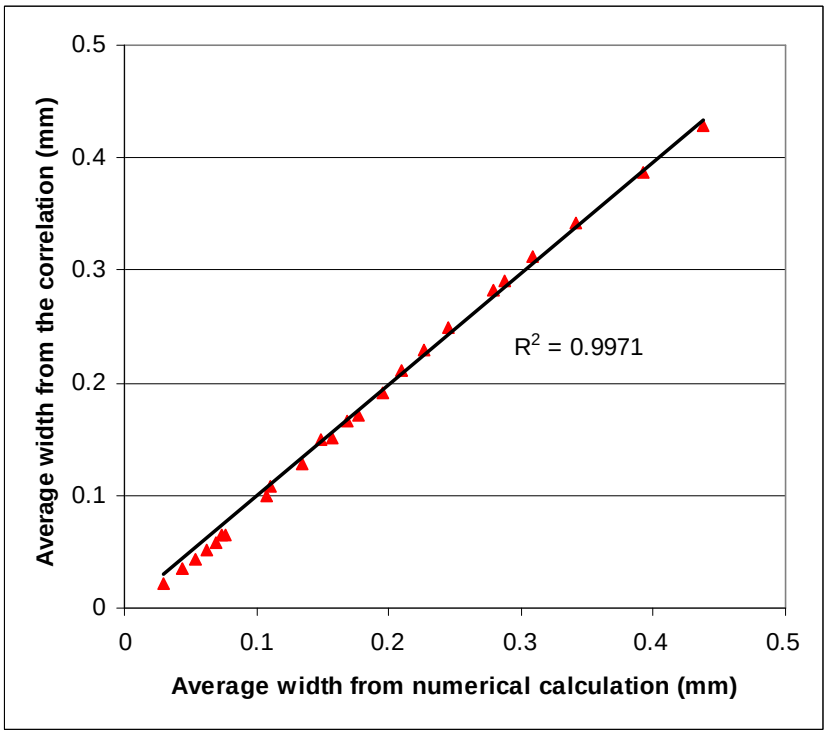


**Fig. 5.52 – Comparison of average fracture width between numerical calculation and correlation calculation (medium leakoff and 0% limestone).**

- 100% limestone

Fig. 5.53 shows how $\sigma_D$ affects average fracture width. Data fitting gives the following correlation. The unit of $w_{dre}$ is millimeter, and the unit of $a_1$ is $(\text{millimeter})^{1-a_3}$.

$$\overline{w} = a_1 erf(a_2 \sigma_D) w_{dre}^{a_3} \quad \text{..... (5. 11)}$$

where

$a_1 = 0.36$ $a_2 = 0.88$ $a_3 = 0.71$

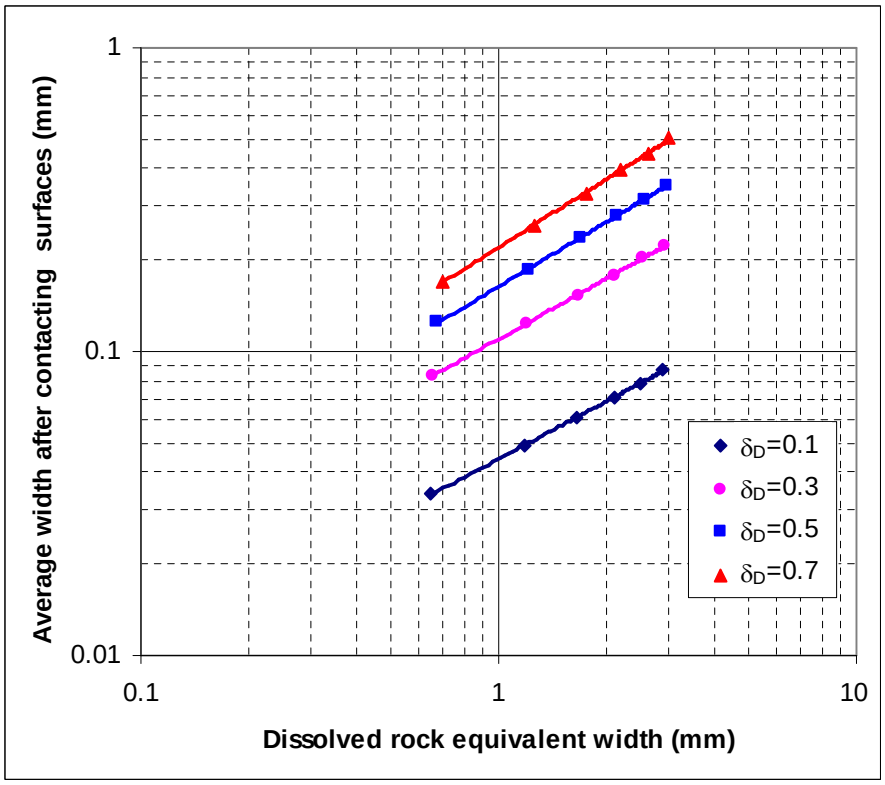


**Fig. 5.53 – Effect of $\sigma_D$ on average fracture width (medium leakoff and 100% limestone).**

Fig. 5.54 shows the comparison of average fracture width between numerical calculation and correlation calculation.

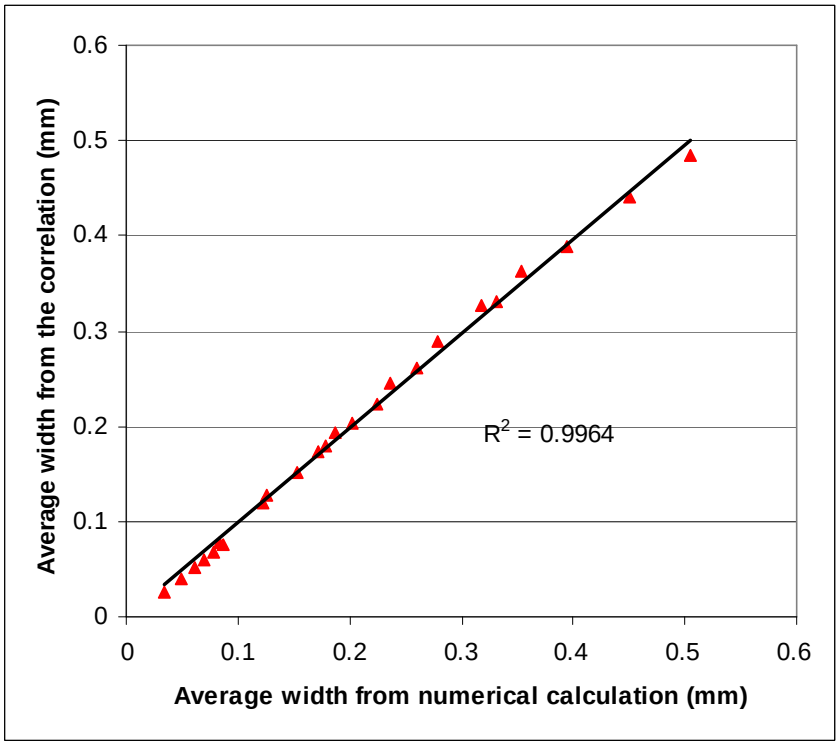


**Fig. 5.54 – Comparison of average fracture width between numerical calculation and correlation calculation (medium leakoff and 100% limestone).**

### 5.9.2 Mineralogy Distribution Dominance

For this category, only the mineralogy distribution affects the relationship between $w_{dre}$ and average fracture width. The mineralogy effect can be divided into two aspects. One is the effect of limestone or dolomite percentage. Another is the effect of etching depth difference caused by dolomite and limestone, which is determined by temperature and acid diffusion coefficient. For feasibility, the effects of these parameters are neglected. The correlation to be developed is just for a typical temperature of 210 $^{o}$F and an acid diffusion coefficient of $6\times10^{-9}$ m$^2$ / $s$ . Fig. 5.55 shows the effect of

limestone percentage on the average fracture width. Data fitting gives the following correlation. The unit of $w_{dre}$ is millimeter, and the unit of $a_1$ is $(\text{millimeter})^{1-a_3}$.

$$\overline{w} = a_1 (f_{\text{limestone}})^{a_2} w_{dre}^{a_3} \quad \text{..... (5. 12)}$$

where

$a_1 = 0.21$ $a_2 = 0.56$ $a_3 = 0.84$

$f_{\text{limestone}}$ : limestone percentage

Fig. 5.56 shows the comparison of average fracture width between numerical calculation and correlation calculation.

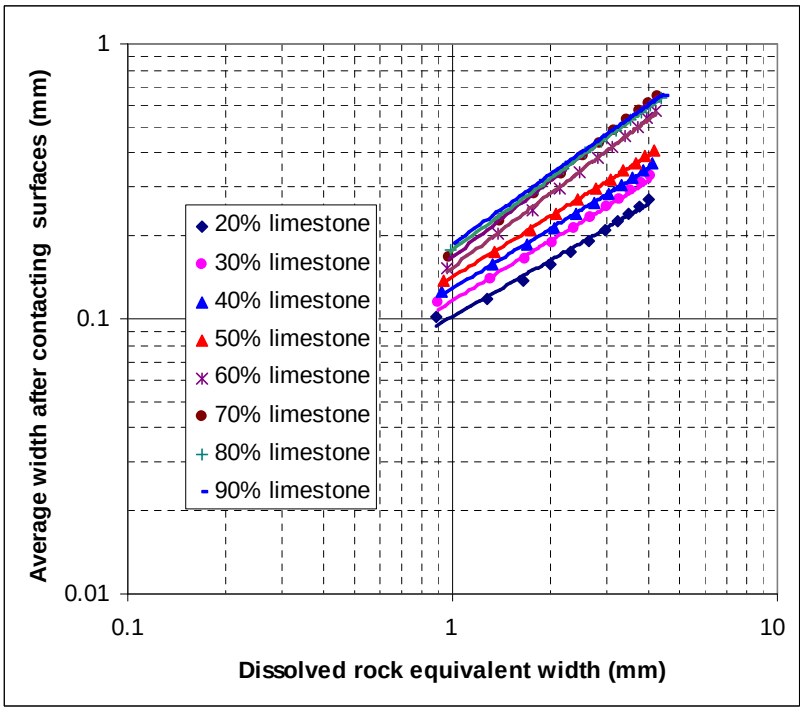


**Fig. 5.55 – Effect of limestone percentage on average fracture width (mineralogy distribution dominance).**

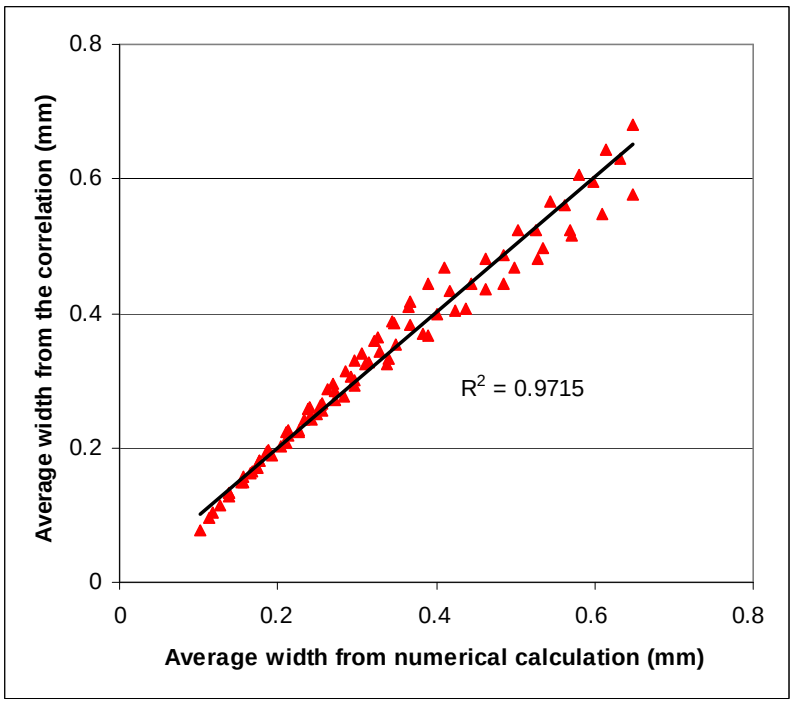


**Fig. 5.56 – Comparison of average fracture width between numerical calculation and correlation calculation (mineralogy distribution dominance).**

For the two extreme cases of 0% limestone and 100% limestone, the average fracture width is so small that the fracture is closed.

### 5.9.3 Competing Effects of Leakoff and Mineralogy Distributions

For this category, the mineralogy and permeability distributions affect the relationship between $w_{dre}$ and average fracture width. The permeability effect is determined by $\sigma_D$. Fig. 5.57 shows how $\sigma_D$ affects average width. The mineralogy effect can be divided into two aspects. One is the effect of limestone or dolomite percentage. Another is the effect of etching depth difference caused by dolomite and limestone, which is determined by temperature and acid diffusion coefficient. For feasibility, the

effects of these parameters are neglected. The correlation to be developed is just for a typical temperature of 210 $^{o}$F and an acid diffusion coefficient of $6\times10^{-9}$ $m^2/s$. Fig. 5.58 shows the effect of limestone percentage on the average facture width. Data fitting gives the following correlation. The unit of $w_{dre}$ is millimeter, and the unit of $a_1$ and $a_3$ is $(\text{millimeter})^{1-a_4}$.

$$\overline{w} = \left(a_1 (f_{\text{limestone}})^{a_2} + a_3\sigma_D\right) w_{dre}^{a_4} \quad \textbf{(5. 13)}$$

where

$a_1 = 0.16$ $a_2 = 0.43$ $a_3 = 0.22$ $a_4 = 0.84$

$f_{\text{limestone}}$ : limestone percentage

Fig. 5.59 shows the comparison of average fracture width between numerical calculation and correlation calculation.

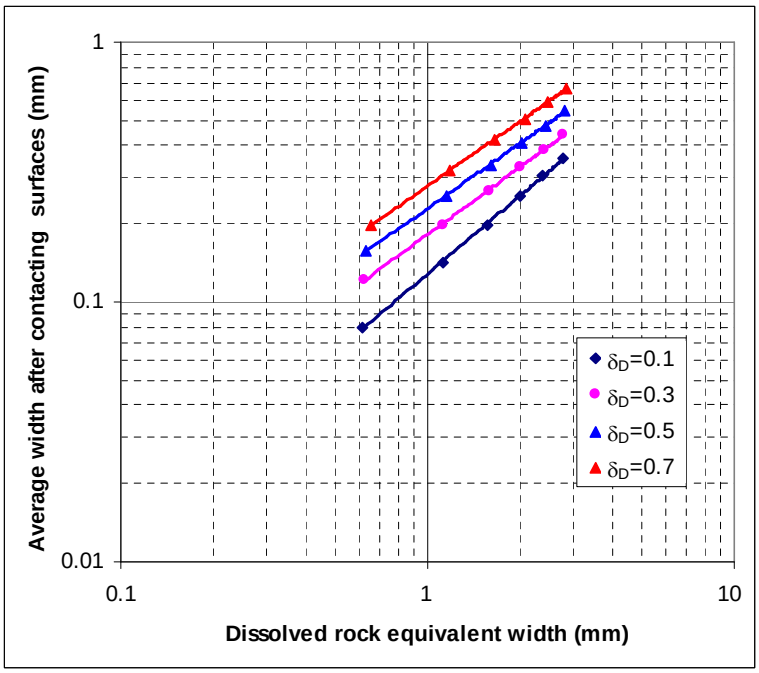


**Fig. 5.57 – Effect of $\sigma_D$ on average fracture width (competing effects of permeability and mineralogy distributions).**

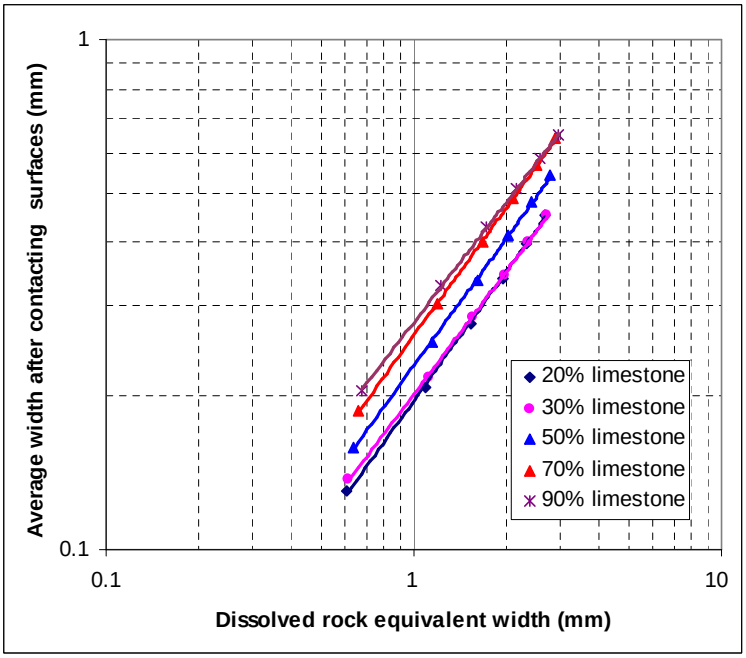


**Fig. 5.58 – Effect of limestone percentage on average fracture width (competing effects of permeability and mineralogy distributions).**

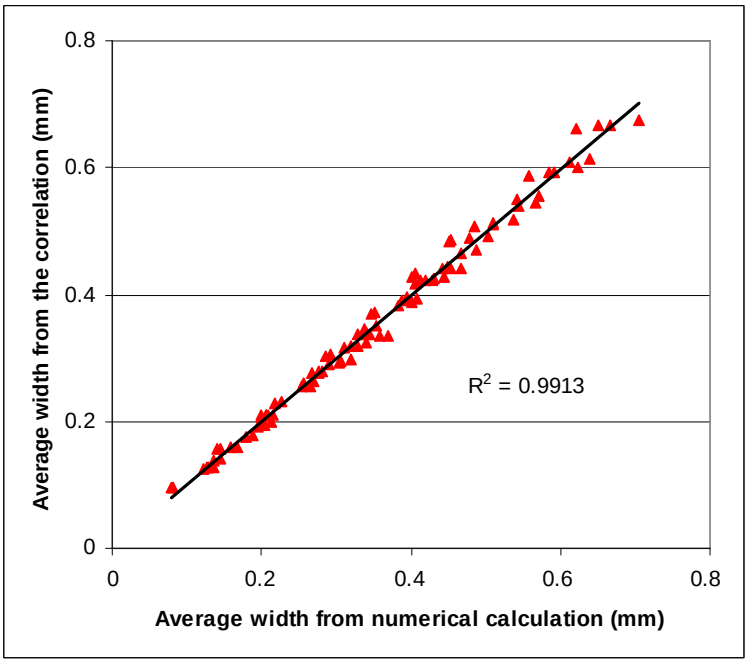


**Fig. 5.59 – Comparison of average fracture width between numerical calculation and correlation calculation (competing effects of permeability and mineralogy distributions).**

## 5.10 Summary of the Conductivity and Average Fracture Width Correlations

We summarize the correlations developed in the research here. According to the relative effect of permeability and mineralogy distributions on conductivity, three categories in acid fracturing are discussed: permeability distribution dominance, mineralogy distribution dominance, and combined effect of permeability and mineralogy distributions. Without the ability to develop a unified correlation for the three categories, we develop correlations for them separately.

1. Permeability distribution dominance

    - The conductivity correlation is

$$\left(k_f w\right)_0 = \frac{\overline{w}^3}{12}\left[1+\left(a_1 erf\left(a_2(\lambda_{D,x}-a_3)\right)-a_4 erf\left(a_5(\lambda_{D,z}-a_6)\right)\right)\sqrt{(e^{\sigma_D}-1)}\right] \text{..} \quad \textbf{(5. 14)}$$

where

$a_1 = 1.63$ $a_2 = 5.0$ $a_3 = 0.15$
$a_4 = 1.39$ $a_5 = 11.0$ $a_6 = 0.03$

- The average fracture width correlation is
  - ❖ High leakoff cases

    $$\overline{w} = a_1 erf\left(a_2 \sigma_D\right) w_{dre}^{a_3} \text{ ..... } \textbf{(5. 15)}$$

    where

    $a_1 = 0.99$ $a_2 = 0.80$ $a_3 = 0.80$

    The unit of $d_{dre}$ is millimeter, and the unit of $a_1$ is $\left(\text{millimeter}\right)^{1-a_3}$.

  - ❖ Medium leakoff with 0% limestone

    $$\overline{w} = a_1 erf\left(a_2 \sigma_D\right) w_{dre}^{a_3} \text{ ..... } \textbf{(5. 16)}$$

    where

    $a_1 = 0.43$ $a_2 = 0.69$ $a_3 = 0.71$

    The unit of $d_{dre}$ is millimeter, and the unit of $a_1$ is $\left(\text{millimeter}\right)^{1-a_3}$.

  - ❖ Medium leakoff with 100% limestone

    $$\overline{w} = a_1 erf\left(a_2 \sigma_D\right) w_{dre}^{a_3} \text{ ..... } \textbf{(5. 17)}$$

    where

    $a_1 = 0.36$ $a_2 = 0.88$ $a_3 = 0.71$

    The unit of $d_{dre}$ is millimeter, and the unit of $a_1$ is $\left(\text{millimeter}\right)^{1-a_3}$.

2. Mineralogy distribution dominance

   - The conductivity correlation is

$$\left(k_f w\right)_0 = \frac{\overline{w}^3}{12}\left[1 + a_1\left(1 - f_{\text{limestone}}\right)\right)^{a_2}\right] \quad \text{..... (5. 18)}$$

   where

$a_1 = 2.97$ $a_2 = 2.02$

   For 0% or 100% limestone, the average fracture width is so small that the fracture is closed.

   - The average fracture width correlation is

$$\overline{w} = a_1\left(f_{\text{limestone}}\right)^{a_2} w_{dre}^{a_3} \quad \text{..... (5. 19)}$$

   where

$a_1 = 0.21$ $a_2 = 0.56$ $a_3 = 0.84$

   The unit of $d_{dre}$ is millimeter, and the unit of $a_1$ is $\left(\text{millimeter}\right)^{1-a_3}$.

3. Combined effect of permeability and mineralogy distributions

   - The conductivity correlation is

$$\left(wk_f\right)_0 = \frac{\overline{w}^3}{12}\left[1 + a_1 + \left(a_2 erf\left(a_3(\lambda_{D,x} - a_4)\right) - a_5 erf\left(a_6(\lambda_{D,z} - a_7)\right)\right)\sqrt{(e^{\sigma_D} - 1)}\right] \quad \text{..... (5. 20)}$$

   where

$a_1 = 0.2$ $a_2 = 0.95$ $a_3 = 5.0$ $a_4 = 0.15$
$a_5 = 0.6$ $a_6 = 12.2$ $a_7 = 0.03$

   - The average fracture width correlation is

$$\overline{w} = \left(a_1\left(f_{\text{limestone}}\right)^{a_2} + a_3\sigma_D\right)w_{dre}^{a_4} \quad \text{..... (5. 21)}$$

where

$a_1 = 0.16$ $a_2 = 0.43$ $a_3 = 0.22$ $a_4 = 0.84$

The unit of $d_{dre}$ is millimeter, and the unit of $a_1$ and $a_3$ is $(\text{millimeter})^{1-a_4}$.

# CHAPTER VI

# CONCLUSIONS AND RECOMMENDATIONS

## 6.1 Conclusions

The intermediate-scale acid fracturing model with grid size small enough and total dimension big enough to capture local and macro-scale heterogeneities developed in the research simulates acid fracture surface etching profiles with acid injection. By bringing the two fracture surfaces into contact, we obtain the fracture width distribution at zero closure stress, based on which we calculate conductivity by simulating fluid flow in the fracture. Permeability and mineralogy distributions on the fracture surfaces are generated by using GSLIB by considering their spatial distribution characteristics. With the model we found the effect of parameters on etching patterns and conductivity as follows.

1. Permeability and mineralogy distributions determine the fracture surface etching patterns, which determine conductivity. According to their relative effects, surface etching patterns can be classified into three categories: permeability distribution dominance, mineralogy distribution dominance, and competing effect of permeability and mineralogy distributions.
2. How fracture roughness affects conductivity depends on the spatial distribution of the roughness. Random roughness distribution makes void spaces isolated from each other. The conductivity is lower than the one calculated using the cubic law and the average fracture width. The rougher

the surface, the higher the conductivity for the same acid contact time. A strong spatially correlated roughness distribution in the horizontal direction leads to the formation of channels, which contribute greatly to conductivity because of negligible pressure drop for fluid flow in channels. The deeper the channels, the higher the conductivity for the same acid contact time. The conductivity is higher than that calculated using the cubic law and the average fracture width.

3. Compared to permeability and mineralogy distributions, other parameters such as injection conditions and acid properties have negligible effects on etching patterns. Temperature affects etching depth difference caused by limestone and dolomite. At very high temperature, limestone causes negligible deeper etching depth than dolomite, but at low temperature, the difference is appreciable.
4. Conditions leading to deep, narrow channels are high horizontal correlation length, low vertical correlation length for permeability and mineralogy distributions, high standard deviation of permeability distribution, and low temperature.
5. With the model, we did extensive numerical experiments to develop acid fracture conductivity correlations at zero closure stress as a function of statistical parameters of permeability and mineralogy distributions and average fracture width. Without the ability to develop a unified correlation

for the three categories of etching patterns, we developed correlations separately for the three categories.

6. Using the correlations of conductivity need the average fracture width at zero closure stress. Therefore, we developed average fracture width correlations for the three categories separately as a function of statistical parameters of permeability and mineralogy distributions and dissolved rock equivalent width, which is the dissolved rock volume divided by the fracture area.

**6.2 Recommendations**

In acid fracturing, pressure in the fracture affects fracture dynamic fracture width so as to affect acid transport, which is not considered in the model. An improvement to the model is to include the pressure effect on dynamic fracture width. Natural fractures, a common feature in carbonate reservoirs, affects acid leakoff in a different manner from matrix. This research did not study the effect of natural fractures on leakoff. It is recommended to study the effect of natural fractures on leakoff. In the model we use 30% of leakoff acid to etch fracture surfaces, which is determined from experiments. It would be helpful to do extensive experiments for different mineralogy, acid type, and leakoff conditions. When bringing the two fracture surfaces into contact for conductivity calculation at zero closure stress, we firstly did it for every cross section and then connect all cross sections to get the fracture profiles. Contacting the two fracture surfaces in three-dimension will improve results. For mineralogy distribution, we just

consider dolomite and limestone. It is recommended to include the effect of HCl insoluble material.

# NOMENCLATURE

All variables in SI unit

$b(x,z,t)$ = fracture width

$b(x,z)$ = fracture width distribution after bringing the two surfaces into contact

$b_{\min}$ = minimum fracture width

$C_c$ = compressibility fluid-loss coefficient

$C_{v,mh}$ = viscous fluid-loss coefficient with wormhole

$C_{wh}$ = overall leakoff coefficient with wormhole

$C_i$ = injection acid concentration

$C_D$ = dimensionless acid concentration

$D_{eff}$ = effective acid diffusion coefficient

$Ef$ = reaction rate constant

$f$ = percentage of leakoff acid etching fracture surfaces

$H$ = fracture height

$J$ = Jacobian

$k_f w$ = fracture conductivity

$L$ = fracture length

$MW_{acid}$ = molecular weight of the acid

$n'$ = reaction rate order constant

$p(x,y,z)$ = pressure in the 3D intermediate-scale model

$p(x,z)$ = pressure distribution inside a fracture in conductivity calculation

$p_0$ = outlet pressure in the 3D intermediate-scale model

$\Delta p$ = pressure drop between inlet and outlet in conductivity calculation

$p_{in}$ = pressure at inlet in conductivity calculation

$p_{out}$ = pressure at outlet in conductivity calculation

$q$ = flux in conductivity calculation

$Q_{inj}$ = injection rate in the 3D intermediate-scale model

$Q_{ibt}$ = breakthrough pore volume for acid in a core flood

$t$ = time

$u$ = velocity in the x direction

$U$ = velocity in the $\xi$ direction in computation domain

$v$ = velocity in the y direction

$v_L$ = leakoff velocity

$V$ = velocity in the $\eta$ direction in computation domain

$w$ = velocity in the z direction

$\overline{w}$ = average fracture width

$w_{dre}$ = dissolved rock equivalent width

$w_i$ = idea fracture width

$W$ = velocity in the $\zeta$ direction in computation domain

$x_\xi$ = derivative of x with respect to $\xi$

$y_1(x,z,t)$ = position of one fracture surface

$y_2(x,z,t)$ = position of one fracture surface

$\beta$ = gravitational dissolving power

$\zeta$ = coordinate in computation domain

$\eta$ = coordinate in computation domain

$\lambda_x$ = the horizontal correlation length

$\lambda_z$ = the vertical correlation length

$\lambda_{D,x}$ = the dimensionless horizontal correlation length

$\lambda_{D,z}$ = the dimensionless vertical correlation length

$\mu$ = viscosity

$\xi$ = coordinate in computation domain

$\rho$ = density

$\sigma_D$ = dimensionless standard deviation of permeability

$\phi$ = porosity

# REFERENCES

Acharya, S. and Moukalled, F.H. 1989. Improvements to in Compressible Flow Calculation on a Non-staggered Curvilinear Grid. *Numerical Heat Transfer, Part B*, **15**: 131-152.

Blatt. H., Middleton, G., and Murray, R. 1980. *Origin of Sedimentary Rocks*. Second edition. Englewood Cliffs, New Jersey: Prentice-Hall, Inc.

Brown, S.R. 1987. Fluid Flow through Rock Joints: The Effect of Surface Roughness. *J. Geophys. Res.* **92**(B2): 1337-1347.

Brown, S.R. 1995. Simple Mathematical Model of a Rough Fracture. *J. Geophys. Res.* **100**(B4): 5941-5952.

Brush, D.J. and Thomson, N.R. 2003. Fluid Flow in Synthetic Rough-Walled Fractures: Navier-Stokes, Stokes and Local Cubic Law Simulations. *Water Resource Res.* **39**(4): 5-1~5-15.

Chung, T.J. 2002. *Computational Fluid Dynamics*. New York: Cambridge University Press.

Coakley, K., Muralidhar, K., Long, J.C.S., and Myer, L.R 1987. Equivalent Permeability of Statistically Simulated Single Fracture. *Proceedings of the Conference on Geostatistical, Sensitivity, and Uncertainty Methods for Ground-Water Flow and Radionuclide Transport Modeling*, San Francisco, California, Sept. 15-17, edited by Buxton, B.E., pp. 441-469.

Conway, M.W., Asadi, M., Penny, G.S., and Chang, F. 1999. A Comparative Study of Straight/Gelled/Emulsified Hydrochloric Acid Diffusivity Coefficient Using

Diaphragm Cell and Rotating Disk, paper SPE 56532 presented at 1999 SPE Annual Technical Conference and Exhibition, Houston, Texas, 3-6 October.

Coulter, A.W., Alderman, E.N., Cloud, J.E., and Crowe, C.W. 1974. Mathematical Model Simulates Actual Well Conditions in Fracture Acidizing Treatment Design. Paper SPE 5004 presented at the SPE-AIME 49th Annual Fall Meeting, Houston, 6-9 Oct.

Crank, J. 1984: *Free and Moving Boundary Problems*. New York: Clarendon Press.

Daccord, E., Touboul, E., and Lenormand, R. 1989. Carbonate Acidizing: Toward a Quantitative Model of the Wormholing Phenomenon. *SPEPE*, Feb., 63-68.

De Rozieres, J., Chang, F.F., and Sullivan, R.B. 1994. Measuring Diffusion Coefficients in Acid Fracturing Fluids and Their Application to Gelled and Emulsified Acids, paper SPE 28552 presented at the 1994 SPE Annual Conference and Exhibition, New Orleans, LA, 25-28 September.

Deutsch, C.V., and Journel, A.G. 1998. *GSLIB Geostatistical Software Library and User's Guide*. New York: Oxford University Press.

Dong C. 2001. Acidizing of Naturally-Fractured Reservoir Formations. Ph.D. dissertation, the University of Texas at Austin.

Goggin, D.J., Kocurek, G., and Lake, L.W. 1992. Permeability Transects of Eolian Sands and Their Use in Generating Random Permeability Fields. *SPE Formation Evaluation*, March, 7-16.

Gong, M. 1997. Mechanical and Hydraulic Behavior of Acid Fractures – Experimental Studies and Mathematical Modeling. Ph.D. dissertation, the University of Texas at Austin.

Hardy, H.H. and Beier, R.A. 1994. *Fractals in Reservoir Engineering*. River Edge, New Jersey: World Scientific Publishing Co. Pte. Ltd.

Hill, A.D., Zhu, D., and Wang, Y.M., 1995. The Effect of Wormholing on the Fluid-Loss Coefficient in Acid Fracturing. *SPE Production & Facilities*, November, 257-263.

Huang, T.P. 2000. Wormhole Modeling in Carbonate Acidizing. Ph.D. dissertation, the University of Texas, Austin.

Hung, K.M. 1987. Modeling of Wormhole Behavior in Carbonate Acidizing. Ph.D. dissertation, University of Texas, Austin.

Hung, K.M., Hill, A.D., and Sepehrnoori, K. 1989. A Mechanistic Model of Wormhole Growth in Carbonate Matrix Acidizing and acid Fracturing. *JPT*, January, 59-66.

Iwai, K. 1976. Fundamental Study of the Fluid Flow through a Single Fracture, Ph.D. thesis, Univ. of California, Berkeley.

Kim I. 2002. Fluid Flow in a Rock Fracturing Using Finite Difference Lattice Boltsmann Method. Ph.D. dissertation, State University of New York, Stony Brook.

Lo, K.K. and Dean, R.H. 1989. Modeling of Acid Fracturing. *SPE Production Engineering*, **4**(2): 194-200.

Lucia F.J. 1999. *Carbonate Reservoir Characterization*. New York: Springer.

Lund, K., Fogler, H. S., and McCune, C. C. 1973. Acidizing I: the Dissolution of Dolomite in Hydrochloric Acid. *Chem. Eng. Sci.*, **28**: 691-700.

Lund, K., Fogler, H. S., McCune, C. C., and Ault, J. W. 1975. Acidizing II: the Dissolution of Calcite in Hydrochloric Acid. Acid. *Chem. Eng. Sci.*, **30**: 825-835.

Moreno, L, Tsang, Y.W., Tsang, C.F., Hale, F.V., and Neretnieks, I. 1988. Flow and Tracer Transport in a Single Fracture, a Stochastic Model and Its Relation to Some Field Observation. *Water Resource Res*. **24**(12): 2033-2048.

Mourzenko, V.V., Thovert, J.F., and Adler, P.M., 1995. Permeability of a Single Fracture; Validity of the Reynolds Equation. *J. Phys. II* **5**: 465-482.

Muralidhar K. and Long J.C.S., 1987. A New Approach to Characterizing Flow in Single Fractures. In: D.D. Evans and T.J. Nicholson, Editors, *Flow and Transport Through Unsaturated Fractured Rock, American Geophysical Union Geophysical Monograph Series* **42**: 115–120.

Murphy, J.R., and Thomson, N.R. 1993. Two-Phase Flow in a Variable Aperture Fracture. *Water Resource Res.* **29**(10): 3453-3476.

Navarrete, R.C., Miller, M.J., and Gordon, J.E. 1998. Laboratory and Theoretical Studies for Acid Fracture Stimulation Optimization, paper SPE 39776 presented at the 1998 SPE Permian Basin Oil and Gas Recovery Conference, Midland, Texas, 23-26 March.

Nierode, C.E., Williams, B.B, and Bombardieri, C.C. 1972. Prediction of Stimulation from Acid Fracture Treatments. *J. Cnd. Pet. Tech.* 1-11.

Nierode, D.E. and Kruk, K. F. 1973: An Evaluation of Acid Fluid Loss Additives, Retarded Acids, and Acidized Fracture Conductivity. Paper SPE 4549, presented at the 48th Annual Fall Meeting of the Society of Petroleum Engineers of AIME, Sep. 30 - Oct. 3, Las Vegas.

Patankar, S.V. 1980. *Numerical Heat Transfer and Fluid Flow*. New York: Hemisphere Publishing Corporation.

Patir, N., and Cheng, H.S. 1978: "An Average Flow Model for Determining Effects of Three dimensional Roughness on Partial Hydrodynamic Lubrication," *J. Lubr. Technol*. **100**: 12-17.

Pournik, M. 2008. Laboratory-Scale Fracture Conductivity Created by Acid Etching. Ph.D. dissertation, Texas A&M University, College Station.

Pruess, K., and Tsang Y.W. 1990. On Two-Phase Relative Permeability and Capillary Pressure of a Rough-Walled Fracture, *Water Resource Res*., **26**(9): 1915-1926.

Rhie, C.M. 1985. A Three-Dimensional Passage Flow Analysis Method Aimed at Centrifugal Impellers. *Computers & Fluids* **13**(4): 443-460.

Roberts, L.D. and Guin, J.A. 1975. The Effect of Surface Kinetics in Fracture Acidizing. *SPEJ* **8**: 385-395.

Romero, J., Gu, H., and Gulrajani, S.N. 1998. Three-Dimensional Transport in Acid Fracturing in Acid Fracturing Treatments: Theoretical Development and Consequences for Hydrocarbon Production. Paper SPE 39956 presented at the 1998 SPE Rocky Mountain Regional/Low-Permeability Reservoirs Symposium and Exhibition, Denver, Colorado, 5-8 April.

Rozieres, J.D., Chang, F.F., and Sullivan, R.B. 1994. Measuring Diffusion Coefficients in Acid Fracturing Fluids and Their Application to Gelled and Emulsified Acids. Paper SPE 28552 presented at the SPE 69th Annual Technical Conference and Exhibition held in New Orleans, LA, 25-28 Sep.

Sarkar, S., Toksoz, M.N, and Burns, D.R. 2004. Fluid Flow Modeling in Fractures. (http://www.eaps.mit.edu/erl/research/report1/reports.html).

Settrari A. 1985. A New General Model of Fluid Loss in Hydraulic Fracturing. *SPEJ*, Aug. 491-501.

Settari, A. 1993. Modeling of Acid-Fracturing Treatments. *SPE Production & Facilities* February, 30-38.

Settari, A., Sullivan, R.B., and Hansen, C. 2001. A New Two-Dimensional Model for Acid-Fracturing Design. *SPE Production & Facilities* November, 200-209.

Tsang, Y.W. 1984. The Effect of Tortuosity on Fluid Flow through a Single Fracture. *Water Resource Res.*, **20**(9): 1209-1215.

Tsang, Y.W., and Tsang, C.F. 1989. Flow Channeling in a Single Fracture as a Two-Dimensional Strongly Heterogeneous Permeable Medium. *Water Resource Res.* **25**(9): 2076-2080.

Terrill, R.M. 1965. Heat Transfer in Laminar Flow between Parallel Porous Plates. *Intl. J. Heat Transfer* **8**: 1491-97.

Van Domselaar, H.R., Schols, R.S., and Visser, W. 1973. An Analysis of the Acidizing Process in Acid Fracturing. *SPEJ* **8**: 239-250.

Verberg, R., and Ladd, A.J.C. 2002. Simulation Chemical Erosion in Rough Fractures. *Physical Review E*. **65**: 056311-1~056311-6.

Walsh, J.B. 1981: "Effect of Pore Pressure and Confining Pressure on Fracture Permeability," *Int. J. Rock Mech. Min. Sci. Geomech. Abstr*. **18**: 429-435.

Wang, Y.M. 1993. Existence of an Optimal Injection Rate in Carbonate Acidizing and the Effect of Rock Heterogeneity on Wormhole Patterns. Ph.D. dissertation, The University of Texas at Austin.

Williams, B.B. and Nierode D.E. 1972. Design of Acid Fracturing Treatments. *J. Pet. Tech* **7**: 849-859.

Witherspoon, P.A., Wang, J.S.Y., Iwai, K., and Gale, J.E. 1980. Validity of Cubic Law for Fluid Flow in a Deformable Rock Fracture. *Water Resource Res.*, **16**(6): 1016-1024.

Zimmerman, R.W., Al-Yaarubi, A., Pain, C.C., and Grattoni, C, A. 2004. Non-linear Regimes of Fluid Flow in Rock Fractures. *Int. J. Rock Mech. Sci.* **41**(3): 163-169.

# APPENDIX A

# COORDINATE TRANSFORMATION

We use the front-fixing method to handle the irregular moving boundaries in numerical calculation. Using body-fitted coordinate transformation, we transform partial differential equations from $(x, y, z)$ to $(\xi, \eta, \zeta)$ . The following is the detail of the coordinate transformation.

## A-1 Navier-Stokes Equations

In every time step, solve incompressible steady-state Navier-Stokes equations, so it has nothing to with time. In new coordinates, define contravariant velocity components as

$$U = J\left(u\xi_x + v\xi_y + w\xi_z\right) \quad \textbf{(A. 1)}$$

$$V = J\left(u\eta_x + v\eta_y + w\eta_z\right) \quad \textbf{(A. 2)}$$

$$W = J\left(u\zeta_x + v\zeta_y + w\zeta_z\right) \quad \textbf{(A. 3)}$$

where $J$ is Jacobian defined as

$$J = \begin{vmatrix} x_\xi & x_\eta & x_\zeta \\ y_\xi & y_\eta & y_\zeta \\ z_\xi & z_\eta & z_\zeta \end{vmatrix} \quad \textbf{(A. 4)}$$

### A-1.1 Continuity Equation

$$\frac{\partial u}{\partial x} + \frac{\partial v}{\partial y} + \frac{\partial w}{\partial z} = 0 \quad \textbf{(A. 5)}$$

Multiplying Eq. (A. 5) by $J$ gives

$$J\left(\frac{\partial u}{\partial x}+\frac{\partial v}{\partial y}+\frac{\partial w}{\partial z}\right)=0 \quad \text{..... (A. 6)}$$

Using the chain rule to Eq. (A. 6) leads to

$$\begin{aligned} &J\left(\frac{\partial u}{\partial \xi}\right)\left(\frac{\partial \xi}{\partial x}\right)+J\left(\frac{\partial u}{\partial \eta}\right)\left(\frac{\partial \eta}{\partial x}\right)+J\left(\frac{\partial u}{\partial \zeta}\right)\left(\frac{\partial \zeta}{\partial x}\right)+ \\ &J\left(\frac{\partial v}{\partial \xi}\right)\left(\frac{\partial \xi}{\partial y}\right)+J\left(\frac{\partial v}{\partial \eta}\right)\left(\frac{\partial \eta}{\partial y}\right)+J\left(\frac{\partial v}{\partial \zeta}\right)\left(\frac{\partial \zeta}{\partial y}\right)+ \\ &J\left(\frac{\partial w}{\partial \xi}\right)\left(\frac{\partial \xi}{\partial z}\right)+J\left(\frac{\partial w}{\partial \eta}\right)\left(\frac{\partial \eta}{\partial z}\right)+J\left(\frac{\partial w}{\partial \zeta}\right)\left(\frac{\partial \zeta}{\partial z}\right)=0 \end{aligned} \quad \text{..... (A. 7)}$$

Integration by part gives the following results:

$$J\left(\frac{\partial u}{\partial \xi}\right)\left(\frac{\partial \xi}{\partial x}\right)=\frac{\partial}{\partial \xi}\left(Ju\frac{\partial \xi}{\partial x}\right)-u\frac{\partial}{\partial \xi}\left(J\frac{\partial \xi}{\partial x}\right) \quad \text{..... (A. 8)}$$

$$J\left(\frac{\partial u}{\partial \eta}\right)\left(\frac{\partial \eta}{\partial x}\right)=\frac{\partial}{\partial \eta}\left(Ju\frac{\partial \eta}{\partial x}\right)-u\frac{\partial}{\partial \eta}\left(J\frac{\partial \eta}{\partial x}\right) \quad \text{..... (A. 9)}$$

$$J\left(\frac{\partial u}{\partial \zeta}\right)\left(\frac{\partial \zeta}{\partial x}\right)=\frac{\partial}{\partial \zeta}\left(Ju\frac{\partial \zeta}{\partial x}\right)-u\frac{\partial}{\partial \zeta}\left(J\frac{\partial \zeta}{\partial x}\right) \quad \text{..... (A. 10)}$$

$$J\left(\frac{\partial v}{\partial \xi}\right)\left(\frac{\partial \xi}{\partial y}\right)=\frac{\partial}{\partial \xi}\left(Jv\frac{\partial \xi}{\partial y}\right)-v\frac{\partial}{\partial \xi}\left(J\frac{\partial \xi}{\partial y}\right) \quad \text{..... (A. 11)}$$

$$J\left(\frac{\partial v}{\partial \eta}\right)\left(\frac{\partial \eta}{\partial y}\right)=\frac{\partial}{\partial \eta}\left(Jv\frac{\partial \eta}{\partial y}\right)-v\frac{\partial}{\partial \eta}\left(J\frac{\partial \eta}{\partial y}\right) \quad \text{..... (A. 12)}$$

$$J\left(\frac{\partial v}{\partial \zeta}\right)\left(\frac{\partial \zeta}{\partial y}\right)=\frac{\partial}{\partial \zeta}\left(Jv\frac{\partial \zeta}{\partial y}\right)-v\frac{\partial}{\partial \zeta}\left(J\frac{\partial \zeta}{\partial y}\right) \quad \text{..... (A. 13)}$$

$$J\left(\frac{\partial w}{\partial \xi}\right)\left(\frac{\partial \xi}{\partial z}\right)=\frac{\partial}{\partial \xi}\left(Jw\frac{\partial \xi}{\partial z}\right)-w\frac{\partial}{\partial \xi}\left(J\frac{\partial \xi}{\partial z}\right) \quad \text{..... (A. 14)}$$

$$J\left(\frac{\partial w}{\partial \eta}\right)\left(\frac{\partial \eta}{\partial z}\right)=\frac{\partial}{\partial \eta}\left(Jw\frac{\partial \eta}{\partial z}\right)-w\frac{\partial}{\partial \eta}\left(J\frac{\partial \eta}{\partial z}\right) \quad \textbf{(A. 15)}$$

$$J\left(\frac{\partial w}{\partial \zeta}\right)\left(\frac{\partial \zeta}{\partial z}\right)=\frac{\partial}{\partial \zeta}\left(Jw\frac{\partial \zeta}{\partial z}\right)-w\frac{\partial}{\partial \zeta}\left(J\frac{\partial \zeta}{\partial z}\right) \quad \textbf{(A. 16)}$$

Substituting the above equations into Eq. (A. 7) gives

$$\frac{\partial}{\partial \xi}\left(Ju\frac{\partial \xi}{\partial x}+Jv\frac{\partial \xi}{\partial y}+Jw\frac{\partial \xi}{\partial z}\right)+\frac{\partial}{\partial \eta}\left(Ju\frac{\partial \eta}{\partial x}+Jv\frac{\partial \eta}{\partial y}+Jw\frac{\partial \eta}{\partial z}\right)+$$
$$\frac{\partial}{\partial \zeta}\left(Ju\frac{\partial \zeta}{\partial x}+Jv\frac{\partial \zeta}{\partial y}+Jw\frac{\partial \zeta}{\partial z}\right)-u\left[\frac{\partial}{\partial \xi}\left(J\frac{\partial \xi}{\partial x}\right)+\frac{\partial}{\partial \eta}\left(J\frac{\partial \eta}{\partial x}\right)+\frac{\partial}{\partial \zeta}\left(J\frac{\partial \zeta}{\partial x}\right)\right]- \quad ..$$
$$v\left[\frac{\partial}{\partial \xi}\left(J\frac{\partial \xi}{\partial y}\right)+\frac{\partial}{\partial \eta}\left(J\frac{\partial \eta}{\partial y}\right)+\frac{\partial}{\partial \zeta}\left(J\frac{\partial \zeta}{\partial y}\right)\right]-w\left[\frac{\partial}{\partial \xi}\left(J\frac{\partial \xi}{\partial z}\right)+\frac{\partial}{\partial \eta}\left(J\frac{\partial \eta}{\partial z}\right)+\frac{\partial}{\partial \zeta}\left(J\frac{\partial \zeta}{\partial z}\right)\right]=0$$

..... **(A. 17)**

Using the definition of $J$ we have

$$\frac{\partial}{\partial \xi}\left(J\frac{\partial \xi}{\partial x}\right)=\frac{\partial}{\partial \xi}\left(y_\eta z_\zeta-y_\zeta z_\eta\right)=\frac{\partial}{\partial \xi}\left(y_\eta z_\zeta\right)-\frac{\partial}{\partial \xi}\left(y_\zeta z_\eta\right)$$
$$=\frac{\partial^2 y}{\partial \xi \partial \eta}z_\zeta+\frac{\partial^2 z}{\partial \xi \partial \zeta}y_\eta-\frac{\partial^2 y}{\partial \xi \partial \zeta}z_\eta-\frac{\partial^2 z}{\partial \xi \partial \eta}y_\zeta \quad \textbf{(A. 18)}$$

$$\frac{\partial}{\partial \eta}\left(J\frac{\partial \eta}{\partial x}\right)=\frac{\partial}{\partial \eta}\left(-y_\xi z_\zeta+y_\zeta z_\xi\right)=-\frac{\partial}{\partial \eta}\left(y_\xi z_\zeta\right)+\frac{\partial}{\partial \eta}\left(y_\zeta z_\xi\right)$$
$$=-\frac{\partial^2 y}{\partial \eta \partial \xi}z_\zeta-\frac{\partial^2 z}{\partial \eta \partial \zeta}y_\xi+\frac{\partial^2 y}{\partial \eta \partial \zeta}z_\xi+\frac{\partial^2 z}{\partial \eta \partial \xi}y_\zeta \quad \textbf{(A. 19)}$$

$$\frac{\partial}{\partial \zeta}\left(J\frac{\partial \zeta}{\partial x}\right)=\frac{\partial}{\partial \zeta}\left(y_\xi z_\eta-y_\eta z_\xi\right)=\frac{\partial}{\partial \zeta}\left(y_\xi z_\eta\right)-\frac{\partial}{\partial \zeta}\left(y_\eta z_\xi\right)$$
$$=\frac{\partial^2 y}{\partial \zeta \partial \xi}z_\eta+\frac{\partial^2 z}{\partial \zeta \partial \eta}y_\xi-\frac{\partial^2 y}{\partial \zeta \partial \eta}z_\xi-\frac{\partial^2 z}{\partial \zeta \partial \xi}y_\eta \quad \textbf{(A. 20)}$$

so

$$u\left[\frac{\partial}{\partial\xi}\left(J\frac{\partial\xi}{\partial x}\right)+\frac{\partial}{\partial\eta}\left(J\frac{\partial\eta}{\partial x}\right)+\frac{\partial}{\partial\zeta}\left(J\frac{\partial\zeta}{\partial x}\right)\right]=0 \quad \text{..... (A. 21)}$$

Similarly, we have

$$v\left[\frac{\partial}{\partial\xi}\left(J\frac{\partial\xi}{\partial y}\right)+\frac{\partial}{\partial\eta}\left(J\frac{\partial\eta}{\partial y}\right)+\frac{\partial}{\partial\zeta}\left(J\frac{\partial\zeta}{\partial y}\right)\right]=0 \quad \text{..... (A. 22)}$$

$$w\left[\frac{\partial}{\partial\xi}\left(J\frac{\partial\xi}{\partial z}\right)+\frac{\partial}{\partial\eta}\left(J\frac{\partial\eta}{\partial z}\right)+\frac{\partial}{\partial\zeta}\left(J\frac{\partial\zeta}{\partial z}\right)\right]=0 \quad \text{..... (A. 23)}$$

Therefore, after transformation, continuity equation in new curvilinear system is

$$\frac{\partial U}{\partial\xi}+\frac{\partial V}{\partial\eta}+\frac{\partial W}{\partial\zeta}=0 \quad \text{..... (A. 24)}$$

**A-1.2 Momentum Equations**

Three momentum equations have the similar format, so we can write them in a unified form:

$$\rho\left(u\frac{\partial\psi}{\partial x}+v\frac{\partial\psi}{\partial y}+w\frac{\partial\psi}{\partial z}\right)=-\frac{\partial p}{\partial i}+\mu\left(\frac{\partial^2\psi}{\partial x^2}+\frac{\partial^2\psi}{\partial y^2}+\frac{\partial^2\psi}{\partial z^2}\right) \quad \text{..... (A. 25)}$$

where

$\psi = u, v, w$

$i = x, y, z$

Multiplying Eq. (A. 25) by $J$ gives

$$\rho\left(uJ\frac{\partial\psi}{\partial x}+vJ\frac{\partial\psi}{\partial y}+wJ\frac{\partial\psi}{\partial z}\right)=-J\frac{\partial p}{\partial i}+\mu\left(J\frac{\partial^2\psi}{\partial x^2}+J\frac{\partial^2\psi}{\partial y^2}+J\frac{\partial^2\psi}{\partial z^2}\right) \quad \text{..... (A. 26)}$$

Using the chain rule we have

$$uJ\frac{\partial\psi}{\partial x}=uJ\xi_x\frac{\partial\psi}{\partial\xi}+Ju\eta_x\frac{\partial\psi}{\partial\eta}+uJ\zeta_x\frac{\partial\psi}{\partial\zeta} \quad \textbf{(A. 27)}$$

$$vJ\frac{\partial\psi}{\partial y}=vJ\xi_y\frac{\partial\psi}{\partial\xi}+vJ\eta_y\frac{\partial\psi}{\partial\eta}+vJ\zeta_y\frac{\partial\psi}{\partial\zeta} \quad \textbf{(A. 28)}$$

$$wJ\frac{\partial\psi}{\partial z}=wJ\xi_z\frac{\partial\psi}{\partial\xi}+wJ\eta_z\frac{\partial\psi}{\partial\eta}+wJ\zeta_z\frac{\partial\psi}{\partial\zeta} \quad \textbf{(A. 29)}$$

Integrating by part gives the following results:

$$uJ\xi_x\frac{\partial\psi}{\partial\xi}=\frac{\partial}{\partial\xi}\left(Ju\psi\xi_x\right)-\psi\frac{\partial}{\partial\xi}\left(Ju\xi_x\right) \quad \textbf{(A. 30)}$$

$$uJ\eta_x\frac{\partial\psi}{\partial\eta}=\frac{\partial}{\partial\eta}\left(Ju\psi\eta_x\right)-\phi\frac{\partial}{\partial\eta}\left(Ju\eta_x\right) \quad \textbf{(A. 31)}$$

$$uJ\zeta_x\frac{\partial\psi}{\partial\zeta}=\frac{\partial}{\partial\zeta}\left(Ju\psi\zeta_x\right)-\psi\frac{\partial}{\partial\zeta}\left(Ju\zeta_x\right) \quad \textbf{(A. 32)}$$

$$vJ\xi_y\frac{\partial\psi}{\partial\xi}=\frac{\partial}{\partial\xi}\left(Jv\psi\xi_y\right)-\psi\frac{\partial}{\partial\xi}\left(Jv\xi_y\right) \quad \textbf{(A. 33)}$$

$$vJ\eta_y\frac{\partial\psi}{\partial\eta}=\frac{\partial}{\partial\eta}\left(Jv\psi\eta_y\right)-\psi\frac{\partial}{\partial\eta}\left(Jv\eta_y\right) \quad \textbf{(A. 34)}$$

$$vJ\zeta_y\frac{\partial\psi}{\partial\zeta}=\frac{\partial}{\partial\zeta}\left(Jv\psi\zeta_y\right)-\psi\frac{\partial}{\partial\zeta}\left(Jv\zeta_y\right) \quad \textbf{(A. 35)}$$

$$wJ\xi_z\frac{\partial\psi}{\partial\xi}=\frac{\partial}{\partial\xi}\left(Jw\psi\xi_z\right)-\psi\frac{\partial}{\partial\xi}\left(Jw\xi_z\right) \quad \textbf{(A. 36)}$$

$$wJ\eta_z\frac{\partial\psi}{\partial\eta}=\frac{\partial}{\partial\eta}\left(Jw\psi\eta_z\right)-\psi\frac{\partial}{\partial\eta}\left(Jw\eta_z\right) \quad \textbf{(A. 37)}$$

$$wJ\zeta_z\frac{\partial\psi}{\partial\zeta}=\frac{\partial}{\partial\zeta}\left(Jw\psi\zeta_z\right)-\psi\frac{\partial}{\partial\zeta}\left(Jw\zeta_z\right) \quad \textbf{(A. 38)}$$

Using Eq. (A. 27) through (A. 38) we have

$$uJ\frac{\partial\psi}{\partial x}+vJ\frac{\partial\psi}{\partial y}+wJ\frac{\partial\psi}{\partial z}=\frac{\partial}{\partial\xi}\left(Ju\psi\xi_x+Jv\psi\xi_y+Jw\psi\xi_z\right)+$$
$$\frac{\partial}{\partial\eta}\left(Ju\psi\eta_x+Jv\psi\eta_y+Jw\psi\eta_z\right)+\frac{\partial}{\partial\zeta}\left(Ju\psi\zeta_x+Jv\psi\zeta_y+Jw\psi\zeta_z\right)-$$
$$\psi\frac{\partial}{\partial\xi}\left(Ju\xi_x\right)-\psi\frac{\partial}{\partial\eta}\left(Ju\eta_x\right)-\psi\frac{\partial}{\partial\zeta}\left(Ju\zeta_x\right)-\psi\frac{\partial}{\partial\xi}\left(Jv\xi_y\right)-\psi\frac{\partial}{\partial\eta}\left(Jv\eta_y\right)- \quad \textbf{(A. 39)}$$
$$\psi\frac{\partial}{\partial\zeta}\left(Jv\zeta_y\right)-\psi\frac{\partial}{\partial\xi}\left(Jw\xi_z\right)-\psi\frac{\partial}{\partial\eta}\left(Jw\eta_z\right)-\psi\frac{\partial}{\partial\zeta}\left(Jw\zeta_z\right)$$

Using the chain rule we have

$$-\psi\frac{\partial}{\partial\xi}\left(Ju\xi_x\right)=-\psi J\xi_x\frac{\partial u}{\partial\xi}-\psi u\frac{\partial}{\partial\xi}\left(J\xi_x\right) \quad \textbf{(A. 40)}$$

$$-\psi\frac{\partial}{\partial\eta}\left(Ju\eta_x\right)=-\psi J\eta_x\frac{\partial u}{\partial\eta}-\psi u\frac{\partial}{\partial\eta}\left(J\eta_x\right) \quad \textbf{(A. 41)}$$

$$-\psi\frac{\partial}{\partial\zeta}\left(Ju\zeta_x\right)=-\psi J\zeta_x\frac{\partial u}{\partial\zeta}-\psi u\frac{\partial}{\partial\zeta}\left(J\zeta_x\right) \quad \textbf{(A. 42)}$$

Using the above results we have

$$-\psi\frac{\partial}{\partial\xi}\left(Ju\xi_x\right)-\psi\frac{\partial}{\partial\eta}\left(Ju\eta_x\right)-\psi\frac{\partial}{\partial\zeta}\left(Ju\zeta_x\right)=$$
$$-\psi J\left(\xi_x\frac{\partial u}{\partial\xi}+\eta_x\frac{\partial u}{\partial\eta}+\zeta_x\frac{\partial u}{\partial\zeta}\right)-\psi u\left[\frac{\partial}{\partial\xi}\left(J\xi_x\right)+\frac{\partial}{\partial\eta}\left(J\eta_x\right)+\frac{\partial}{\partial\zeta}\left(J\zeta_x\right)\right] \quad \textbf{(A. 43)}$$
$$=-\psi J\frac{\partial u}{\partial x}$$

Similarly, we have

$$-\psi\frac{\partial}{\partial\xi}\left(Jv\xi_y\right)=-\psi J\xi_y\frac{\partial v}{\partial\xi}-\psi v\frac{\partial}{\partial\xi}\left(J\xi_y\right) \quad \textbf{(A. 44)}$$

$$-\psi\frac{\partial}{\partial\eta}\left(Jv\eta_y\right)=-\psi J\eta_y\frac{\partial v}{\partial\eta}-\psi v\frac{\partial}{\partial\eta}\left(J\eta_y\right) \quad \textbf{(A. 45)}$$

$$-\psi \frac{\partial}{\partial \zeta}\left(Jv\zeta_y\right) = -\psi J\zeta_y \frac{\partial v}{\partial \zeta} - \psi v \frac{\partial}{\partial \zeta}\left(J\zeta_y\right) \quad \textbf{(A. 46)}$$

$$-\psi \frac{\partial}{\partial \xi}\left(Jv\xi_y\right) - \psi \frac{\partial}{\partial \eta}\left(Jv\eta_y\right) - \psi \frac{\partial}{\partial \zeta}\left(Jv\zeta_y\right) =$$
$$-\psi J\left(\xi_y \frac{\partial v}{\partial \xi} + \eta_y \frac{\partial v}{\partial \eta} + \zeta_y \frac{\partial v}{\partial \zeta}\right) - \psi v\left[\frac{\partial}{\partial \xi}\left(J\xi_y\right) + \frac{\partial}{\partial \eta}\left(J\eta_y\right) + \frac{\partial}{\partial \zeta}\left(J\zeta_y\right)\right] \quad \textbf{(A. 47)}$$
$$= -\psi J \frac{\partial v}{\partial y}$$

$$-\psi \frac{\partial}{\partial \xi}\left(Jw\xi_z\right) = -\psi J\xi_z \frac{\partial w}{\partial \xi} - \psi w \frac{\partial}{\partial \xi}\left(J\xi_z\right) \quad \textbf{(A. 48)}$$

$$-\psi \frac{\partial}{\partial \eta}\left(Jw\eta_z\right) = -\psi J\eta_z \frac{\partial w}{\partial \eta} - \psi w \frac{\partial}{\partial \eta}\left(J\eta_z\right) \quad \textbf{(A. 49)}$$

$$-\psi \frac{\partial}{\partial \zeta}\left(Jw\zeta_z\right) = -\psi J\zeta_z \frac{\partial w}{\partial \zeta} - \psi w \frac{\partial}{\partial \zeta}\left(J\zeta_z\right) \quad \textbf{(A. 50)}$$

$$-\psi \frac{\partial}{\partial \xi}\left(Jw\xi_z\right) - \psi \frac{\partial}{\partial \eta}\left(Jw\eta_z\right) - \psi \frac{\partial}{\partial \zeta}\left(Jw\zeta_z\right) =$$
$$-\psi J\left(\xi_z \frac{\partial w}{\partial \xi} + \eta_z \frac{\partial w}{\partial \eta} + \zeta_z \frac{\partial w}{\partial \zeta}\right) - \psi w\left[\frac{\partial}{\partial \xi}\left(J\xi_z\right) + \frac{\partial}{\partial \eta}\left(J\eta_z\right) + \frac{\partial}{\partial \zeta}\left(J\zeta_z\right)\right] \quad \textbf{(A. 51)}$$
$$= -\psi J \frac{\partial w}{\partial z}$$

so

$$-\psi \frac{\partial}{\partial \xi}\left(Ju\xi_x\right) - \psi \frac{\partial}{\partial \eta}\left(Ju\eta_x\right) - \psi \frac{\partial}{\partial \zeta}\left(Ju\zeta_x\right) - \psi \frac{\partial}{\partial \xi}\left(Jv\xi_y\right) - \psi \frac{\partial}{\partial \eta}\left(Jv\eta_y\right)$$
$$-\psi \frac{\partial}{\partial \zeta}\left(Jv\zeta_y\right) - \psi \frac{\partial}{\partial \xi}\left(Jw\xi_z\right) - \psi \frac{\partial}{\partial \eta}\left(Jw\eta_z\right) - \psi \frac{\partial}{\partial \zeta}\left(Jw\zeta_z\right) \quad \textbf{(A. 52)}$$
$$= -\psi J\left(\frac{\partial u}{\partial x} + \frac{\partial v}{\partial y} + \frac{\partial w}{\partial z}\right) = 0$$

Therefore, after transformation, the left-hand side of momentum equations becomes

$$uJ\frac{\partial\psi}{\partial x}+vJ\frac{\partial\psi}{\partial y}+wJ\frac{\partial\psi}{\partial z}=\frac{\partial}{\partial\xi}(\psi U)+\frac{\partial}{\partial\eta}(\psi V)+\frac{\partial}{\partial\zeta}(\psi W) \quad \text{..... (A. 53)}$$

Now transform the right-hand side of the momentum equations. Using the chain rule we have

$$J\frac{\partial^2\psi}{\partial x^2}=J\frac{\partial}{\partial x}\left(\frac{\partial\psi}{\partial x}\right)=J\xi_x\frac{\partial}{\partial\xi}\left(\frac{\partial\psi}{\partial x}\right)+J\eta_x\frac{\partial}{\partial\eta}\left(\frac{\partial\psi}{\partial x}\right)+J\zeta_x\frac{\partial}{\partial\zeta}\left(\frac{\partial\psi}{\partial x}\right) \text{.... (A. 54)}$$

$$J\xi_x\frac{\partial}{\partial\xi}\left(\frac{\partial\psi}{\partial x}\right)=\frac{\partial}{\partial\xi}\left(J\xi_x\frac{\partial\psi}{\partial x}\right)-\frac{\partial\psi}{\partial x}\frac{\partial}{\partial\xi}(J\xi_x) \quad \text{..... (A. 55)}$$

$$J\eta_x\frac{\partial}{\partial\eta}\left(\frac{\partial\psi}{\partial x}\right)=\frac{\partial}{\partial\eta}\left(J\eta_x\frac{\partial\psi}{\partial x}\right)-\frac{\partial\psi}{\partial x}\frac{\partial}{\partial\eta}(J\eta_x) \quad \text{..... (A. 56)}$$

$$J\zeta_x\frac{\partial}{\partial\zeta}\left(\frac{\partial\psi}{\partial x}\right)=\frac{\partial}{\partial\zeta}\left(J\zeta_x\frac{\partial\psi}{\partial x}\right)-\frac{\partial\psi}{\partial x}\frac{\partial}{\partial\zeta}(J\zeta_x) \quad \text{..... (A. 57)}$$

so

$$\begin{aligned}J\frac{\partial^2\psi}{\partial x^2}&=\frac{\partial}{\partial\xi}\left(J\xi_x\frac{\partial\psi}{\partial x}\right)+\frac{\partial}{\partial\eta}\left(J\eta_x\frac{\partial\psi}{\partial x}\right)+\frac{\partial}{\partial\zeta}\left(J\zeta_x\frac{\partial\psi}{\partial x}\right)-\\&\quad\frac{\partial\psi}{\partial x}\left[\frac{\partial}{\partial\xi}(J\xi_x)+\frac{\partial}{\partial\eta}(J\eta_x)+\frac{\partial}{\partial\zeta}(J\zeta_x)\right]\\&=\frac{\partial}{\partial\xi}\left(J\xi_x\frac{\partial\psi}{\partial x}\right)+\frac{\partial}{\partial\eta}\left(J\eta_x\frac{\partial\psi}{\partial x}\right)+\frac{\partial}{\partial\zeta}\left(J\zeta_x\frac{\partial\psi}{\partial x}\right)\end{aligned} \quad \text{..... (A. 58)}$$

Similarly we have

$$J\frac{\partial^2\psi}{\partial y^2}=J\frac{\partial}{\partial y}\left(\frac{\partial\psi}{\partial y}\right)=J\xi_y\frac{\partial}{\partial\xi}\left(\frac{\partial\psi}{\partial y}\right)+J\eta_y\frac{\partial}{\partial\eta}\left(\frac{\partial\psi}{\partial y}\right)+J\zeta_y\frac{\partial}{\partial\zeta}\left(\frac{\partial\psi}{\partial y}\right) \text{... (A. 59)}$$

$$J\xi_y\frac{\partial}{\partial\xi}\left(\frac{\partial\psi}{\partial y}\right)=\frac{\partial}{\partial\xi}\left(J\xi_y\frac{\partial\psi}{\partial y}\right)-\frac{\partial\psi}{\partial y}\frac{\partial}{\partial\xi}(J\xi_y) \quad \text{..... (A. 60)}$$

$$J\eta_y \frac{\partial}{\partial \eta}\left(\frac{\partial \psi}{\partial y}\right) = \frac{\partial}{\partial \eta}\left(J\eta_y \frac{\partial \psi}{\partial y}\right) - \frac{\partial \psi}{\partial y}\frac{\partial}{\partial \eta}\left(J\eta_y\right) \quad \textbf{(A. 61)}$$

$$J\zeta_y \frac{\partial}{\partial \zeta}\left(\frac{\partial \psi}{\partial y}\right) = \frac{\partial}{\partial \zeta}\left(J\zeta_y \frac{\partial \psi}{\partial y}\right) - \frac{\partial \psi}{\partial y}\frac{\partial}{\partial \zeta}\left(J\zeta_y\right) \quad \textbf{(A. 62)}$$

$$\begin{aligned} J\frac{\partial^2 \psi}{\partial y^2} &= \frac{\partial}{\partial \xi}\left(J\xi_y \frac{\partial \psi}{\partial y}\right) + \frac{\partial}{\partial \eta}\left(J\eta_y \frac{\partial \psi}{\partial y}\right) + \frac{\partial}{\partial \zeta}\left(J\zeta_y \frac{\partial \psi}{\partial y}\right) - \\ &\quad \frac{\partial \psi}{\partial y}\left[\frac{\partial}{\partial \xi}\left(J\xi_y\right) + \frac{\partial}{\partial \eta}\left(J\eta_y\right) + \frac{\partial}{\partial \zeta}\left(J\zeta_y\right)\right] \\ &= \frac{\partial}{\partial \xi}\left(J\xi_y \frac{\partial \psi}{\partial y}\right) + \frac{\partial}{\partial \eta}\left(J\eta_y \frac{\partial \psi}{\partial y}\right) + \frac{\partial}{\partial \zeta}\left(J\zeta_y \frac{\partial \psi}{\partial y}\right) \end{aligned} \quad \textbf{(A. 63)}$$

$$J\frac{\partial^2 \psi}{\partial z^2} = J\frac{\partial}{\partial z}\left(\frac{\partial \psi}{\partial z}\right) = J\xi_z \frac{\partial}{\partial \xi}\left(\frac{\partial \psi}{\partial z}\right) + J\eta_z \frac{\partial}{\partial \eta}\left(\frac{\partial \psi}{\partial z}\right) + J\zeta_z \frac{\partial}{\partial \zeta}\left(\frac{\partial \psi}{\partial z}\right) \quad \textbf{(A. 64)}$$

$$J\xi_z \frac{\partial}{\partial \xi}\left(\frac{\partial \psi}{\partial z}\right) = \frac{\partial}{\partial \xi}\left(J\xi_z \frac{\partial \psi}{\partial z}\right) - \frac{\partial \psi}{\partial z}\frac{\partial}{\partial \xi}\left(J\xi_z\right) \quad \textbf{(A. 65)}$$

$$J\eta_z \frac{\partial}{\partial \eta}\left(\frac{\partial \psi}{\partial z}\right) = \frac{\partial}{\partial \eta}\left(J\eta_z \frac{\partial \psi}{\partial z}\right) - \frac{\partial \psi}{\partial z}\frac{\partial}{\partial \eta}\left(J\eta_z\right) \quad \textbf{(A. 66)}$$

$$J\zeta_z \frac{\partial}{\partial \zeta}\left(\frac{\partial \psi}{\partial z}\right) = \frac{\partial}{\partial \zeta}\left(J\zeta_z \frac{\partial \psi}{\partial z}\right) - \frac{\partial \psi}{\partial z}\frac{\partial}{\partial \zeta}\left(J\zeta_z\right) \quad \textbf{(A. 67)}$$

$$\begin{aligned} J\frac{\partial^2 \psi}{\partial z^2} &= \frac{\partial}{\partial \xi}\left(J\xi_z \frac{\partial \psi}{\partial z}\right) + \frac{\partial}{\partial \eta}\left(J\eta_z \frac{\partial \psi}{\partial z}\right) + \frac{\partial}{\partial \zeta}\left(J\zeta_z \frac{\partial \psi}{\partial z}\right) - \\ &\quad \frac{\partial \psi}{\partial z}\left[\frac{\partial}{\partial \xi}\left(J\xi_z\right) + \frac{\partial}{\partial \eta}\left(J\eta_z\right) + \frac{\partial}{\partial \zeta}\left(J\zeta_z\right)\right] \\ &= \frac{\partial}{\partial \xi}\left(J\xi_z \frac{\partial \psi}{\partial z}\right) + \frac{\partial}{\partial \eta}\left(J\eta_z \frac{\partial \psi}{\partial z}\right) + \frac{\partial}{\partial \zeta}\left(J\zeta_z \frac{\partial \psi}{\partial z}\right) \end{aligned} \quad \textbf{(A. 68)}$$

Using the above results we have

$$J\frac{\partial^2\psi}{\partial x^2}+J\frac{\partial^2\psi}{\partial y^2}+J\frac{\partial^2\psi}{\partial z^2}=\frac{\partial}{\partial\xi}\left(J\xi_x\frac{\partial\psi}{\partial x}+J\xi_y\frac{\partial\psi}{\partial y}+J\xi_z\frac{\partial\psi}{\partial z}\right)+$$
$$\frac{\partial}{\partial\eta}\left(J\eta_x\frac{\partial\psi}{\partial x}+J\eta_y\frac{\partial\psi}{\partial y}+J\eta_z\frac{\partial\psi}{\partial z}\right)+ \quad \text{.. (A. 69)}$$
$$\frac{\partial}{\partial\zeta}\left(J\zeta_x\frac{\partial\psi}{\partial x}+J\zeta_y\frac{\partial\psi}{\partial y}+J\zeta_z\frac{\partial\psi}{\partial z}\right)$$

Using the chain rule for the right-hand side of Eq. (A. 69) we have

$$J\xi_x\frac{\partial\psi}{\partial x}+J\xi_y\frac{\partial\psi}{\partial y}+J\xi_z\frac{\partial\psi}{\partial z}=J\xi_x\left(\frac{\partial\psi}{\partial\xi}\xi_x+\frac{\partial\psi}{\partial\eta}\eta_x+\frac{\partial\psi}{\partial\zeta}\zeta_x\right)+$$
$$J\xi_y\left(\frac{\partial\psi}{\partial\xi}\xi_y+\frac{\partial\psi}{\partial\eta}\eta_y+\frac{\partial\psi}{\partial\zeta}\zeta_y\right)+J\xi_z\left(\frac{\partial\phi}{\partial\xi}\xi_z+\frac{\partial\phi}{\partial\eta}\eta_z+\frac{\partial\phi}{\partial\zeta}\zeta_z\right)$$
$$=J\frac{\partial\psi}{\partial\xi}\left[(\xi_x)^2+(\xi_y)^2+(\xi_y)^2\right]+J\frac{\partial\psi}{\partial\eta}\left(\xi_x\eta_x+\xi_y\eta_y+\xi_z\eta_z\right)+ \quad \text{..... (A. 70)}$$
$$J\frac{\partial\psi}{\partial\zeta}\left(\xi_x\zeta_x+\xi_y\zeta_y+\xi_z\zeta_z\right)$$
$$=\alpha J\frac{\partial\psi}{\partial\xi}+\lambda_1 J\frac{\partial\psi}{\partial\eta}+\lambda_2 J\frac{\partial\psi}{\partial\zeta}$$

Similarly we have

$$J\eta_x\frac{\partial\psi}{\partial x}+J\eta_y\frac{\partial\psi}{\partial y}+J\eta_z\frac{\partial\psi}{\partial z}=J\eta_x\left(\frac{\partial\psi}{\partial\xi}\xi_x+\frac{\partial\psi}{\partial\eta}\eta_x+\frac{\partial\psi}{\partial\zeta}\zeta_x\right)+$$
$$J\eta_y\left(\frac{\partial\psi}{\partial\xi}\xi_y+\frac{\partial\psi}{\partial\eta}\eta_y+\frac{\partial\psi}{\partial\zeta}\zeta_y\right)+J\eta_z\left(\frac{\partial\psi}{\partial\xi}\xi_z+\frac{\partial\psi}{\partial\eta}\eta_z+\frac{\partial\psi}{\partial\zeta}\zeta_z\right)$$
$$=J\frac{\partial\psi}{\partial\xi}\left(\xi_x\eta_x+\xi_y\eta_y+\xi_z\eta_z\right)+J\frac{\partial\psi}{\partial\eta}\left[(\eta_x)^2+(\eta_y)^2+(\eta_z)^2\right]+ \quad \text{..... (A. 71)}$$
$$J\frac{\partial\psi}{\partial\zeta}\left(\eta_x\zeta_x+\eta_y\zeta_y+\eta_z\zeta_z\right)$$
$$=\lambda_1 J\frac{\partial\psi}{\partial\xi}+\beta J\frac{\partial\psi}{\partial\eta}+\lambda_3 J\frac{\partial\psi}{\partial\zeta}$$

$$J\zeta_x\frac{\partial\psi}{\partial x}+J\zeta_y\frac{\partial\psi}{\partial y}+J\zeta_z\frac{\partial\psi}{\partial z}=J\zeta_x\left(\frac{\partial\psi}{\partial\xi}\xi_x+\frac{\partial\psi}{\partial\eta}\eta_x+\frac{\partial\psi}{\partial\zeta}\zeta_x\right)+$$

$$J\zeta_y\left(\frac{\partial\psi}{\partial\xi}\xi_y+\frac{\partial\psi}{\partial\eta}\eta_y+\frac{\partial\psi}{\partial\zeta}\zeta_y\right)+J\zeta_z\left(\frac{\partial\psi}{\partial\xi}\xi_z+\frac{\partial\psi}{\partial\eta}\eta_z+\frac{\partial\psi}{\partial\zeta}\zeta_z\right)$$

$$=J\frac{\partial\psi}{\partial\xi}\left(\xi_x\zeta_x+\xi_y\zeta_y+\xi_z\zeta_z\right)+J\frac{\partial\psi}{\partial\eta}\left(\eta_x\zeta_x+\eta_y\zeta_y+\eta_z\zeta_z\right)+ \quad \text{.. (A. 72)}$$

$$J\frac{\partial\psi}{\partial\zeta}\left[(\zeta_x)^2+(\zeta_y)^2+(\zeta_z)^2\right]$$

$$=\lambda_2 J\frac{\partial\psi}{\partial\xi}+\lambda_3 J\frac{\partial\psi}{\partial\eta}+\gamma J\frac{\partial\psi}{\partial\zeta}$$

where

$$\alpha=(\xi_x)^2+(\xi_y)^2+(\xi_z)^2 \quad \text{..... (A. 73)}$$

$$\beta=(\eta_x)^2+(\eta_y)^2+(\eta_z)^2 \quad \text{..... (A. 74)}$$

$$\gamma=(\zeta_x)^2+(\zeta_y)^2+(\zeta_z)^2 \quad \text{..... (A. 75)}$$

$$\lambda_1=\xi_x\eta_x+\xi_y\eta_y+\xi_z\eta_z \quad \text{..... (A. 76)}$$

$$\lambda_2=\xi_x\zeta_x+\xi_y\zeta_y+\xi_z\zeta_z \quad \text{..... (A. 77)}$$

$$\lambda_3=\eta_x\zeta_x+\eta_y\zeta_y+\eta_z\zeta_z \quad \text{..... (A. 78)}$$

The right-hand side of the momentum equations is

$$J\frac{\partial^2\psi}{\partial x^2}+J\frac{\partial^2\psi}{\partial y^2}+J\frac{\partial^2\psi}{\partial z^2}=\frac{\partial}{\partial\xi}\left(\alpha J\frac{\partial\psi}{\partial\xi}+\lambda_1 J\frac{\partial\psi}{\partial\eta}+\lambda_2 J\frac{\partial\psi}{\partial\zeta}\right)+$$

$$\frac{\partial}{\partial\eta}\left(\lambda_1 J\frac{\partial\psi}{\partial\xi}+\beta J\frac{\partial\psi}{\partial\eta}+\lambda_3 J\frac{\partial\psi}{\partial\zeta}\right)+\frac{\partial}{\partial\zeta}\left(\lambda_2 J\frac{\partial\psi}{\partial\xi}+\lambda_3 J\frac{\partial\psi}{\partial\eta}+\gamma J\frac{\partial\psi}{\partial\zeta}\right) \quad \text{... (A. 79)}$$

Substituting Eq. (A. 53) and (A. 79) into momentum equations gives

$$\rho\frac{\partial}{\partial\xi}(U\psi)+\rho\frac{\partial}{\partial\eta}(V\psi)+\rho\frac{\partial}{\partial\zeta}(W\psi)=\mu\frac{\partial}{\partial\xi}\left(\alpha J\frac{\partial\psi}{\partial\xi}+\lambda_1 J\frac{\partial\psi}{\partial\eta}+\lambda_2 J\frac{\partial\psi}{\partial\zeta}\right)+$$
$$\mu\frac{\partial}{\partial\eta}\left(\lambda_1 J\frac{\partial\psi}{\partial\xi}+\beta J\frac{\partial\psi}{\partial\eta}+\lambda_3 J\frac{\partial\psi}{\partial\zeta}\right)+\mu\frac{\partial}{\partial\zeta}\left(\lambda_2 J\frac{\partial\psi}{\partial\xi}+\lambda_3 J\frac{\partial\psi}{\partial\eta}+\gamma J\frac{\partial\psi}{\partial\zeta}\right)+s_i \quad \text{.... (A. 80)}$$

Rearranging Eq. (A. 80) gives

$$\frac{\partial}{\partial\xi}\left[\rho U\psi-\mu J\left(\alpha\frac{\partial\psi}{\partial\xi}+\lambda_1\frac{\partial\psi}{\partial\eta}+\lambda_2\frac{\partial\psi}{\partial\zeta}\right)\right]+\frac{\partial}{\partial\eta}\left[\rho V\psi-\mu J\left(\lambda_1\frac{\partial\psi}{\partial\xi}+\beta\frac{\partial\psi}{\partial\eta}+\lambda_3\frac{\partial\psi}{\partial\zeta}\right)\right]+$$
$$\frac{\partial}{\partial\zeta}\left[\rho U\psi-\mu J\left(\lambda_2\frac{\partial\psi}{\partial\xi}+\lambda_3\frac{\partial\psi}{\partial\eta}+\gamma\frac{\partial\psi}{\partial\zeta}\right)\right]=s_i$$
..... **(A. 81)**

where

$$s_x=-J\left(\frac{\partial\xi}{\partial x}\frac{\partial p}{\partial\xi}+\frac{\partial\eta}{\partial x}\frac{\partial p}{\partial\eta}+\frac{\partial\zeta}{\partial x}\frac{\partial p}{\partial\zeta}\right) \quad \text{..... (A. 82)}$$

$$s_y=-J\left(\frac{\partial\xi}{\partial y}\frac{\partial p}{\partial\xi}+\frac{\partial\eta}{\partial y}\frac{\partial p}{\partial\eta}+\frac{\partial\zeta}{\partial y}\frac{\partial p}{\partial\zeta}\right) \quad \text{..... (A. 83)}$$

$$s_z=-J\left(\frac{\partial\xi}{\partial z}\frac{\partial p}{\partial\xi}+\frac{\partial\eta}{\partial z}\frac{\partial p}{\partial\eta}+\frac{\partial\zeta}{\partial z}\frac{\partial p}{\partial\zeta}\right) \quad \text{..... (A. 84)}$$

## A-2 Acid Balance Equation

The acid balance equations is

$$\frac{\partial C_D}{\partial t}+u\frac{\partial C_D}{\partial x}+v\frac{\partial C_D}{\partial y}+w\frac{\partial C_D}{\partial z}=\frac{\partial}{\partial y}\left(D_{eff}\frac{\partial C_D}{\partial y}\right) \quad \text{..... (A. 85)}$$

In moving coordinate system with the definition as in Eq. (4. 1), (4. 2), and (4. 3) we have

$$\frac{\partial}{\partial t}=\frac{\partial}{\partial t}+\frac{\partial \xi}{\partial t}\frac{\partial}{\partial \xi}+\frac{\partial \eta}{\partial t}\frac{\partial}{\partial \eta}+\frac{\partial \zeta}{\partial t}\frac{\partial}{\partial \zeta}=\frac{\partial}{\partial t}-\left(\frac{1}{b}\frac{\partial y_1}{\partial t}+\frac{\eta}{b}\frac{\partial b}{\partial t}\right)\frac{\partial}{\partial \eta} \quad \text{..... (A. 86)}$$

$$\frac{\partial^2}{\partial y^2}=\frac{1}{b^2}\left(\frac{\partial^2}{\partial \eta^2}\right) \quad \text{..... (A. 87)}$$

Using the chain rule we have

$$\begin{aligned} u\frac{\partial C_D}{\partial x}+v\frac{\partial C_D}{\partial y}+w\frac{\partial C_D}{\partial z} &= u\left(\frac{\partial C_D}{\partial \xi}\frac{\partial \xi}{\partial x}+\frac{\partial C_D}{\partial \eta}\frac{\partial \eta}{\partial x}+\frac{\partial C_D}{\partial \zeta}\frac{\partial \zeta}{\partial x}\right)+ \\ &\quad v\left(\frac{\partial C_D}{\partial \xi}\frac{\partial \xi}{\partial y}+\frac{\partial C_D}{\partial \eta}\frac{\partial \eta}{\partial y}+\frac{\partial C_D}{\partial \zeta}\frac{\partial \zeta}{\partial y}\right)+ \\ &\quad w\left(\frac{\partial C_D}{\partial \xi}\frac{\partial \xi}{\partial z}+\frac{\partial C_D}{\partial \eta}\frac{\partial \eta}{\partial z}+\frac{\partial C_D}{\partial \zeta}\frac{\partial \zeta}{\partial z}\right)+ \\ &= \frac{\partial C_D}{\partial \xi}\left(u\frac{\partial \xi}{\partial x}+v\frac{\partial \xi}{\partial y}+w\frac{\partial \xi}{\partial z}\right)+\frac{\partial C_D}{\partial \eta}\left(u\frac{\partial \eta}{\partial x}+v\frac{\partial \eta}{\partial y}+w\frac{\partial \eta}{\partial z}\right)+ \\ &\quad \frac{\partial C_D}{\partial \zeta}\left(u\frac{\partial \zeta}{\partial x}+v\frac{\partial \zeta}{\partial y}+w\frac{\partial \eta}{\partial z}\right) \\ &= \frac{U}{J}\frac{\partial C_D}{\partial \xi}+\frac{V}{J}\frac{\partial C_D}{\partial \eta}+\frac{W}{J}\frac{\partial C_D}{\partial \zeta} \end{aligned} \quad \text{..... (A. 88)}$$

Substituting Eq. (A. 86) through (A. 88) into Eq. (A. 85) gives

$$\frac{\partial C_D}{\partial t}-\left(\frac{1}{b}\frac{\partial y_1}{\partial t}+\frac{\eta}{b}\frac{\partial b}{\partial t}\right)\frac{\partial C_D}{\partial \eta}+\frac{U}{J}\frac{\partial C_D}{\partial \xi}+\frac{V}{J}\frac{\partial C_D}{\partial \eta}+\frac{W}{J}\frac{\partial C_D}{\partial \zeta}-D_{eff}\frac{1}{b^2}\frac{\partial^2 C_D}{\partial \eta^2}=0 \quad \text{... (A. 89)}$$

# APPENDIX B

## FINITE DIFFERENCE EQUATIONS

Governing equations are discretized using control volume to get finite difference equations. Fig. B.1 shows an example of control volume unit. E, W, F, R, T, B and P indicate grid points, and e, w, f, r, t and b indicate interface points.

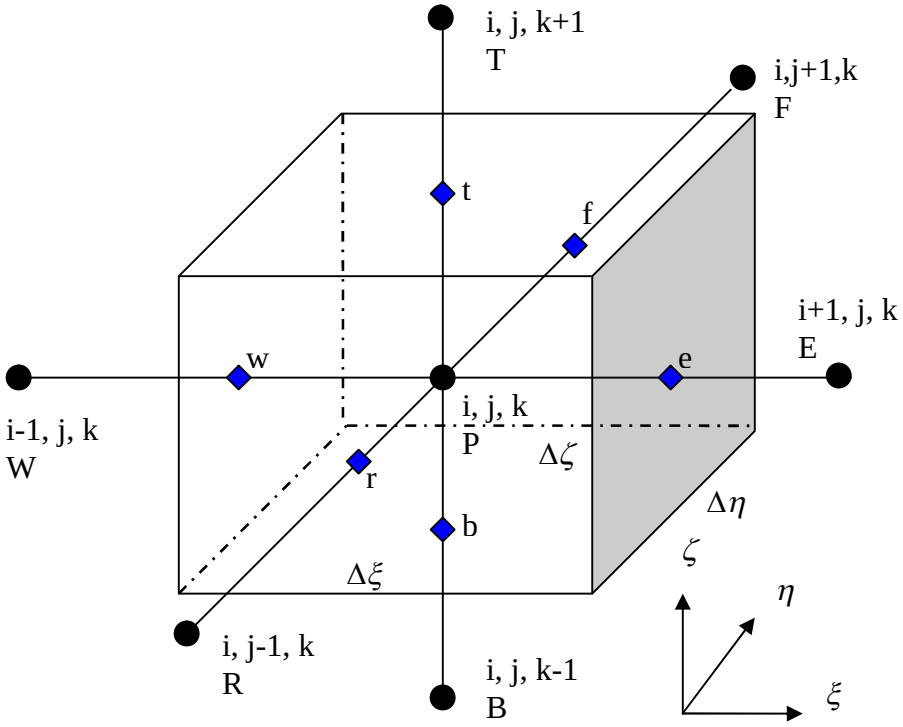


**Fig. B.1 – An example of control volume unit.**

### B-1 Navier-Stokes Equations

In every time step, we solve the Navier-Stokes equations to get velocity fields with known fracture shape and boundary conditions. We use the SIMPLEM (Acharya and Moukalled, 1989) method to solve Navier-Stokes equations. We calculate velocity

fields from momentum equations and calculate pressure field from continuity equation. Iteration is needed to solve for the pressure field and update the velocity fields alternatively. First we estimate velocity fields, then calculate the pressure field based on velocity fields, next update velocity fields based on pressure fields, and iterate to get converged solution.

Momentum equations in three coordinate directions are similar in format, so it can be written in a unified form.

$$\frac{\partial}{\partial\xi}\left[\rho U\psi-\mu J\left(\alpha\frac{\partial\psi}{\partial\xi}+\lambda_1\frac{\partial\psi}{\partial\eta}+\lambda_2\frac{\partial\psi}{\partial\zeta}\right)\right]+\frac{\partial}{\partial\eta}\left[\rho V\psi-\mu J\left(\lambda_1\frac{\partial\psi}{\partial\xi}+\beta\frac{\partial\psi}{\partial\eta}+\lambda_3\frac{\partial\psi}{\partial\zeta}\right)\right]+$$
$$\frac{\partial}{\partial\zeta}\left[\rho W\psi-\mu J\left(\lambda_2\frac{\partial\psi}{\partial\xi}+\lambda_3\frac{\partial\psi}{\partial\eta}+\gamma\frac{\partial\psi}{\partial\zeta}\right)\right]=s_i \quad \text{..... (B. 1)}$$

where

$$i=x,y,z \quad \text{..... (B. 2)}$$

$$s_x=-J\left(\frac{\partial\xi}{\partial x}\frac{\partial p}{\partial\xi}+\frac{\partial\eta}{\partial x}\frac{\partial p}{\partial\eta}+\frac{\partial\zeta}{\partial x}\frac{\partial p}{\partial\zeta}\right) \quad \text{..... (B. 3)}$$

$$s_y=-J\left(\frac{\partial\xi}{\partial y}\frac{\partial p}{\partial\xi}+\frac{\partial\eta}{\partial y}\frac{\partial p}{\partial\eta}+\frac{\partial\zeta}{\partial y}\frac{\partial p}{\partial\zeta}\right) \quad \text{..... (B. 4)}$$

$$s_z=-J\left(\frac{\partial\xi}{\partial z}\frac{\partial p}{\partial\xi}+\frac{\partial\eta}{\partial z}\frac{\partial p}{\partial\eta}+\frac{\partial\zeta}{\partial z}\frac{\partial p}{\partial\zeta}\right) \quad \text{..... (B. 5)}$$

$$\alpha=(\xi_x)^2+(\xi_y)^2+(\xi_z)^2 \quad \text{..... (B. 6)}$$

$$\beta=(\eta_x)^2+(\eta_y)^2+(\eta_z)^2 \quad \text{..... (B. 7)}$$

$$\gamma=(\zeta_x)^2+(\zeta_y)^2+(\zeta_z)^2 \quad \text{..... (B. 8)}$$

$$\lambda_1 = \xi_x \eta_x + \xi_y \eta_y + \xi_z \eta_z \quad \text{..... (B. 9)}$$

$$\lambda_2 = \xi_x \zeta_x + \xi_y \zeta_y + \xi_z \zeta_z \quad \text{..... (B. 10)}$$

$$\lambda_3 = \eta_x \zeta_x + \eta_y \zeta_y + \eta_z \zeta_z \quad \text{..... (B. 11)}$$

Integrating over the control volume depicted in Fig. B.1 gives

$$\begin{aligned} &\rho \Delta\eta\Delta\zeta (U\psi)_w^e - \mu\Delta\eta\Delta\zeta \left[ J\left( \alpha \frac{\partial\psi}{\partial\xi} + \lambda_1 \frac{\partial\psi}{\partial\eta} + \lambda_2 \frac{\partial\psi}{\partial\zeta} \right) \right]_w^e \\ &+ \rho \Delta\xi\Delta\zeta (V\psi)_r^f - \mu\Delta\xi\Delta\zeta \left[ J\left( \lambda_1 \frac{\partial\psi}{\partial\xi} + \beta \frac{\partial\psi}{\partial\eta} + \lambda_3 \frac{\partial\psi}{\partial\zeta} \right) \right]_r^f \\ &+ \rho \Delta\xi\Delta\eta (W\psi)_b^t - \mu\Delta\xi\Delta\eta \left[ J\left( \lambda_2 \frac{\partial\psi}{\partial\xi} + \lambda_3 \frac{\partial\psi}{\partial\eta} + \gamma \frac{\partial\psi}{\partial\zeta} \right) \right]_b^t = s\Delta\xi\Delta\eta\Delta\zeta \end{aligned} \quad \text{..... (B. 12)}$$

Rearranging the above equation gives

$$\begin{aligned} &\rho \Delta\eta\Delta\zeta (U\psi)_w^e - \mu\Delta\eta\Delta\zeta \left[ J\alpha \frac{\partial\psi}{\partial\xi} \right]_w^e + \rho \Delta\xi\Delta\zeta (V\psi)_r^f - \mu\Delta\xi\Delta\zeta \left[ J\beta \frac{\partial\psi}{\partial\eta} \right]_r^f \\ &+ \rho \Delta\xi\Delta\eta (W\psi)_b^t - \mu\Delta\xi\Delta\eta \left[ J\gamma \frac{\partial\psi}{\partial\zeta} \right]_b^t = s_i \Delta\xi\Delta\eta\Delta\zeta + m_i \end{aligned} \quad \text{..... (B. 13)}$$

where

$$\begin{aligned} m_i = &\mu\Delta\eta\Delta\zeta \left[ J\left( \lambda_1 \frac{\partial\psi}{\partial\eta} + \lambda_2 \frac{\partial\psi}{\partial\zeta} \right) \right]_w^e + \mu\Delta\xi\Delta\zeta \left[ J\left( \lambda_1 \frac{\partial\psi}{\partial\xi} + \lambda_3 \frac{\partial\psi}{\partial\zeta} \right) \right]_r^f \\ &+ \mu\Delta\xi\Delta\eta \left[ J\left( \lambda_2 \frac{\partial\psi}{\partial\xi} + \lambda_3 \frac{\partial\psi}{\partial\eta} \right) \right]_b^t \end{aligned} \quad \text{..... (B. 14)}$$

A power law (Patankar, 1980) is used for the first order derivative of velocity. Define

$$a_e = D_e A(|P_e|) + Max(-F_e, 0) \quad \text{..... (B. 15)}$$

$$a_w = D_w A(|P_w|) + Max(F_w, 0) \quad \textbf{(B. 16)}$$

$$a_f = D_f A(|P_f|) + Max(-F_f, 0) \quad \textbf{(B. 17)}$$

$$a_r = D_r A(|P_r|) + Max(F_r, 0) \quad \textbf{(B. 18)}$$

$$a_t = D_t A(|P_t|) + Max(-F_t, 0) \quad \textbf{(B. 19)}$$

$$a_b = D_b A(|P_b|) + Max(F_b, 0) \quad \textbf{(B. 20)}$$

$$A(|P_i|) = Max(0, (1 - 0.1|P_i|)^5) \quad \textbf{(B. 21)}$$

Peclet number $P_i = \frac{F_i}{D_i}$; i denotes the interfaces of w, e, f, r, t, and b between nodes.

$$F_e = (U)_e \rho \Delta\eta\Delta\zeta \quad \textbf{(B. 22)}$$

$$F_w = (U)_w \rho \Delta\eta\Delta\zeta \quad \textbf{(B. 23)}$$

$$F_f = (V)_f \rho \Delta\xi\Delta\zeta \quad \textbf{(B. 24)}$$

$$F_r = (V)_r \rho \Delta\xi\Delta\zeta \quad \textbf{(B. 25)}$$

$$F_t = (W)_t \rho \Delta\xi\Delta\eta \quad \textbf{(B. 26)}$$

$$F_b = (W)_b \rho \Delta\xi\Delta\eta \quad \textbf{(B. 27)}$$

$$D_e = \mu\Delta\eta\Delta\zeta\alpha\left(\frac{J}{\delta\xi}\right)_e \quad \textbf{(B. 28)}$$

$$D_w = \mu\Delta\eta\Delta\zeta\alpha\left(\frac{J}{\delta\xi}\right)_w \quad \textbf{(B. 29)}$$

$$D_f = \mu \Delta\xi \Delta\zeta J \left( \frac{\beta}{\delta\eta} \right)_f \quad \text{..... (B. 30)}$$

$$D_r = \mu \Delta\xi \Delta\zeta J \left( \frac{\beta}{\delta\eta} \right)_r \quad \text{..... (B. 31)}$$

$$D_n = \mu \Delta\xi \Delta\eta \gamma \left( \frac{J}{\delta\zeta} \right)_t \quad \text{..... (B. 32)}$$

$$D_s = \mu \Delta\xi \Delta\eta \gamma \left( \frac{J}{\delta\zeta} \right)_b \quad \text{..... (B. 33)}$$

Finite difference equations of momentum equations are:

$$a_P^1 u_P = \sum_{n=W,E,F,R,T,B} a_n u_n + s_x + m_x \quad \text{..... (B. 34)}$$

$$a_P^1 v_P = \sum_{n=W,E,F,R,T,B} a_n v_n + s_y + m_y \quad \text{..... (B. 35)}$$

$$a_P^1 w_P = \sum_{n=W,E,F,R,T,B} a_n w_n + s_z + m_z \quad \text{..... (B. 36)}$$

where

$$s_x = -\Delta\xi \Delta\eta \Delta\zeta \frac{J}{\rho} \left( \frac{\partial p}{\partial \xi} \xi_x + \frac{\partial p}{\partial \eta} \eta_x + \frac{\partial p}{\partial \zeta} \zeta_x \right) = \left( b_1 \frac{\partial p}{\partial \xi} + c_1 \frac{\partial p}{\partial \eta} + d_1 \frac{\partial p}{\partial \zeta} \right)_P \quad \textbf{(B. 37)}$$

$$s_y = -\Delta\xi \Delta\eta \Delta\zeta \frac{J}{\rho} \left( \frac{\partial p}{\partial \xi} \xi_y + \frac{\partial p}{\partial \eta} \eta_y + \frac{\partial p}{\partial \zeta} \zeta_y \right) = \left( b_2 \frac{\partial p}{\partial \xi} + c_2 \frac{\partial p}{\partial \eta} + d_2 \frac{\partial p}{\partial \zeta} \right)_P \quad \textbf{(B. 38)}$$

$$s_z = -\Delta\xi \Delta\eta \Delta\zeta \frac{J}{\rho} \left( \frac{\partial p}{\partial \xi} \xi_y + \frac{\partial p}{\partial \eta} \eta_y + \frac{\partial p}{\partial \zeta} \zeta_y \right) = \left( b_2 \frac{\partial p}{\partial \xi} + c_2 \frac{\partial p}{\partial \eta} + d_2 \frac{\partial p}{\partial \zeta} \right)_P \quad \textbf{(B. 39)}$$

$$m_x = \mu\Delta\eta\Delta\zeta\left[ J\left( \lambda_1 \frac{\partial u}{\partial \eta} + \lambda_2 \frac{\partial u}{\partial \zeta} \right) \right]_w^e + \mu\Delta\xi\Delta\zeta\left[ J\left( \lambda_1 \frac{\partial u}{\partial \xi} + \lambda_3 \frac{\partial u}{\partial \zeta} \right) \right]_r^f + \mu\Delta\xi\Delta\eta\left[ J\left( \lambda_2 \frac{\partial u}{\partial \xi} + \lambda_3 \frac{\partial u}{\partial \eta} \right) \right]_b^t \quad \text{..... (B. 40)}$$

$$m_y = \mu\Delta\eta\Delta\zeta\left[ J\left( \lambda_1 \frac{\partial v}{\partial \eta} + \lambda_2 \frac{\partial v}{\partial \zeta} \right) \right]_w^e + \mu\Delta\xi\Delta\zeta\left[ J\left( \lambda_1 \frac{\partial v}{\partial \xi} + \lambda_3 \frac{\partial v}{\partial \zeta} \right) \right]_r^f + \mu\Delta\xi\Delta\eta\left[ J\left( \lambda_2 \frac{\partial v}{\partial \xi} + \lambda_3 \frac{\partial v}{\partial \eta} \right) \right]_b^t \quad \text{..... (B. 41)}$$

$$m_z = \mu\Delta\eta\Delta\zeta\left[ J\left( \lambda_1 \frac{\partial w}{\partial \eta} + \lambda_2 \frac{\partial w}{\partial \zeta} \right) \right]_w^e + \mu\Delta\xi\Delta\zeta\left[ J\left( \lambda_1 \frac{\partial w}{\partial \xi} + \lambda_3 \frac{\partial w}{\partial \zeta} \right) \right]_r^f + \mu\Delta\xi\Delta\eta\left[ J\left( \lambda_2 \frac{\partial w}{\partial \xi} + \lambda_3 \frac{\partial w}{\partial \eta} \right) \right]_b^t \quad \text{..... (B. 42)}$$

$$b_1 = -J\xi_x\Delta\xi\Delta\eta\Delta\zeta \quad \text{..... (B. 43)}$$

$$c_1 = -J\eta_x\Delta\xi\Delta\eta\Delta\zeta \quad \text{..... (B. 44)}$$

$$d_1 = -J\zeta_x\Delta\xi\Delta\eta\Delta\zeta \quad \text{..... (B. 45)}$$

$$b_2 = -J\xi_y\Delta\xi\Delta\eta\Delta\zeta \quad \text{..... (B. 46)}$$

$$c_2 = -J\eta_y\Delta\xi\Delta\eta\Delta\zeta \quad \text{..... (B. 47)}$$

$$d_2 = -J\zeta_y\Delta\xi\Delta\eta\Delta\zeta \quad \text{..... (B. 48)}$$

$$b_3 = -J\xi_z\Delta\xi\Delta\eta\Delta\zeta \quad \text{..... (B. 49)}$$

$$c_3 = -J\eta_z\Delta\xi\Delta\eta\Delta\zeta \quad \text{..... (B. 50)}$$

$$d_3 = -J\zeta_z\Delta\xi\Delta\eta\Delta\zeta \quad \text{..... (B. 51)}$$

Next derive pressure finite difference equation from continuity equation.

Rewrite velocity finite difference equations as

$$u_P = \sum_{n=W,E,F,R,T,B} A_n u_n + S_x + M_x \quad \text{..... (B. 52)}$$

$$v_P = \sum_{n=W,E,F,R,T,B} A_n u_n + S_y + M_y \quad \text{..... (B. 53)}$$

$$w_P = \sum_{n=W,E,F,R,T,B} A_n u_n + S_z + M_z \quad \text{..... (B. 54)}$$

where

$$A_n = \frac{a_n}{a_P} \quad \text{..... (B. 55)}$$

$$S_x = \frac{s_x}{a_P} = \left( B_1 \frac{\partial p}{\partial \xi} + C_1 \frac{\partial p}{\partial \eta} + D_1 \frac{\partial p}{\partial \zeta} \right)_p \quad \text{..... (B. 56)}$$

$$S_y = \frac{s_y}{a_P} = \left( B_2 \frac{\partial p}{\partial \xi} + C_2 \frac{\partial p}{\partial \eta} + D_2 \frac{\partial p}{\partial \zeta} \right)_p \quad \text{..... (B. 57)}$$

$$S_\zeta = \frac{s_z}{a_z} = \left( B_3 \frac{\partial p}{\partial \xi} + C_3 \frac{\partial p}{\partial \eta} + D_3 \frac{\partial p}{\partial \zeta} \right)_p \quad \text{..... (B. 58)}$$

$$M_x = \frac{m_x}{a_P} \quad \text{..... (B. 59)}$$

$$M_y = \frac{m_y}{a_P} \quad \text{..... (B. 60)}$$

$$M_z = \frac{m_z}{a_P} \quad \text{..... (B. 61)}$$

$$B_1 = b_1 / a_P \quad \text{..... (B. 62)}$$

$$C_1 = c_1 / a_P \quad \text{..... (B. 63)}$$

$$D_1 = d_1 / a_P \quad \text{..... (B. 64)}$$

$$B_2 = b_2 / a_P \quad \textbf{(B. 65)}$$

$$C_2 = c_2 / a_P \quad \textbf{(B. 66)}$$

$$D_2 = d_2 / a_P \quad \textbf{(B. 67)}$$

$$B_3 = b_3 / a_P \quad \textbf{(B. 68)}$$

$$C_3 = c_3 / a_P \quad \textbf{(B. 69)}$$

$$D_3 = d_3 / a_P \quad \textbf{(B. 70)}$$

$$u_p = u^* + B_1 \frac{\partial p}{\partial \xi} + C_1 \frac{\partial p}{\partial \eta} + D_1 \frac{\partial p}{\partial \zeta} \quad \textbf{(B. 71)}$$

$$v_p = v^* + B_2 \frac{\partial p}{\partial \xi} + C_2 \frac{\partial p}{\partial \eta} + D_2 \frac{\partial p}{\partial \zeta} \quad \textbf{(B. 72)}$$

$$w_p = w^* + B_3 \frac{\partial p}{\partial \xi} + C_3 \frac{\partial p}{\partial \eta} + D_3 \frac{\partial p}{\partial \zeta} \quad \textbf{(B. 73)}$$

where

$$u^* = \sum A_n^1 u_n + M_1 \quad \textbf{(B. 74)}$$

$$v^* = \sum A_n^2 v_n + M_2 \quad \textbf{(B. 75)}$$

$$w^* = \sum A_n^3 w_n + M_2 \quad \textbf{(B. 76)}$$

To get pressure finite difference equation, use momentum interpolation in the continuity equation. It starts with expressing the contravariant velocity components as

$$
\begin{aligned}
U = {} & J\xi_x\left(u^* + B_1\frac{\partial p}{\partial \xi} + C_1\frac{\partial p}{\partial \eta} + D_1\frac{\partial p}{\partial \zeta}\right) + \\
& J\xi_y\left(v^* + B_2\frac{\partial p}{\partial \xi} + C_2\frac{\partial p}{\partial \eta} + D_2\frac{\partial p}{\partial \zeta}\right) + \\
& J\xi_z\left(w^* + B_3\frac{\partial p}{\partial \xi} + C_3\frac{\partial p}{\partial \eta} + D_3\frac{\partial p}{\partial \zeta}\right) \qquad \text{..... (B. 77)} \\
= {} & J\left(u^*\xi_x + v^*\xi_y + w^*\xi_z\right) + \left(J\xi_x B_1 + J\xi_y B_2 + J\xi_z B_3\right)\frac{\partial p}{\partial \xi} \\
& + \left(J\xi_x C_1 + J\xi_y C_2 + J\xi_z C_3\right)\frac{\partial p}{\partial \eta} + \left(J\xi_x D_1 + J\xi_y D_2 + J\xi_z D_3\right)\frac{\partial p}{\partial \zeta} \\
= {} & U^* + \overline{B}_1\frac{\partial p}{\partial \xi} + \overline{C}_1\frac{\partial p}{\partial \eta} + \overline{D}_1\frac{\partial p}{\partial \zeta}
\end{aligned}
$$

where

$$\overline{B}_1 = J\xi_x B_1 + J\xi_y B_2 + J\xi_z B_3 \text{ ..... (B. 78)}$$

$$\overline{C}_1 = J\xi_x C_1 + J\xi_y C_2 + J\xi_z C_3 \text{ ..... (B. 79)}$$

$$\overline{D}_1 = J\xi_x D_1 + J\xi_y D_2 + J\xi_z D_3 \text{ ..... (B. 80)}$$

$$U^* = J\left(u^*\xi_x + v^*\xi_y + w^*\xi_z\right) \text{ ..... (B. 81)}$$

Similarly we have

$$
\begin{aligned}
V = {} & J\eta_x\left(u^* + B_1\frac{\partial p}{\partial \xi} + C_1\frac{\partial p}{\partial \eta} + D_1\frac{\partial p}{\partial \zeta}\right) + \\
& J\eta_y\left(v^* + B_2\frac{\partial p}{\partial \xi} + C_2\frac{\partial p}{\partial \eta} + D_2\frac{\partial p}{\partial \zeta}\right) + \\
& J\eta_z\left(w^* + B_3\frac{\partial p}{\partial \xi} + C_3\frac{\partial p}{\partial \eta} + D_3\frac{\partial p}{\partial \zeta}\right) \\
= {} & J\left(u^*\eta_x + v^*\eta_y + w^*\eta_z\right) + \left(J\eta_x B_1 + J\eta_y B_2 + J\eta_z B_3\right)\frac{\partial p}{\partial \xi} \\
& + \left(J\eta_x C_1 + J\eta_y C_2 + J\eta_z C_3\right)\frac{\partial p}{\partial \eta} + \left(J\eta_x D_1 + J\eta_y D_2 + J\eta_z D_3\right)\frac{\partial p}{\partial \zeta} \\
= {} & V^* + \overline{B}_2\frac{\partial p}{\partial \xi} + \overline{C}_2\frac{\partial p}{\partial \eta} + \overline{D}_2\frac{\partial p}{\partial \zeta}
\end{aligned}
\qquad \text{..... } \textbf{(B. 82)}
$$

$$\overline{B}_2 = J\eta_x B_1 + J\eta_y B_2 + J\eta_z B_3 \text{ ..... } \textbf{(B. 83)}$$

$$\overline{C}_2 = J\eta_x C_1 + J\eta_y C_2 + J\eta_z C_3 \text{ ..... } \textbf{(B. 84)}$$

$$\overline{D}_2 = J\eta_x D_1 + J\eta_y D_2 + J\eta_z D_3 \text{ ..... } \textbf{(B. 85)}$$

$$V^* = J\left(u^*\eta_x + v^*\eta_y + w^*\eta_z\right) \text{..... } \textbf{(B. 86)}$$

$$
\begin{aligned}
W = {} & J\zeta_x\left(u^* + B_1\frac{\partial p}{\partial \xi} + C_1\frac{\partial p}{\partial \eta} + D_1\frac{\partial p}{\partial \zeta}\right) + \\
& J\zeta_y\left(v^* + B_2\frac{\partial p}{\partial \xi} + C_2\frac{\partial p}{\partial \eta} + D_2\frac{\partial p}{\partial \zeta}\right) + \\
& J\zeta_z\left(w^* + B_3\frac{\partial p}{\partial \xi} + C_3\frac{\partial p}{\partial \eta} + D_3\frac{\partial p}{\partial \zeta}\right) \\
= {} & J\left(u^*\zeta_x + v^*\zeta_y + w^*\zeta_z\right) + \left(J\zeta_x B_1 + J\zeta_y B_2 + J\zeta_z B_3\right)\frac{\partial p}{\partial \xi} \\
& + \left(J\zeta_x C_1 + J\zeta_y C_2 + J\zeta_z C_3\right)\frac{\partial p}{\partial \eta} + \left(J\zeta_x D_1 + J\zeta_y D_2 + J\zeta_z D_3\right)\frac{\partial p}{\partial \zeta} \\
= {} & W^* + \overline{B}_3\frac{\partial p}{\partial \xi} + \overline{C}_3\frac{\partial p}{\partial \eta} + \overline{D}_3\frac{\partial p}{\partial \zeta}
\end{aligned}
\qquad \text{..... } \textbf{(B. 87)}
$$

where

$$\overline{B}_3 = J\zeta_x B_1 + J\zeta_y B_2 + J\zeta_z B_3 \quad \textbf{(B. 88)}$$

$$\overline{C}_3 = J\zeta_x C_1 + J\zeta_y C_2 + J\zeta_z C_3 \quad \textbf{(B. 89)}$$

$$\overline{D}_3 = J\zeta_x D_1 + J\zeta_y D_2 + J\zeta_z D_3 \quad \textbf{(B. 90)}$$

$$W^* = J\left(u^*\zeta_x + v^*\zeta_y + w^*\zeta_z\right) \quad \textbf{(B. 91)}$$

Integrating the continuity equation on a control volume gives

$$\left(U\Delta\eta\Delta\zeta\right)_w^e + \left(V\xi\Delta\zeta\right)_r^f + \left(W\xi\Delta\eta\right)_b^t = 0 \quad \textbf{(B. 92)}$$

Substitution of $U$ , $V$ , and $W$ into Eq. (B. 92) leads to

$$\begin{aligned}\eta\Delta\zeta\left(U^* + \overline{B}_1\frac{\partial p}{\partial\xi} + \overline{C}_1\frac{\partial p}{\partial\eta} + \overline{D}_1\frac{\partial p}{\partial\zeta}\right)_w^e + \Delta\xi\Delta\zeta\left(V^* + \overline{B}_2\frac{\partial p}{\partial\xi} + \overline{C}_2\frac{\partial p}{\partial\eta} + \overline{D}_2\frac{\partial p}{\partial\zeta}\right)_r^f \\ + \Delta\xi\Delta\eta\left(W^* + \overline{B}_3\frac{\partial p}{\partial\xi} + \overline{C}_3\frac{\partial p}{\partial\eta} + \overline{D}_3\frac{\partial p}{\partial\zeta}\right)_b^t = 0\end{aligned} \quad \textbf{(B. 93)}$$

Rearranging the above equation gives

$$\begin{aligned}&\left(\overline{B}_1\frac{\partial p}{\partial\xi}\Delta\eta\Delta\zeta\right)_w^e + \left(\overline{C}_2\frac{\partial p}{\partial\eta}\Delta\xi\Delta\zeta\right)_r^f + \left(\overline{D}_3\frac{\partial p}{\partial\zeta}\Delta\xi\Delta\eta\right)_b^t = \\ &-\left(U^*\Delta\eta\Delta\zeta\right)_w^e - \left(V^*\Delta\xi\Delta\zeta\right)_r^f - \left(W^*\Delta\xi\Delta\eta\right)_b^t - \eta\Delta\zeta\left(\overline{C}_1\frac{\partial p}{\partial\eta} + \overline{D}_1\frac{\partial p}{\partial\zeta}\right)_w^e \\ &-\Delta\xi\Delta\zeta\left(\overline{B}_2\frac{\partial p}{\partial\xi} + \overline{D}_2\frac{\partial p}{\partial\zeta}\right)_r^f - \Delta\xi\Delta\eta\left(\overline{B}_3\frac{\partial p}{\partial\xi} + \overline{C}_3\frac{\partial p}{\partial\eta}\right)_b^t\end{aligned} \quad \textbf{(B. 94)}$$

$$\begin{aligned}&(p_P - p_E)\Delta\eta\Delta\zeta\left(\frac{\overline{B}_1}{\delta\xi}\right)_e + (p_P - p_W)\Delta\eta\Delta\zeta\left(\frac{\overline{B}_1}{\delta\xi}\right)_w + (p_P - p_F)\Delta\xi\Delta\zeta\left(\frac{\overline{C}_2}{\delta\eta}\right)_f \\ &+ (p_P - p_R)\Delta\xi\Delta\zeta\left(\frac{\overline{C}_2}{\delta\eta}\right)_r + (p_P - p_T)\Delta\xi\Delta\mu\left(\frac{\overline{D}_3}{\delta\zeta}\right)_t + (p_P - p_B)\Delta\xi\Delta\mu\left(\frac{\overline{D}_3}{\delta\zeta}\right)_b = f\end{aligned} \quad \textbf{(B. 95)}$$

where

$$f = \Delta\eta\Delta\zeta\left(U^*\right)_w^e + \Delta\xi\Delta\zeta\left(V^*\right)_r^f + \Delta\xi\Delta\eta\left(W^*\right)_s^n + f_{no} \quad \textbf{(B. 96)}$$

$$f_{no} = \eta\Delta\zeta\left( C\_1\frac{\partial p}{\partial \eta} + D\_1\frac{\partial p}{\partial \zeta}\right)_w^e + \Delta\xi\Delta\zeta\left( B\_2\frac{\partial p}{\partial \xi} + D\_2\frac{\partial p}{\partial \zeta}\right)_r^f + \Delta\xi\Delta\eta\left( B\_3\frac{\partial p}{\partial \xi} + C + 3\frac{\partial p}{\partial \eta}\right)_b^t \quad \text{..... (B. 97)}$$

Therefore the finite equation for pressure is

$$a_P p_P = \sum_{EWTBFR} a_n p_n + f \quad \text{..... (B. 98)}$$

where

$$a_E = \Delta\eta\Delta\zeta\left(\frac{B}{\delta\xi}\right)_e \quad \text{..... (B. 99)}$$

$$a_W = \Delta\eta\Delta\zeta\left(\frac{B}{\delta\xi}\right)_w \quad \text{..... (B. 100)}$$

$$a_F = \Delta\xi\Delta\zeta\left(\frac{C}{\delta\eta}\right)_f \quad \text{..... (B. 101)}$$

$$a_R = \Delta\xi\Delta\zeta\left(\frac{C}{\delta\eta}\right)_r \quad \text{..... (B. 102)}$$

$$a_T = \Delta\xi\Delta\eta\left(\frac{D}{\delta\zeta}\right)_t \quad \text{..... (B. 103)}$$

$$a_B = \Delta\xi\Delta\eta\left(\frac{D}{\delta\zeta}\right)_b \quad \text{..... (B. 104)}$$

$$a_P = a_E + a_W + a_F + a_R + a_N + a_S \quad \text{..... (B. 105)}$$

## B-2 Acid Balance Equation

Acid balance equations is

$$\frac{\partial C_D}{\partial t}-\left(\frac{1}{b}\frac{\partial y_1}{\partial t}+\frac{\eta}{b}\frac{\partial b}{\partial t}\right)\frac{\partial C_D}{\partial \eta}+\frac{U}{J}\frac{\partial C_D}{\partial \xi}+\frac{V}{J}\frac{\partial C_D}{\partial \eta}+\frac{W}{J}\frac{\partial C_D}{\partial \zeta}-D_{eff}\frac{1}{b^2}\frac{\partial^2 C_D}{\partial \eta^2}=0 \quad \text{.....}$$

..... **(B. 106)**

Using upwind method for first order derivative we have

$$\begin{aligned}
&\frac{\left(C_D^{n+1}\right)_{i,j,k}-\left(C_D^{n}\right)_{i,j,k}}{\Delta t}\\
&\max(-\frac{U}{J},0)\frac{\left(C_D^{n+1}\right)_{i,j,k}-\left(C_D^{n+1}\right)_{i+1,j,k}}{\Delta \xi}+\max(\frac{U}{J},0)\frac{\left(C_D^{n+1}\right)_{i,j,k}-\left(C_D^{n+1}\right)_{i-1,j,k}}{\Delta \xi}\\
&+\max(-\frac{W}{J},0)\frac{\left(C_D^{n+1}\right)_{i,j,k}-\left(C_D^{n+1}\right)_{i,j,k+1}}{\Delta \zeta}+\max(\frac{W}{J},0)\frac{\left(C_D^{n+1}\right)_{i,j,k}-\left(C_D^{n+1}\right)_{i,j,k-1}}{\Delta \zeta}\\
&+\max(-\frac{V}{J},0)\frac{\left(C_D^{n+1}\right)_{i,j,k}-\left(C_D^{n+1}\right)_{i,j+1,k}}{\Delta \eta}+\max(\frac{V}{J},0)\frac{\left(C_D^{n+1}\right)_{i,j,k}-\left(C_D^{n+1}\right)_{i,j-1,k}}{\Delta \eta}\\
&-D_{eff}\frac{1}{b^2}\frac{\left(C_D^{n+1}\right)_{i,j+1,k}-2\left(C_D^{n+1}\right)_{i,j,k}+\left(C_D^{n+1}\right)_{i,j-1,k}}{\Delta \eta^2}=\left(\frac{1}{b}\frac{\partial y_1}{\partial t}+\frac{\eta}{b}\frac{\partial b}{\partial t}\right)\frac{\left(C_D^{n}\right)_{i,j+1,k}-\left(C_D^{n}\right)_{i,j-1,k}}{\Delta \eta}
\end{aligned} \quad \textbf{(B. 107)}$$

Finite difference equation is

$$\begin{aligned}
&A_B\left(C_D^{n+1}\right)_{i,j,k-1}+A_R\left(C_D^{n+1}\right)_{i,j-1,k}+A_W\left(C_D^{n+1}\right)_{i-1,j,k}+A_P\left(C_D^{n+1}\right)_{i,j,k}\\
&+A_E\left(C_D^{n+1}\right)_{i+1,j,k}+A_F\left(C_D^{n+1}\right)_{i,j+1,k}+A_T\left(C_D^{n+1}\right)_{i,j,k+1}=M
\end{aligned} \quad \text{.....} \quad \textbf{(B. 108)}$$

where

$$A_B = D_B + F_B \quad \text{.....} \quad \textbf{(B. 109)}$$

$$A_T = D_T + F_T \quad \text{.....} \quad \textbf{(B. 110)}$$

$$A_E = D_E + F_E \quad \text{.....} \quad \textbf{(B. 111)}$$

$$A_R = D_R + F_R \quad \text{.....} \quad \textbf{(B. 112)}$$

$$A_F = D_F + F_F \quad \text{.....} \quad \textbf{(B. 113)}$$

$$A_P = -A_E - A_W - A_F - A_R - A_T - A_B + \Delta\eta\Delta\xi\Delta\zeta \quad \text{.....} \quad \textbf{(B. 114)}$$

$$M = \Delta\eta\Delta\xi\Delta\zeta\left(C_D^n\right)_{i,j,k} + \Delta t\Delta\xi\Delta\zeta\left(\frac{1}{b}\frac{\partial y_1}{\partial t} + \frac{\eta}{b}\frac{\partial b}{\partial t}\right)\frac{\left(C_D^n\right)_{i,j+1,k} - \left(C_D^n\right)_{i,j-1,k}}{\Delta\eta}. \quad \textbf{(B. 115)}$$

$$F_B = -\max(\frac{W\Delta t\Delta\eta\Delta\xi}{J},0) \quad \textbf{(B. 116)}$$

$$F_R = -\max(\frac{V}{J}\Delta t\Delta\xi\Delta\zeta,0) \quad \textbf{(B. 117)}$$

$$F_W = -\max(\frac{U\Delta t\Delta\eta\Delta\zeta}{J},0) \quad \textbf{(B. 118)}$$

$$F_E = -\max(-\frac{U\Delta t\Delta\eta\Delta\zeta}{J},0) \quad \textbf{(B. 119)}$$

$$F_F = -\max(-\frac{V}{J}\Delta t\Delta\xi\Delta\zeta,0) \quad \textbf{(B. 120)}$$

$$F_T = -\max(-\frac{W\Delta t\Delta\eta\Delta\xi}{J},0) \quad \textbf{(B. 121)}$$

$$D_B = 0 \quad \textbf{(B. 122)}$$

$$D_R = -D_{eff}\frac{1}{b^2}\frac{\Delta t\Delta\xi\Delta\zeta}{\Delta\eta} \quad \textbf{(B. 123)}$$

$$D_W = 0 \quad \textbf{(B. 124)}$$

$$D_E = 0 \quad \textbf{(B. 125)}$$

$$D_F = -D_{eff}\frac{1}{b^2}\frac{\Delta t\Delta\xi\Delta\zeta}{\Delta\eta} \quad \textbf{(B. 126)}$$

$$D_T = 0 \quad \textbf{(B. 127)}$$

For acid balance equation, boundary conditions on fracture walls are specified implicitly, so it should be expressed in discrete form. Grid index in $\eta$ direction is 0, 1, ... NY-1.

On $\eta = 0$

$$\frac{D_{eff} C_i}{b} \frac{\partial C_D}{\partial \eta} = E_f (C_i C_D - C_{eqm})^{n'} (1-\phi)\Big|_{\eta=0} \quad \text{..... (B. 128)}$$

Assume $C_{eqm} = 0$

$$\frac{\partial C_D}{\partial \eta} = \frac{b}{C_i D_{eff}} E_f (C_i C_D)^{n'} (1-\phi)\Big|_{\eta=0} \quad \text{..... (B. 129)}$$

$$\frac{\left(C_D^{n+1}\right)_1 - \left(C_D^{n+1}\right)_0}{\Delta\eta} = \frac{b C_i^{n'} E_f (1-\phi)\left(C_D^n\right)_0^{n'-1}}{C_i D_{eff}} \left(C_D^{n+1}\right)_0 \quad \text{..... (B. 130)}$$

$$\left(C_D^{n+1}\right)_1 = \left[1 + \frac{b C_i^{n'-1} E_f (1-\phi) C_0^{n-1}}{D_{eff}} \Delta\eta\right] \left(C_D^{n+1}\right)_0 \quad \text{..... (B. 131)}$$

$$\left(C_D^{n+1}\right)_0 = \frac{1}{\left[1 + \frac{b C_i^{n'-1} E_f (1-\phi)\left(C_D^n\right)_0^{n'-1}}{D_{eff}} \Delta\eta\right]} \left(C_D^{n+1}\right)_1 \quad \text{..... (B. 132)}$$

On $\eta = 1$

$$\frac{\partial C_D}{\partial \eta} = -\frac{b}{C_i D_{eff}} E_f (C_i C_D)^{n'} (1-\phi)\Big|_{\eta=1} \quad \text{..... (B. 133)}$$

$$\frac{\left(C_D^{n+1}\right)_{NY-1} - \left(C_D^{n+1}\right)_{NY-2}}{\Delta\eta} = -\frac{b C_i^{n'} E_f (1-\phi)\left(C_D^{n+1}\right)_{NY-1}^{n'-1}}{C_i D_{eff}} \left(C_D^{n+1}\right)_{NY-1} \quad \text{..... (B. 134)}$$

$$\left(C_D^{n+1}\right)_{NY-2} = \left[1 + \frac{b C_i^n E_f (1-\phi) C_{NY-1}^{n-1}}{C_i D_{eff}} \Delta\eta\right] \left(C_D^{n+1}\right)_{NY-1} \quad \text{..... (B. 135)}$$

$$\left(C_D^{n+1}\right)_{NY-1} = \frac{1}{\left[1 + \frac{b C_i^n E_f (1-\phi) C_{NY-1}^{n-1}}{C_i D_{eff}} \Delta\eta\right]} \left(C_D^{n+1}\right)_{NY-2} \quad \text{..... (B. 136)}$$

# APPENDIX C

## CONDUCTIVITY CALCULATION

Fracture conductivity at zero closure stress is calculated based on the etching profiles output from the intermediate-scale mode by bringing the two surfaces into contact. Bringing the two surfaces into contact should be done in three-dimension because a few high asperities will support the fracture at zero closure stress. We did in a simpler way. First, we contact the fracture surfaces at every cross section (the vertical direction). At every cross section, we find the minimum etching depth $b_{\min}$. Subtract the minimum etching depth from every point $b(x,z,t)$ gives fracture width distribution at that cross section $b(x,z) = b(x,z,t) - b_{\min}$. Then connecting all cross sections gives the fracture width distribution in the whole domain as shown in Fig. C.1.

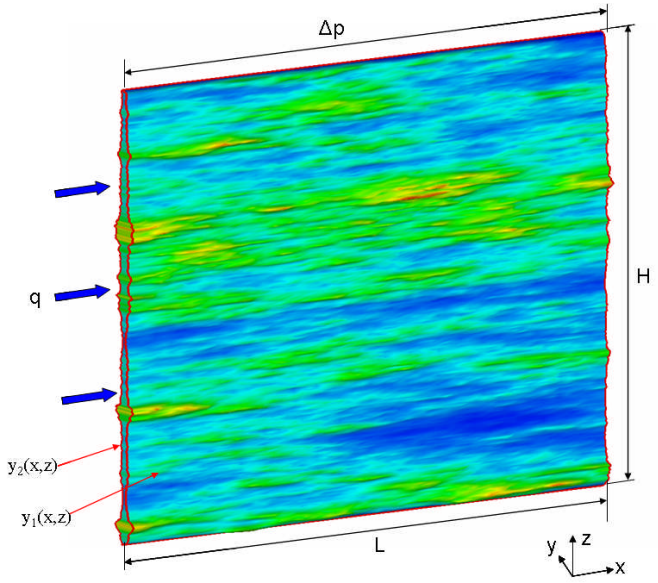


**Fig. C.1 – Fracture width distribution after contacting the two surfaces.**

Rough fracture walls caused by non-uniform etching resulting from heterogeneities prevent convenient conductivity calculation as in proppant fracturing. The common way is to calculate the overall conductivity of the fracture. The overall conductivity can be calculated by using Darcy law with the relationship between overall flow rate and pressure drop along the fracture as

$$\left(k_f w\right)_0 = \frac{q\mu L}{\Delta p H} \quad \text{..... (C. 1)}$$

where

$$\Delta p = p_{in} - p_{out} \quad \text{..... (C. 2)}$$

$$q = \int_0^H \left[ -\frac{b^3(x,z)}{12\mu} \frac{\partial p}{\partial x}\bigg|_{x=0} \right] dz \quad \text{..... (C. 3)}$$

$\left(k_f w\right)_0$ is overall conductivity; $L$ is fracture length; $H$ is fracture height; $\mu$ is fluid viscosity; $q$ is overall flux; $p_{in}$ is the pressure at the inlet; and $p_{outlet}$ is pressure at the outlet. This requires calculating the relationship of $q$ and $\Delta p$ for the fracture.

To get the relationship of $\Delta p$ and $q$, we need to calculate fluid flow in the fracture numerically. Local cubic law equation (Brush 2003) is used to calculate fluid flow in the fracture.

$$\frac{\partial}{\partial x}\left( \frac{b^3(x,z)}{12\mu} \frac{\partial p(x,z)}{\partial x} \right) + \frac{\partial}{\partial z}\left( \frac{b^3(x,z)}{12\mu} \frac{\partial p(x,z)}{\partial z} \right) = 0 \quad \text{..... (C. 4)}$$

with boundary conditions:

$$p(x = 0, z) = p_{in} \quad \text{..... (C. 5)}$$

$$p(x = L, z) = p_{out} \quad \text{..... (C. 6)}$$

$$\left.\frac{\partial p(x,z)}{\partial z}\right|_{z=0,H} = 0 \quad \textbf{(C. 7)}$$

The equation is solved numerically in the domain as depicted in Fig. C.1. Specifying inlet and outlet pressure, we can get pressure distribution in the fracture domain. $q$ is calculated based on pressure distribution. After getting $q$ and $\Delta p$ over the fracture domain, we use Eq. (C. 1) to calculate the fracture conductivity.

# APPENDIX D

## COMPUTATIONAL PROCEDURE OF THE MODEL

An example data in the input file is listed in Table D.1.

**Table D. 1 – An example of input data.**

| | |
|---|---|
| Grid number in x direction | 64 |
| Grid number in y direction | 7 |
| Grid number in z direction | 256 |
| Fracture length (m) | 3.048 |
| Fracture height (m) | 3.048 |
| Fracture width (m) | 0.003 |
| Acid fluid viscosity (Poise) | 0.03 |
| Acid fluid density ( $kg/m^3$ ) | 1000 |
| Acid concentration ( $kg.mole/m^3$ ) | 4.4 |
| Diffusion coefficient ( $m^2/s$ ) | 0.000000006 |
| Filtrate viscosity (Poise) | 0.001 |
| Reservoir fluid viscosity (Poise) | 0.001 |
| Formation porosity | 0.12 |
| Total compressibility ( $psi^{-1}$ ) | 0.000005 |
| Limestone density ( $kg/m^3$ ) | 2600 |
| Dolomite density ( $kg/m^3$ ) | 2850 |
| Limestone breakthrough pore volume in core flooding | 2 |
| Dolomite breakthrough pore volume in core flooding | 20 |
| Injection rate (ml/min) | 160 |
| Injection time (min) | 30 |
| Inlet pressure (Pascal) | 600000 |
| Temperature (K) | 373 |
| Pressure difference between the fracture and formation (psi) | 1000 |
| Fraction of acid leakoff to react with the fracture surfaces | 0.3 |
| Mineralogy distribution file (1 for limestone, 0 for dolomite) | Mineralogy.dat |
| Permeability distribution file (md) | Permeability.dat |

The flow chart of the computational program is in Fig. 4.2.

The program modules consist of

1. Preprocessing parts: generating initial fracture shape, permeability distribution, and mineralogy distribution on the fracture surfaces.

- Use GSLIB to generate spatially correlated random number by specifying correlation length in the x and z directions.
- Generate initial fracture shape. It could be regular shape, which just need fracture width, or irregular shape, which can be generated by using the spatially correlated number output from GSLIB.
- Use spatially correlated random number to generate permeability distribution in the module of permeability.sln by specifying average permeability and normalized standard deviation ($\sigma_D = \frac{Stdev \ln(k)}{\ln(avg\_k)}$). If average permeability is 1 md, substitute 10 md for the average permeability. $k(I,K) = \exp[\ln(avg\_k) + \sigma_D \ln(avg\_k) * R(I,K)]$ is for permeability. $R(I,K)]$is random number output from GSLIB. The permeability file output from the module, which is used as input file in main module, include three columns: x coordinate, z coordinate, and permeability
- Use spatially correlated random number to generate mineralogy distribution in the module of mineralogy.sln by specifying percentage of limestone and dolomite. In the mineralogy file output form the module, 1 indicates limestone, and 0 indicates dolomite. The output file, which is used as input

file in main module, include three columns: x coordinate, z coordinate, and mineralogy.

2. The main module (Acid_Fracturing.sln): simulating acid flow in the fracture, acid/rock reaction on the surfaces, and updating fracture surface etching profiles. Acid_Fracturing.cpp is the entrance of the project. Acid_Fracturing.cpp mainly realizes the following functions: read permeability and mineralogy distributions from the data files, call NS function to calculate velocity fields, call Acid_Bal function to calculate acid concentration distribution, call Width_Update function to update fracture width profiles based on acid/rock reaction, and output every minute velocity fields, pressure fields, acid concentration distribution, and fracture width profiles. During solving Navier-Stokes equations, velocity fields are solved in NS function, which call Pressure_Solver to solve pressure equation. An example of input file is listed in Table D.1. The main module output the fracture surface etching profiles.

3 Post processing module (Conductivlty.sln): calculating conductivity based on etching profiles. Given fracture surface profiles, we bring the two fracture surfaces into contact at zero closure stress to get new fracture width distribution. Solving fluid flow in the fracture let us calculate overall conductivity of the fracture. This module output fracture width distribution after contact, average fracture width, standard deviation of fracture width distribution, and conductivity.

# APPENDIX E

## PARAMETER DETERMINATION IN THE CORRELATIONS

When using the correlations, we need to estimate parameters: percentage of limestone and dolomite, the horizontal and vertical correlation lengths of permeability distribution, and standard deviation of natural log of permeability distribution for intermediate-scale. The percentage of limestone and dolomite can be obtained by logging. The hard thing is to get the parameters of permeability distribution. Unlike fine scale or field scale, which can be estimated from geology model or core measurement, intermediate-scale parameters are hard to obtained because no data in intermediate-scale is available. Goggin *et al*. (1992) did a study showing that statistical measures of variability and spatial correlation (but not mean permeability) are portable between the outcrops and subsurface. According to their method, we can use mechanical field permeameter to measure permeability at very small spacing in the horizontal and vertical directions within a dimension of 10 by 10 ft. With the measure data, we can do variogram analysis to get the horizontal and vertical correlation lengths. Calculating standard deviation of natural log of permeability distribution is straight forward.

# APPENDIX F

# ACID/ROCK REACTION RATE AND ACID DIFFUSION COEFFICIENT DETERMINATION

Acid/rock reaction rate is calculated based on the kinetics measured by Lund et al. (1973, 1975) as follows:

$$-r_{HCl} = E_f C_{HCl}^{\alpha} \quad \text{..... (F. 1)}$$

$$E_f = E_f^0 \exp\left(\frac{-\Delta E}{RT}\right) \quad \text{..... (F. 2)}$$

The constants $\alpha$, $E_f^0$, and $\Delta E / R$ are given in Table F.1. SI unit are used in these expressions, so $C_{HCl}^{\alpha}$ is in $kg-mole/m^3$ and T is in $K$.

**Table F. 1 – Constants in acid/rock reaction kinetics.**

| Mineral | $\alpha$ | $E_f^0$ $\frac{\text{kg mole HCl}}{\text{m}^2\text{ - s - (kg - mole HCl/m}^3)^{\alpha}}$ | $\frac{\Delta E}{R}(K)$ |
|---|---|---|---|
| Limestone | 0.63 | $7.314\times10^{7}$ | $7.55\times10^{3}$ |
| Dolomite | $\frac{6.32\times10^{-4}T}{1-1.92\times10^{-3}T}$ | $4.48\times10^{5}$ | $7.9\times10^{3}$ |

Acid diffusion coefficient is calculated by using the correlation developed by Conway et al. (1999). According to their study, acid diffusion coefficient is affected by

temperature, acid concentration, and rock type, but temperature dominates the effect. The rock type effect is neglected in our simulations.

$$D = \exp\left( -\frac{A}{T} + B\sqrt{\frac{[Ca^{2+}]}{H^{+}]}} + C\sqrt{\frac{[Mg^{2+}]}{[H^{+}]}} + D[H^{+}] + E \right) \text{.....(F. 3)}$$

where

$A = -2918.54$

$B = -0.589$

$C = -0.789$

$D = 0.0452$

$E = -4.995, -5.47, -7.99$ for straight, gelled, and emulsified acid respectively.

# VITA

Name: Jianye Mou

Address: Petroleum Engineering Dept., China University of Petroleum-Beijing
18 Fuxue Road, Changping, Beijing, China, 102249

Email Address: moujianye2002@yahoo.com

Education: B.S., Petroleum Engineering, Daqing Petroleum Institute, China, 1998

M.S., Petroleum Engineering, China University of Petroleum-Beijing, China, 2001

Ph.D., Petroleum Engineering, Texas A&M University, USA, 2009

This dissertation was typed by the author.